IKE Institut für Kernenergetik
und Energiesysteme

Numerical Investigation of the Flow and Heat Transfer within the Core Cooling Channel of a Supercritical Water Reactor

Yu Zhu

November 2010 IKE 8 - 122

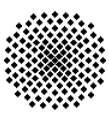

Universität Stuttgart

I K E Institut für Kernenergetik
und Energiesysteme

Numerical Investigation of the Flow and Heat Transfer within the Core Cooling Channel of a Supercritical Water Reactor

von der Fakultät Energie-, Verfahrens- und Biotechnik der Universität Stuttgart zur Erlangung der Würde eines Doktor-Ingenieurs (Dr.-Ing.) genehmigte Abhandlung

vorgelegt von

M.Eng. Yu Zhu
aus Xi'an (China).

Hauptberichter: Prof. Dr.-Ing. habil. E. Laurien

Mitberichter: Prof. Dr.-Ing. T. Schulenberg

Tag der Einreichung: 03.06.2010

Tag der mündlichen Prüfung: 20.09.2010

ISSN – 0173 – 6892

November 2010 IKE 8 - 122

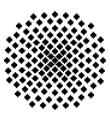

Universität Stuttgart

Institut für Kernenergetik und
Energiesysteme

Universität Stuttgart

Pfaffenwaldring 31

D-70550 Stuttgart

Acknowledgements

It is a true pleasure to thank those who made this thesis possible. First, I want to greatly thank Prof. Eckart Laurien for his guidance and patience. His encouragement and his support helped me to accomplish the objective of this study. His enormous expertise and rigorous attitude to the work are strongly impacting me during my study. I am very grateful to all his help and especially all the encouragements he ever gave me. I wish him all the best with my greatest sincerity.

I would also like to give a special thanks to Prof. Thomas Schulenberg. It was him who introduces me into HPLWR project. His help, not only with the development of this thesis but also through the whole project work, is greatly appreciated.

Next, my thanks go to my office mate Mr. Armin Zirkel (soon to be Dr.) for all his comment and help during my study. I would like also to thank Dr. Thomas Wintteler, Dr. Dominik von Lavante, Dr. Marc Linder, Mr. Muhammad Rashid and other colleagues for all their help and the great atmosphere we shared in IKE.

I sincerely want to give my regards to Prof. Tingkuan Chen, Prof. Yushan Luo and Prof. Haijun Wan in Xi'an Jiaotong University. Thanks for their supports and encouragement in so many years. I also want to send my greeting to Prof. Günter Lohnert. This gentlemen greatly broads my horizons and shows me how wide the world is. Thanks for all his time talking with me.

Last, but not least, I wants to thank my wife Jing and all members of my family for their love and support during my study. I wish all of you good health and happiness forever!

In November 2010

Yu Zhu

Abstract

The High Performance Light Water Reactor (HPLWR) has been investigated currently as one of the Generation IV nuclear reactor concepts. It has potential advantages of 44% thermal efficiency and a compact structure of the plant system. Due to supercritical conditions, a phase change does not occur during the heat-up process in the HPLWR core. Some components in current light water reactors are therefore not necessary. For instance, steam separators and dryers in boiling water reactor, steam generators, pressurizers and primary loop pumps in pressurized water reactor. For HPLWR, a special core layout has been designed in which water as the working fluid is guided three times upward and downward through the core and finally heats up to 500°C. Based on previous calculations, the fluid temperature at the outlet of the first upwards flow, the so-called 'evaporator', will be 390°C, i.e. 5°C higher above the pseudocritical temperature (T_{pc}) of 384.7°C at pressure of 25MPa. In the vicinity of this critical point, strong variations of water properties combined with a high heat flux can lead to a deteriorated heat transfer (DHT), which consequently causes a severe increase of the wall temperature. In general, the empirical heat transfer correlations are not capable of predicting the heat transfer which has strong property variations, especially in cases of deterioration. Hence, the primary aim of this study is to understand the heat transfer behaviour of the supercritical water and the mechanism of the deterioration by means of Computational Fluid Dynamics (CFD). In order to validate the numerical model, several experimental datasets have been chosen for comparison. The results indicated that the current numerical model is capable of not only predicting the normal and enhanced heat transfer, but also capturing the onset of heat transfer deterioration (HTD).

Based on the validated model, a set of thermal hydraulic studies of a single Wire-Wrapped Rod (WWR) in a square channel have been performed on the geometries and working conditions relevant to the HPLWR design. The work aims at further understanding of the flow and heat transfer characteristics in the reactor core, which is strongly influenced by the wire spacer. The presence of the wire inside the fuel assembly results in a strong flow mixing and sweeping effects among sub-channels. Therefore it is difficult to accurately predict the complicated thermal hydraulic behaviour by any correlations. The results of the simulation indicated that the improved heat transfer affected by wire only occurs at a relative high heat flux ($q/G > 1$), which is consistent with the conclusion made by the experimentalist. In the end of this thesis, two form-factors are introduced into a basic heat transfer correlation. These two correction factors aim at taking the "geometry effect" and the "wire effect" into account and can be later used for safety analyses.

Kurzfassung

Der High Performance Light Water Reactor (HPLWR) wird derzeit als ein Konzept der Kernreaktoren der 4. Generation untersucht. Seine möglichen Vorteile liegen in einem hohen thermischen Wirkungsgrad von 44 % und einem kompakten Aufbau. Durch die überkritischen Bedingungen tritt während des Aufheizens im Reaktorkern kein Phasenwechsel auf. Damit sind einige Komponenten der aktuellen Leichtwasserreaktoren nicht notwendig. Diese sind z.B. der Dampfabscheider und die Dampftrocknung beim Siedewasserreaktor bzw. der Dampferzeuger, der Druckhalter sowie die Primärkreislaufpumpen beim Druckwasserreaktor. Für den HPLWR wurde ein spezielles Design des Reaktorkerns entwickelt, welches das Arbeitsmittel Wasser dreifach durch den Kern leitet um es bis zum Austritt auf 500 °C aufzuheizen. Auf Grundlage von vorherigen Berechnungen liegt die Austrittstemperatur nach dem ersten Aufwärtsstrom, dem so genannten „Verdampfer“, mit 390 °C ca. 5 K über der pseudokritischen Temperatur (T_{pc}) von 384.7 °C bei einem Druck von 25 MPa. In der Nähe des kritischen Punkts können jedoch starke Veränderungen der Stoffeigenschaft des Wassers zusammen mit einer hohen Wärmestromdichte zu einem deutlich schlechteren Wärmeübergang (Deteriorated Heat Transfer, DHT) führen. Dies hat einen starken Anstieg der Wandtemperatur zur Folge. Im Allgemeinen sind die empirischen Wärmeübergangskorrelationen nicht geeignet Wärmeübergänge mit solch starken Veränderungen der Stoffeigenschaften vorauszuberechnen. Daher ist das grundsächliche Ziel dieser Arbeit sowohl das Wärmeübergangsverhalten von überkritischem Wasser als auch die Ursachen dessen Verschlechterung mit Hilfe der numerischen Strömungssimulation zu verstehen. Um das numerische Modell zu validieren wurden mehrere experimentelle Datensätze für einen Vergleich ausgewählt. Die Ergebnisse zeigen, dass das numerische Model nicht nur in der Lage ist den normalen und verbesserten Wärmeübergang zu berechnen sondern auch den Beginn der Verschlechterung des Wärmeübergangs erfassen kann.

Mit Hilfe dieses validierten Modells wurden zahlreiche thermo-hydraulischen Studien eines drahtumwickelten Brennstabs innerhalb eines rechtwinkligen Kanals durchgeführt. Hierbei entsprachen sowohl die Geometrie als auch die Betriebsbedingungen den Auslegungsdaten des HPLWR. Ein besseres Verständnis der Strömung und des Wärmeübergangs innerhalb des Reaktorkerns, der maßgeblich vom Abstandshalter (Drahthelix) beeinflusst wird, ist dabei das Ziel dieser Arbeit. Die Anwesenheit des Drahtes führt zu einer starken Vermischung der Strömung und zu Dralleffekten zwischen einzelnen Unterkanälen. Daher ist es schwierig, das komplizierte thermo-hydraulische Verhalten mit Korrelationen zu berechnen. Das Ergebnis der Simulation zeigte jedoch, dass eine Verbesserung des Wärmeübergangs durch die Drahthelix nur bei relativ hohen Wärmestromdichten auftritt, was sich mit den Schlussfolgerungen der Experimentatoren deckt. Daher wird am Ende der Arbeit eine Wärmeübergangskorrelation durch zwei Formfaktoren ergänzt um sowohl den

„Geometrie-“ als auch den „Drahthelixeffekt“ mit einzubeziehen. Diese Korrelation kann damit für zukünftige Sicherheitsanalysen genutzt werden.

Im folgenden ist eine Übersicht der Arbeit zu sehen. (I), Drei grundlegende Geometrien wurden ausgewählt, um den Wärmeübergang Verhalten in überkritischen Fluiden und die Auswirkungen der Geometrie untersuchen. (II) Model Verifizierung und Validierung entsprechend den Geometrien und den Arbeitsbedingungen in den experimentellen Untersuchungen wurden durchgeführt, um das Modell Konfiguration und das Mesh-Setup zu testen. (III) Basierend auf dem validierten Modell, zwei Form-Faktoren können auf der Geometrien und die Arbeitsbedingungen entsprechend dem HPLWR abgeleitet werden.

I. Vereinfachte Geometrien

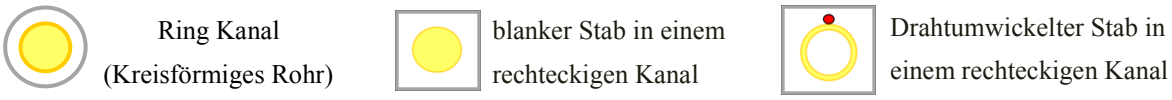

II. Modell Verifizierung und Validierung

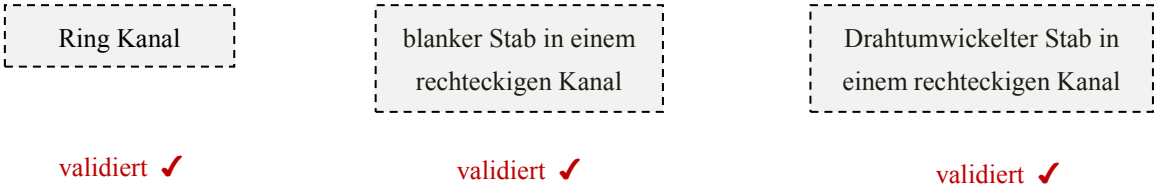

III. Form-Faktor Derivation

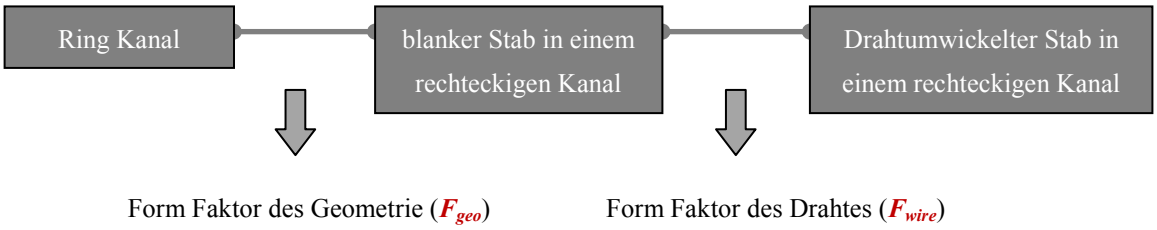

Figure I: Flussdiagramm für die Modellierung des Strömungsverhaltens für überkritischem Wasser mittels numerische Strömungssimulation.

Table of Contents

Notations and Symbols

Letters

A	Flow Area	m^2
Bu	Buoyancy Number, $Bu = \frac{\overline{Gr}_b}{Re_b^{2.7}\overline{Pr}_b^{0.5}}$	Dimensionless
c_p	Specific Heat Capacity	J/kg·K
D	Diameter	m
g	Gravity Acceleration	m/s^2
G	Mass Flux Density	$kg/m^2 \cdot s$
Gr	Grashof Number, $Gr = \frac{(\rho_b - \rho)d^3 g}{\rho \nu^2}$	Dimensionless
$\overline{Gr}$	Grashof Number, $\overline{Gr} = \frac{(\rho_b - \bar{\rho})d^3 g}{\rho \nu^2}$	Dimensionless
h	Heat Transfer Coefficient	$W/m^2 \cdot K$
i	Specific Enthalpy	kJ/kg
k	Turbulence Kinetic Energy	m^2/s^2
Nu	Nusselt Number	Dimensionless
P	Pressure	MPa
Pr	Prandtl Number	Dimensionless
$\overline{Pr}$	Prandtl Number, $\overline{Pr} = \frac{i_w - i_b}{T_w - T_b}\frac{\mu_b}{k_b}$	Dimensionless
q	Heat Flux	kW/m^2
r	Radius	m
Re	Reynolds Number	Dimensionless
T	Temperature	K
u,v,w	Velocity Components in coordinates (x, y, z)	m/s
u′,v′,w′	Fluctuating Velocities in coordinates (x, y, z)	m/s
$\rho\overline{u_i' u_j'}$	Turbulent Stress tensor	m^2/s^2

$\rho c_p \overline{u_j' T'}$	Turbulence Heat Flux	J/ m^2·s
y	Distance from Wall	m
y^+	Non Dimensional Distance	Dimensionless

Greek

ε	Dissipation per unit mass	m^2/s^3
λ	Thermal Conductivity	W/m·K
ν	Kinematic Viscosity	m^2/s
μ	Dynamic Viscosity	kg/m·s
μ_t	Eddy Viscosity	kg/m·s
ρ	Density	kg/m^3
$\bar{\rho}$	Integrated Density, $\bar{\rho} = \frac{1}{T_w - T_b} \int_{T_b}^{T_w} \rho \, \partial T$	kg/m^3
τ	Shear Stress	kg/m^2·s
ω	Specific dissipation rate	1/s

Subscripts

b	Bulk
in	Inlet
max	Maximum Value
min	Minimum Value
out	Outlet
pc	Pseudocritical
rod	Heated Rod
rms	Root Mean Square
t	Turbulent
tube	Tube

w	Wall
wire	Wrapped Wire

Abbreviations

1D	One Dimensional
2D	Two Dimensional
3D	Three Dimensional
BWR	Boiling Water Reactor
CEL	CFX Expression Language
CFD	Computational Fluid Dynamics
DHT	Deteriorated Heat Transfer
DNS	Direct Numerical Simulation
HPLWR	High Performance Light Water Reactor
HTC	Heat Transfer Correlation
HTD	Heat Transfer Deterioration
LES	Large Eddy Simulation
LHTD	Local Heat Transfer Deterioration
PWR	Pressurized Water Reactor
RANS	Reynolds-Averaged Navier-Stokes Equations
RNG	Re-Normalisation Group
RSM	Reynolds Stress Model
SCWR	Supercritical Water Reactor
SSG	Speziale, Sarkar and Gatski RSM
SST	Shear Stress Transport
WWR	Wire-Wrapped Rod

1 Introduction

Nuclear generation began about 60 years ago and today generates 16% global electricity [1]. This percentage is still growing rapidly. About two-thirds of world population lives in nations where nuclear power plants are an integral part of electricity production and industrial infrastructures. Half the people in the world live in countries where new nuclear power plants are in planning or under construction. In 2007, the International Atomic Energy Agency (IAEA) reported that there were over 400 nuclear power reactors in operation in the world, operating in 31 countries, and 29 more are under construction [2]. After the a long depression period due to the TMI and the Chernobyl accidents, the nuclear industry right now is undergoing a revival.

Recent concerns over the emission of nitrous oxides and carbon dioxide is increasingly getting people's attention on the continued use of fossil fuels as a source of energy. The Kyoto Protocol, developed in 1997 and signed by 187 states, requires a reduction in emissions below current values. The Copenhagen Summit, held in 2009 and with 192 countries in attendance, also aims at reducing the carbon dioxide emissions. These targets can be reached very likely by continuing use of nuclear power for the generation of electricity. A typical 1,000-megawatt fossil fired power plant may emit yearly as much as 100,000 tons of sulfur dioxide, 75,000 tons of nitrogen oxides, and 5,000 tons of fly ash [2]. Nuclear power plants produce none of these air pollutants and emit only little amounts of radioactive gases. Compromising between the rapidly increasing energy demand and the target of a reduction in emissions, nuclear power plant has been naturally highlighted in the energy market.

Nuclear reactor generations have been differentiated from each other in the nuclear energy market. Generation I reactors were developed in 1950-60s, which was the early prototype of the power plant. Generation II reactors typified by the commercial reactors were built up to the end of the 1990's and are the most in operation worldwide. It is currently producing 31% electricity in Europe [2]. Generation III and III+ are the development of the generation II reactors, which include some improved technologies. The first reactor of Generation III is in operation in Japan and others are under construction in Finland and France or ready to be built up elsewhere. Generation IV reactors are a set of theoretical nuclear reactor designs being researched currently. The primary goals are to improve nuclear safety and proliferation resistance, minimize waste and natural resource utilization, and reduce the cost of construction and operation.

1.1 Motivation

High Performance Light Water Reactor (HPLWR) has been selected as one of the Generation IV nuclear systems. It is a high-pressure water-cooled reactor which operates above the thermodynamic critical point of water (374 ºC, 22 MPa). The supercritical water (500 ºC at outlet of the core, 25 MPa) directly drives the turbine, without any secondary steam system. Supercritical water has been used in coal fired plants for quite a long time. By increasing the system pressure from subcritical to supercritical pressure, sizes of components can be reduced and higher plant efficiencies can be obtained. The design of HPLWR aims to utilize these advantages of supercritical water technologies into the Light Water Reactors (LWR). By operating its coolant at higher temperature and pressure, it has the potential advantage of a higher thermal efficiency of 44% and a compact structure of the plant system compared with current LWR, see Figure 1–1 and Table 1–1. For instance, steam separators and dryers in Boiling Water Reactor (BWR), steam generators, pressurizers and primary loop pumps in Pressurized Water Reactor (PWR) are not required anymore. Additionally, because the supercritical water could be treated as a single phase fluid as the coolant, the risk of a boiling crisis like burn-out is also physically excluded. Besides these features distinguished with conventional pressurized water reactor and boiling water reactor, HPLWR inherits some in-hand and well-developed technologies from the current power plant, such as the layout design in reactor building, the reactor pressure vessel (RPV) and the already available turbine technologies for such steam pressures and temperatures (see Bittermann et al., [3]), leading to an decrease in the current R&D cost of HPLWR.

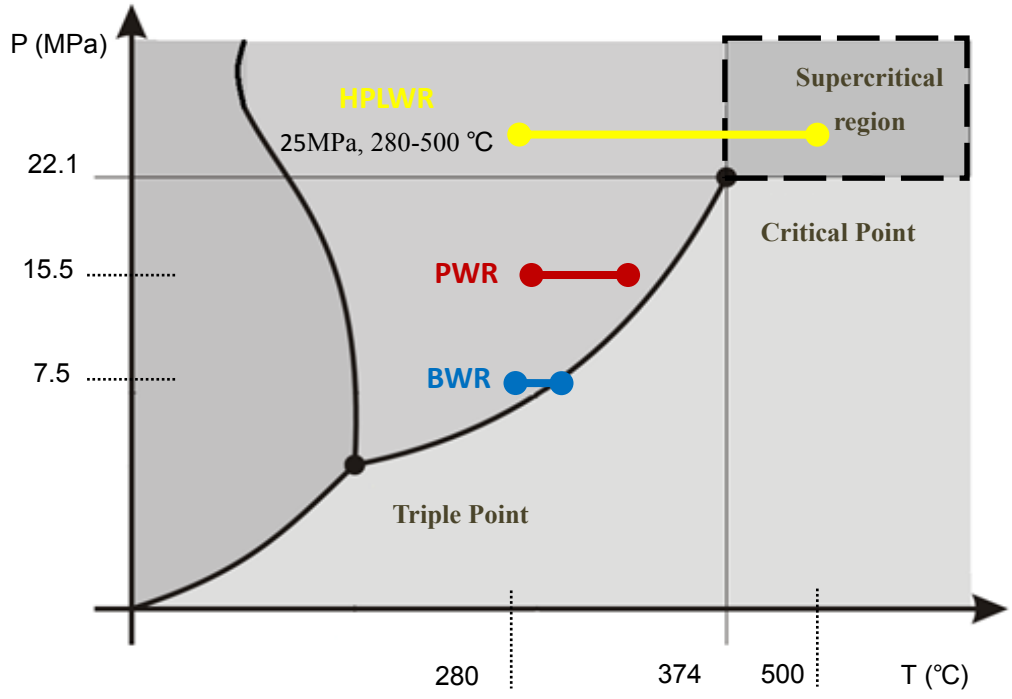

Figure 1–1: Operating Conditions of HPLWR compared with BWR's and PWR's.

	BWR	PWR	HPLWR
Thermal efficiency (%)	34	33	44
Pressure (MPa)	7.5	15.5	25
Outlet Temperature (ºC)	286	330	500
Containment diameter and height (m, m) [4]	~30, 30	~50, 50	~ 20, 20

Table 1–1: Parameters of BWR, PWR and HPLWR

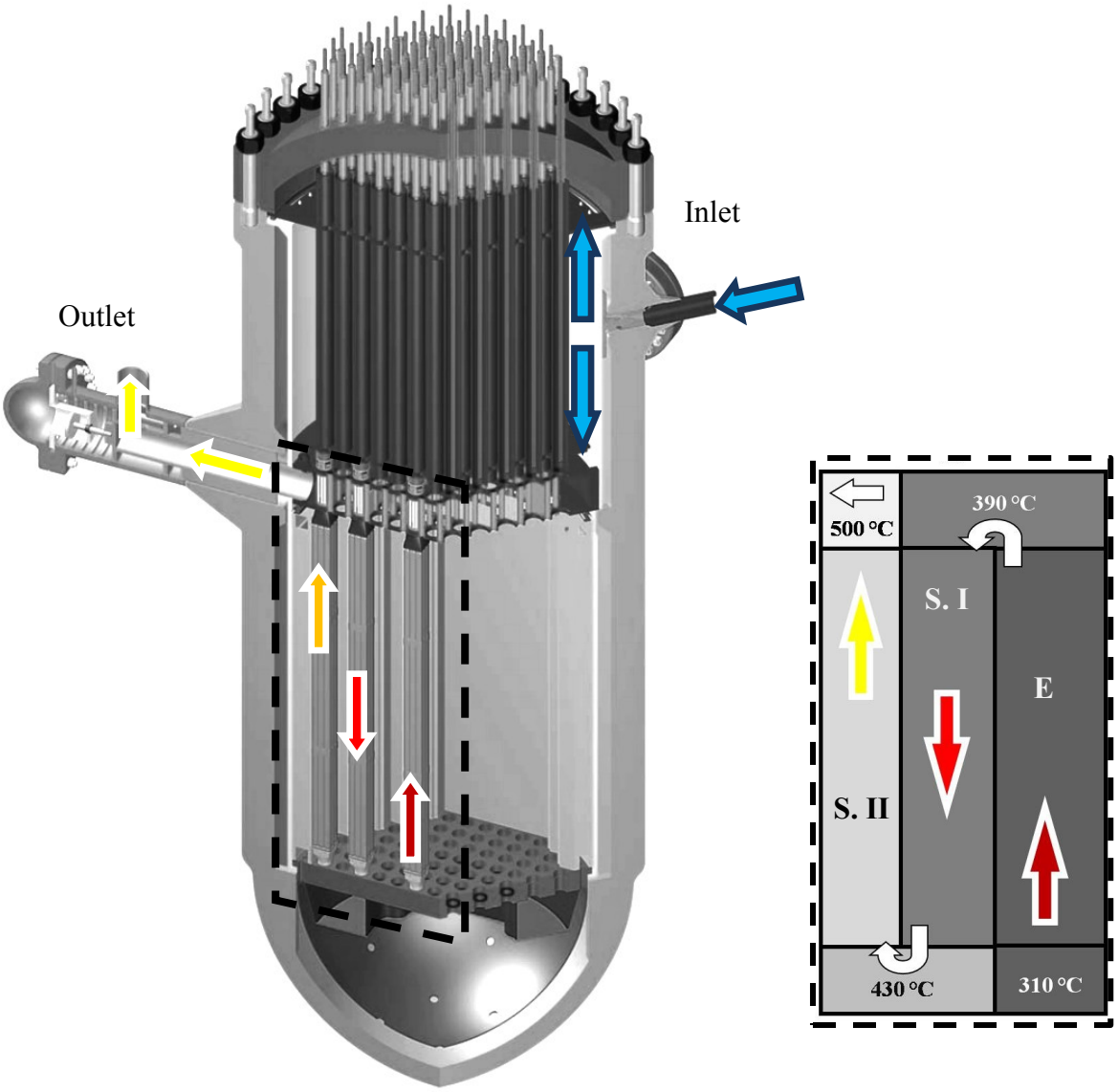

Figure 1–2: Flow directions (by Schulenberg et al. [5]) in the HPLWR core by Fischer et al.[6]. *E.* (Evaporator), *S.I* (Superheater I), *S.II* (Superheater II)

The project “High Performance Light Water Reactor Phase 2” started in September 2006. Up to now, preliminary designs are available for reactor pressure vessel and its internals, such as the reflector, the control rod drives, the core with its assemblies and the mixing plenums. The reactor core with a thermal neutron spectrum has been designed based on the proposal by Schulenberg et al. [5]. As shown in Figure 1–2, the feed water flows in the RPV at a mass flux density of 1179 kg/s, which is roughly one tenth of that in the current PWRs. Then it is divided into an upward flow, which goes into the moderator boxes and gaps with 75% of the total mass flow, and a downward flow with the rest of the mass flow of 294.75 kg/s. The flow path of coolant through the core is designed with three heat-up steps with the intermediate mixing. The first heat-up path is the so-called “*Evaporator*”, which is composed of 52 assembly clusters with upward flow in the nuclear core centre. Supercritical water enters into evaporator at 310 ºC and then leaves it at 390 ºC. After a first mixing in a plenum above the core, water enters into the “*Superheater I*” and flows downward through another 52 assembly clusters which are surrounding the evaporator. The second heat-up path after a lower mixing plenum, “*Superheater II*”, keeps heating the water up and finally provides a temperature of 500 ºC at the core outlet. It can be found that the pseudocritical temperature of the coolant will be exceeded when the coolant flows vertically in the evaporator. Under such conditions the heat transfer coefficient might decrease in some regions when the mass flux is relative low and the heat flux is relative high, which consequently results in a high cladding temperature, or even a severe deterioration.

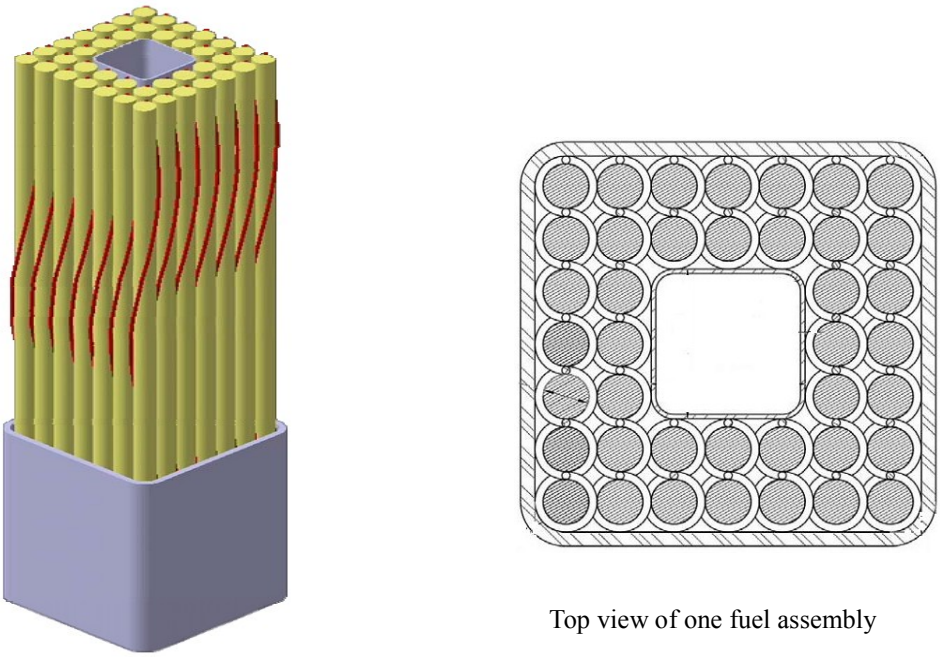

Top view of one fuel assembly

Figure 1–3: HPLWR fuel assembly with wire spacers by Himmel et al. [7]

In order to avoid such unwelcome scenario and enhance the mixing of coolant in sub-channels, wires wrapped around each fuel rod have been evaluated to be a promising spacer and mixing device, proposed by Schulenberg et al. [5]. As shown in Figure 1–3, one

fuel assembly has 40 pins wrapped by wires and a central water box for the moderator. The wrapped wires are capable to guarantee a cross mixing in both upward and downward flow of the coolant in the fuel assemblies and also to prevent the neighboring rods from coming close to each other due to the thermal stresses and the possible external forces.

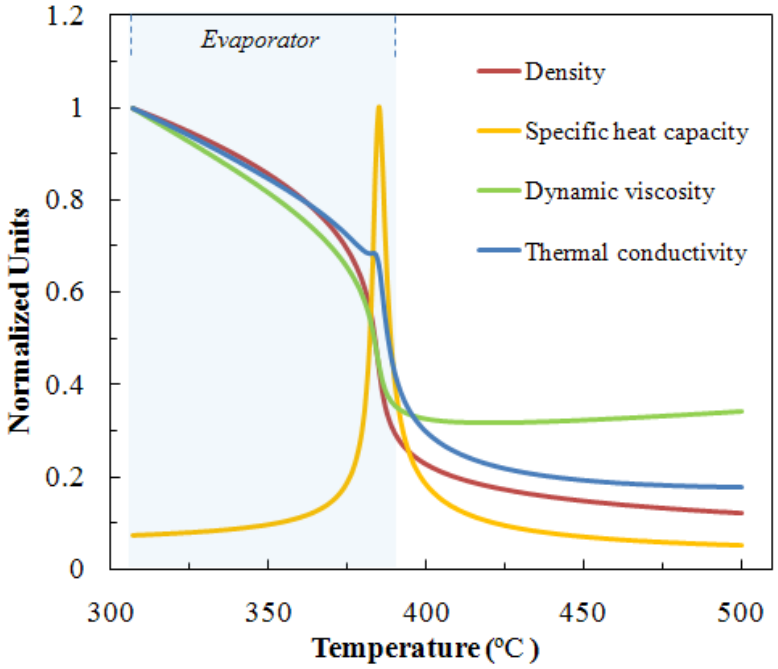

Figure 1–4: Normalized thermo-physical property variation of water as a function of temperature at 25 MPa, calculated by IAPWS-IF97 [8].

As illustrated in Figure 1–2, the water flows into evaporator at 310 ºC and leaves it at 390 ºC. It will pass through the pseudocritical temperature of 384.7 ºC at a system pressure of 25 MPa. The most significant thermo-physical property variations occur near this special temperature point, see Figure 1–4. The specific heat of water exhibits a maximum value within a very narrow temperature range in the vicinity of the pseudocritical temperature, varying by a factor of about 20. Thermal conductivity, density and dynamic viscosity also decrease dramatically near the pseudocritical point. Consequently, the heat transfer is strongly influenced by the strong changes in properties. In general, the experimental investigations show that there are three modes of heat transfer in fluids at supercritical pressures: 1) Enhanced Heat Transfer (EHT), the heat transfer is characterized by a larger value of heat transfer coefficient than those calculated by the standard Dittus-Boelter correlation; 2) Normal Heat Transfer (NHT), the heat transfer is similar to those of subcritical convective heat transfer which can be predicted by means of Dittus-Boelter correlation with a reasonable value; 3) Deteriorated Heat Transfer (DHT), this heat transfer occurs at a high heat flux and a relatively low mass flux and results in an abnormal increase on heated-wall temperature, (see Mokry et al., [9]). In order to keep the temperature

integrity of the fuel cladding, deteriorated heat transfer must be avoided to ensure a safe operation of the system in HPLWR. Therefore the behaviour of DHT in the upward channel flow has to be investigated comprehensively, and the onset of the deterioration in the coolant channel should be predicted as precisely as possible.

1.2 Status of Research and Development

1.2.1 Designs and Studies of Supercritical Water Reactor (SCWR)

In Europe, a consortium of 12 European partners of 9 Euratom members states has jointly been working on an innovative concept of a SCWR since 2000. This new type of reactor is called High Performance Light Water Reactor, which has been mentioned at the beginning of this thesis. The project plan is structured into working packages for design integration, core design, safety systems, materials, heat transfer, education and dissemination. Most work has been performed for a core with a thermal neutron spectrum, which is based originally on an assembly cluster design proposed by Hofmeister et al. [10]. The containment design with its safety and residual heat removal systems is based on the latest boiling water reactor concept. An additional passive safety system has been proposed by de Marsac et al. [11] to cause a forced convection through the core driven by steam. The core power distribution has been analyzed respectively by Maraczy et al. [12] using the two group diffusion code KARATE which was coupled with thermal-hydraulic code SPROD, and by Monti et al. [13] with the neutron transport code ERANOS coupled with the system code TRACE. The coolant mixing inside assemblies induced by wire spacer has been investigated by Himmel et al. [14]. The results demonstrated that wire spacer is capable of providing sufficient mixing to coolant. Corrosion tests at supercritical pressure and temperature of up to 650 ºC are being performed at VTT Industrial Systems. Latest results have been published by Pentillä et al. [15]. The prediction of the wall temperature is accomplished by a look-up table for heat transfer in supercritical water (Löwenberg, et al. [16]), restricted to heat transfer in smooth tubes, to vertically flow and to fully developed forced convection flow. However, deteriorated heat transfer is not yet covered in this table. Efforts by means of CFD regarding this topic have been made by Palko and Anglart [17], Zhu and Laurien [18] as well as Visser et al. [19], respectively. The onset of HTD can be captured by the current model with a proper resolution of the boundary layer. So far, the European project on the HPLWR has reached an enormous progress and further research is underway. More details have been summarized by Schulenberg and Starflinger [11].

In Japan, a conceptual study of the pressure-vessel type SCWR started at University of Tokyo in 1989. This conceptual study covers almost all aspects of conceptual design for both thermal and fast options. In 1994, a once-through cycle SCWR was developed by Oka

and Koshiyuka [20] [21].The design studies focused on several important issues of the core design, for instance, heat transfer analyses by Koshizuka et al. [22], plant start-up system design (Tin Tin Yi et al., [23]), a 3D neutronics/thermal-hydraulics coupled core design (Kamei et al., [24]) with subchannel analyses (Yamaji et al., [25]), fuel rod thermal/mechanical analyses (Yamaji et al., [26]), safety analyses including Loss of Coolant Accident (LOCA) (Ishiwatari et al., [27]), and so on. In 2005, a research project of a Super Fast Reactor has started in Japan (Ishiwatari et al., [28]). It aims at maximizing the power density and utilizing plutonium from the LWR spent fuel rather than the fuel breeding (Ishiwatari et al., [29]). An improved core has been designed to keep both overall and local void reactivity negative by updating the duel and core configurations (Cao et al., [30]). The estimation of nuclear transmutation capability and in-core structure design including mechanical analyses has also been performed (Cao et al., [12], [28]). In order to develop a basic thermal-hydraulic database for the Super Fast Reactor, a set of experimental tests have been carried out with HCFC22 as the work fluid. It started from a smooth circular tube (Mori et al., [31]) and afterwards to a 7-rod bundle (Mori et al., [32]). Besides the fast-spectrum concept, a new R&D project on thermal-spectrum SCWR concept was granted in 2008 [29]. Up to now, both of the fast and thermal options are ongoing in Japan.

The SCWR researches in Canada focus on the development of a pressure-tube design rather than the pressure vessel design. It is a nature extension of the Canada Deuterium Uranium (CANDU) reactor, referred to CANDU-SCWR. The preliminary design proposed by Khartabil et al. [33] indicated it has a potential thermal efficiency of 48% with a stable once-through fuel cycle. Basic designs are building on the extensive experience that has been accumulated from the current CANDU reactor. Nevertheless, material for in-core components is still a crucial point for this new reactor design. A study to obtain the data needed for materials selection and evaluation has been reported by Guzonas et al. [34]. A survey of experimental data on heat transfer of supercritical water is also carried out by Pioro and Duffey [35] aiming at the design criterion of cladding temperature limit. Considering the dynamic instability due to sharp variation in fluid properties, analytical models have been developed for predicting the onset of dynamic instability by Chatoorgoon et al. [36].

SCWR research in Korea is currently focusing on a feasibility study including the core conceptual design, supercritical heat transfer study and the investigation of corrosion effects on candidate materials. A conceptual design of a 1400 MWe reactor core with a solid moderator, ZrH_2, has been proposed by Joo et al. [37] and studied further by Bae et al. [38] and Kim et al. [12]. A passive safety system has also been involved in this initial design. On the topic of the heat transfer study, a set of experimental tests to supercritical CO_2 have been performed by Bae et al. [39] and Kim et al. [40] in order to obtain a deep understanding to the heat transfer behaviour at a supercritical pressure.

In 2005, the Shanghai Jiao Tong University started the first SCWR research activities in China. A preliminary reactor core with mixed neutron spectrum has been proposed by

Cheng et al. [41]. Other work on aspect of heat transfer investigation and materials test is summarized by Cheng [29].

1.2.2 Heat Transfer Investigations of Supercritical Fluids

The intensive work on the heat transfer of supercritical water was mainly performed since the 1950s along with the development of supercritical pressure boilers. Since then, a lot of works are devoted to the heat transfer of supercritical fluids. The majority of them are related to heat transfer in circular tubes cooled with water, carbon dioxide and helium at supercritical pressure. However, there is no consensus on the general trends in supercritical heat transfer. The studies mentioned in this chapter are restricted to fluids of water and carbon dioxide, flowing vertically upwards inside a circular tube or other geometries related to SCWR, by means of the experimental test and the numerical investigation.

Experimental Studies

Shitsman [42] analyzed the heat transfer experimental data of supercritical water flowing inside tubes and then generalized these data with the Dittus-Boelter type correlation:

$$Nu_b = 0.023\, Re_b^{0.8} Pr_{min}^{0.8} \tag{1-1}$$

The subscript "*min*" means minimum *Pr* value, i.e., either the *Pr* value evaluated at the bulk fluid temperature or the *Pr* value evaluated at the wall temperature. However, Shitsman assumed that thermal conductivity was a smoothly decreasing function of temperature near the critical and pseudocritical points. In his following investigations the impaired heat transfer at supercritical working conditions has been involved in. Later on, he [43] found that the impaired heat transfer took place only with a rising flow of the fluid and did not occur with a down coming flow. One set of his data [44] has been used to validate the results of CFD in chapter 2, which is characterized by "two-peak" variation on the wall temperature due to the impaired heat transfer.

Ackerman [45] investigated heat transfer to water at supercritical pressures flowing in smooth vertical tubes within a wide range of pressures, mass fluxes, heat fluxes and diameters. He found that a pseudo-film boiling phenomenon could occur at supercritical pressures, which can be the reason of the deteriorated heat transfer. One of the evidences was "boiling noise" at the onset of heat transfer deterioration, which has also been detected by Goldmann [46] and been heard under sub-critical pressure; Another evidence was the photographs presented by Nishikawa and Miyabe in 1956 [47], which are considered to be film boiling of supercritical pressure carbon dioxide under the free convection. However, a growing number of studies have indicated that the pseudo-film boiling theory could not stand up at all. The "boiling noise" did not appear in the experiments performed by Swenson et al. [45] and those by Shiralkar and Griffith [48]. Hall and Jackson [49]

considered that the phenomenon of bubble moving might be caused by the poor purity of the carbon dioxide, in other words, it is caused by the separation of multi-components.

Swenson et al. [45] carried out a set of test to supercritical water in an open-circuit test apparatus. They found that the heat transfer coefficient (h) has a peak when the film temperature is within the pseudocritical temperature range. This peak decreased with increase of the pressure and the heat flux. The results also revealed that the bulk fluid enthalpy corresponding to the maximum h is slightly less than the pseudocritical bulk fluid enthalpy. Similar results were reported by Yamagata et al. [50]. In addition, Swenson et al. found that conventional correlations did not work well near the pseudocritical point. Therefore a new correlation was recommended by them:

$$\frac{hD}{k_w} = 0.00459\left(\frac{DG}{\mu_w}\right)^{0.923}\left(\frac{H_w - H_b}{T_w - T_b}\frac{\mu_w}{k\mu_w}\right)^{0.613}\left(\frac{\rho_w}{\rho_w}\right)^{0.231} \tag{1-2}$$

The new correlation improved the accuracy of agreement between measurements and predictions. However, they made the same assumption as Shitsman that the thermal conductivity was a smoothly decreasing function of temperature near the critical and the pseudocritical points.

The experimental works performed by Bishop et al. [51] [52] were in a frame of designing supercritical light water reactor. These experimental tests to the supercritical water flowing upward inside tubes and annular channels have covered a wide range of flow and operation parameters. The smallest tube diameter is 2.54 mm and the majority of the data sets were obtained with high heat fluxes (maximum of 3.46 MW/m^2). Their data for heat transfer in tubes were generalized using the following correlation:

$$Nu_x = 0.0069\, Re_x^{0.9}\, \overline{Pr}_x^{0.66}\left(\frac{\rho_w}{\rho_b}\right)_x^{0.43}\left(1 + 2.4\frac{D}{x}\right) \tag{1-3}$$

where x is the axial location along the heated length and D is the tube diameter.

Krasnoshchekov and Protopopov [53] [54] investigated the heat transfer at supercritical region in flow of carbon dioxide and water in tubes. They derived a correlation for forced convective heat transfer in the water and the carbon dioxide at supercritical pressures, in which the Pr and specific c_p were averaged over the ranges to account for the thermo-physical property variations. Later, Krasnoshchekov et al. [55] [56] modified their original correlation to a new form as follows:

$$Nu = 0.95\, Nu_0\left(\frac{\rho_w}{\rho_b}\right)^{0.3}\left(\frac{\bar{c}_p}{c_{pb}}\right)^n\left[1 + \left(\frac{x}{D}\right)^{0.8}\right] \tag{1-4}$$

$$Nu_0 = \frac{(\xi/8)Re_b\overline{Pr}}{12.7\sqrt{\xi/8}\left(\overline{Pr}_b^{2/3}-1\right)+1.07} \tag{1-5}$$

The power index n depends on the ratios of T_w / T_{pc} and T_b / T_{pc}. This correlation took the tube entrance region into account by using the axial heated length (x) and the tube diameter (D). The Darcy friction factor (ξ) in Equation (1-5) can be calculated by Filonenko formula as follows:

$$\xi = \frac{1}{(1.82\ log_{10}^{Re_b}-1.64)^2} \tag{1-6}$$

Ornatskii et al. [57] investigated the heat transfer of water with rising and falling flow at supercritical pressures in a tube with the diameter of 3 mm. They found that the deteriorated heat transfer can be observed at supercritical pressures both with rising and falling flows of water, depending on the ratio of heat flux over mass flux density and also flow conditions. In 1972, Ornatskii et al. [58] investigated the normal and the deteriorated heat transfer in a vertical annular channel (external tube heating). The deteriorated heat-transfer zone was observed visually as a red hotspot, appearing in the upper section of the test tube. The hotspot zone becomes more obvious with the increase in heat flux.

Glushchenko et al. [59] conducted experiments with an upward flow of water in vertical tubes and in vertical annular channels by means of external and internal one-side heating at supercritical pressure. They found that the beginning of the heat transfer deterioration shifted towards lower enthalpies of the fluid with the increase in heat flux. In addition, the heat transfer restorations have also been observed in the cases of tubes. In general, the results of the investigation showed that variations in wall temperature of a heated tube and of an annular channel were similar when the tubes and annular channels are fairly long. However, in the cases of deteriorated heat transfer, no decrease in the wall temperature (heat transfer recovery) was observed in the experiments for annular channels. In 1972, Glushchenko and Gandzyuk [60] published the investigation results of temperature conditions at the wall of an annular channel. The width of the annular gap was only 1 mm with a length of 600 mm. It is worth to be mentioned that these results of upward flowing in an annular channel are the only available published data with internal heating rather than those with external heating performed by Ornatskii [58]. It was found that, for the mode of normal heat transfer, the dependence of the Nu number on Re and Pr remained almost the same as in the case of constant physical properties. They recommended the following equation to predict the wall temperature in the mode of normal heat transfer:

$$Nu = 0.017\ Re^{0.8}\ \overline{Pr}^{0.4}\left(\frac{\overline{Pr}}{Pr_w}\right)^{0.25}\left(\frac{d_2}{d_1}\right)^{0.18} \tag{1-7}$$

where d_2 and d_1 are the tube inner diameter and rod outer diameter, respectively. For the mode of deteriorated heat transfer, Glushchenko and Gandzyuk recommended the Equation (1-4) developed by Krasnoshchekov et al. [56]. They found that the calculated values of the wall temperature agreed qualitatively with those in experiments. However, there are still around 30% deviation existing.

The data from Yamagata et al. [50] is perhaps one of the most popular dataset used for the validation of numerical models. They investigated forced-convective heat transfer to supercritical water flowing in tubes and found that for water flowing in vertical and horizontal tubes the heat transfer coefficient increases significantly in the pseudocritical region. The magnitude of the peak of the heat transfer coefficient decreases with the increase of the heat flux and the pressure. The maximum coefficient values correspond to a bulk-fluid enthalpy, which is slightly less than the pseudocritical bulk-fluid enthalpy. It should be mentioned that when the measured inlet bulk-fluid temperature is close to pseudocritical or critical temperatures, the value of inlet temperature cannot be reliably used as the starting point for downstream bulk-fluid temperature calculations. They mentioned that there are significant variations in thermo-physical properties near the pseudocritical and critical points. These variations consequently lead to increased uncertainties in calculations. Therefore, a value of the measured test-section outlet bulk-fluid temperature should be used for upstream bulk-fluid temperature calculations. In addition, Yamagata et al. [50] recommended the following correlation:

$$Nu = 0.0135\, Re_b^{0.85} Pr_b^{0.8} F_c \tag{1-8}$$

The value of last term F_c depends on the ratios of $(T_{pc} - T_b)$ and $(T_w - T_b)$. In addition, Yamagata et al. [50] proposed the following relationship between the mass flux density and the heat flux for predicting the onset of heat transfer deterioration: $q=0.2 \cdot G^{1.2}$.

Kirillov et al. [61] conducted research into a radial cross-section temperature profile in water flowing in a circular tube at subcritical and supercritical pressures. They found that inside the turbulent flow core, the radial cross-section temperature profile is logarithmic at supercritical pressures and at temperatures close to the pseudocritical temperature. In 2005, Kirillov et al. [62] performed an experimental study on heat transfer to supercritical water in vertical tubes. This study aimed to obtain a new set of heat transfer data as a reference dataset for comparison with supercritical water bundle and for the verification of scaling parameters between water and modeling fluids. In addition, based on Bishop's equation (Equation (1-3), Kirillov suggested a corrected correlation, in which the entrance-region effect is not considered anymore and the constant is also changed. The format of the new equation is shown as follows:

$$Nu_x = 0.0052\, Re_x^{0.9}\, \overline{Pr}_x^{0.66} \left(\frac{\rho_w}{\rho_b}\right)_x^{0.43} \tag{1-9}$$

The succeeding work carried out by Kirillov and Grabezhnaya [63], Pioro and Kirillov [64] presented the results of comparison between the new experimental dataset and different correlations. They found that the modified correlation has a good agreement with the experimental heat transfer coefficients outside the pseudocritical region. However, this correlation slightly under-predicted the heat transfer coefficients within the pseudocritical region and cannot accurately predict within the regime of deteriorated heat transfer.

Recently, Licht et al [65] performed a series of integral heat transfer measurements in a square annular channel for bulk water temperatures of 175-400 ºC with upward mass flux densities of up to 1000 kg/m^{2}s, heat fluxes of up to 440 kW/m^2 and all at a system pressure of 25 MPa. Mean and turbulent velocities have been measured by a two component laser Doppler velocimetry system. Experimental data were later on compared along with simulations by using the CFD code FLUENT. The comparison results were used to explain the deterioration and enhancement of heat transfer in supercritical water. They recommended that this experimental measured heat transfer and local velocity data can serve as a database to validate CFD models, such as Reynolds-averaged Navier-Stokes (RANS) equations and possibly even large Eddy simulations (LES) and direct numerical simulations (DNS).

Li et al. [66] performed experimental studies on heat transfer of supercritical water flowing upward around a wire-wrapped rod in a square vertical channel. Experimental conditions included pressures of 23-25 MPa, mass flux densities of 500-1200 kg/m^{2}s and heat fluxes of 200-800 kW/m^2. The experimental Nusselt numbers were compared with those calculated by empirical correlations for smooth tubes. The results indicated that the Jackson correlation (Equation 1-10) showed better agreement with the test data compared with the Dittus-Boelter correlation. However it over-predicted the Nusselt numbers almost within the whole range of experimental conditions. Comparison of experimental data at two different supercritical pressures showed that the heat transfer was more enhanced at a lower supercritical pressure but the deterioration was also more likely to occur at the higher pressure. It was also found that the wrapped-wire does not enhance the heat transfer significantly under the mode of the normal heat transfer, but it does contribute to the improvement of the heat transfer under the mode of the deteriorated heat transfer, the mode at a high heat flux and a relative low mass flux density. These data have been used by in this thesis to validate the numerical model. The computational results indicated a conclusion regarding the wire effect.

Carbon dioxide is the most investigated fluid in supercritical regions after water due to the similar thermo-physical behaviour under supercritical conditions and the lower cost to conduct experiments. The experimental investigations on supercritical carbon dioxide started in 1950’s. Most of the recent experiments were carried out for the purpose of SCWR design.

Hall and Jackson [67] performed experimental investigations of heat transfer to supercritical carbon dioxide in both upward and downward directions in a vertical circular tube. The deteriorations were observed in the heat transfer of fluids flowing upward in tubes. It is concluded that the buoyancy forces cause the reduction of shear stress in the wall layer and consequently impaired the turbulent diffusion. In 2002, Jackson [68] modified the original correlation of Krasnoshchekov et al. Equation (1-4) for forced-convective heat transfer in water and carbon dioxide at supercritical pressures:

$$Nu = 0.0183\, Re_{\mathrm{b}}^{0.82}\, Pr_{\mathrm{b}}^{0.5} \left(\frac{\rho_w}{\rho_b}\right)^{0.3} \left(\frac{\bar{c}_p}{c_{pb}}\right)^{n} \tag{1-10}$$

The power index n depends on the ratio of T_w / T_{pc} and T_b / T_{pc}, which has been found to be very effective for reflecting the effect of a temperature increase in a thermal boundary layer near a wall.

Fewster and Jackson [69] conducted heat-transfer experiments in turbulent flow of carbon dioxide inside vertical tubes at supercritical pressures. The objective of these experiments was to investigate various regimes of heat transfer at supercritical conditions. They found that three modes of heat transfer at supercritical pressures exist. Those are normal heat transfer, improved heat transfer and deteriorated heat transfer.

Kim et al. [70] performed a set of experiments on the heat transfer of supercritical carbon dioxide flowing upward in a vertical circular tube. They compared the measured results with four existing correlations. The comparison indicated that the Jackson and Fewster correlation showed the best prediction quality. In addition, two criteria on the onset of deteriorated heat transfer are compared with the test data as well. Both criteria describe fairly well the experiments even though they are based on the experiments with different medium and working conditions.

Bae and Kim [71] summarized the extensive experiments on a heat transfer to a vertically upward flowing carbon dioxide at a supercritical pressure in tubes and in an annular channel which they performed since 2006. Based on the Jackson correlation (Equation (1-10)), a new correlation, which covers both a deteriorated heat transfer mode and a normal heat transfer mode, was developed for relevant ranges of Bu.

$$Nu = Nu_{ref}\, f(Bu) \tag{1-11}$$

The value of Bu is calculated individually in five different sub-regions in order to take the difference of the effect of buoyancy into account. It has been validated by published data for carbon dioxide and water. A fairly good agreement between the predictions and the measured data was achieved especially when the buoyancy effect is severe.

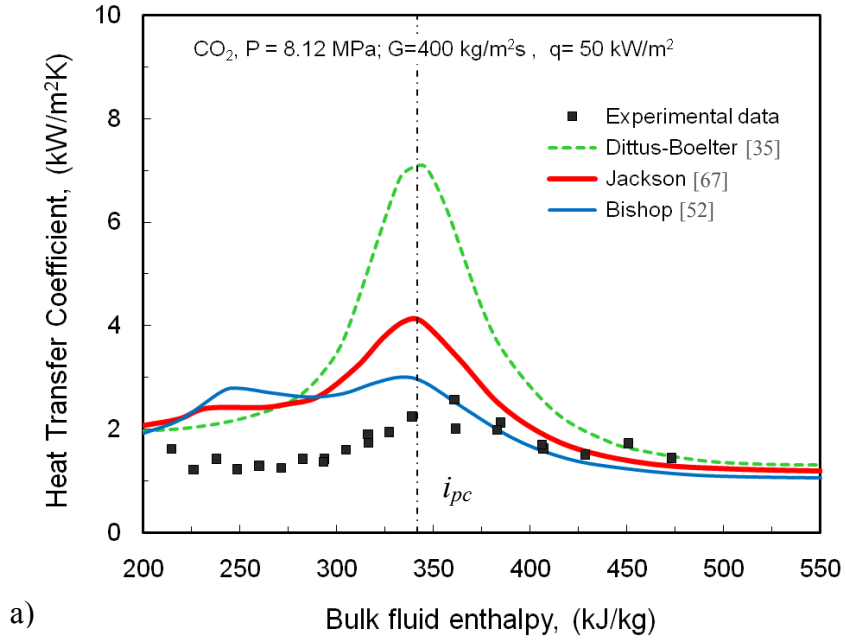

a)

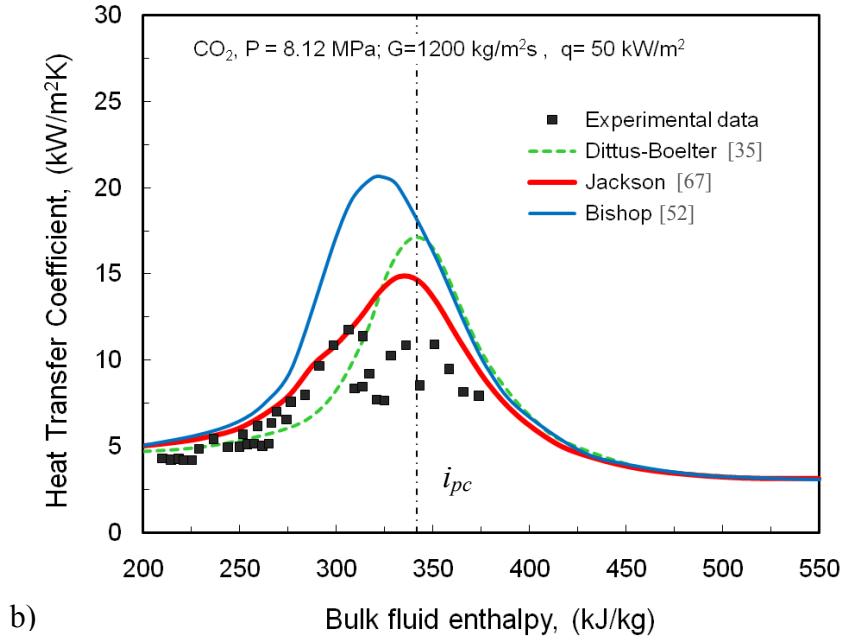

b)

Figure 1–5: Comparison of various correlations with experimental data [71]: Carbon dioxide, vertical annular channel (upward flow), D_{rod}=8mm, D_{tube}=10mm, a): deteriorated heat transfer, b): normal heat transfer.

As always, derivation of this new correlation was based on their own dataset. The comparison of experimental data and other's correlations still shows considerable disagreement, especially in the mode of the deteriorated heat transfer, see Figure 1–5. This is one of the most insufficiencies of the empirical correlations that one correlation mostly provides a good prediction only with the "derivation-based" dataset. Therefore, the analytical studies become necessary in order to obtain more insight into the heat transfer behaviour in supercritical fluids.

CFD Studies

Apart from the experimental study, the heat transfer behaviour to supercritical fluids in circular tubes and annular channels has been studied by using Computational Fluid Dynamics (CFD) codes as well. The purpose of these studies is to provide a better understanding of the heat transfer mechanism and to predict the heat transfer coefficient in supercritical fluids more precisely. Until now, satisfactory analytical methods have not yet been developed due to the difficulty in dealing with the steep property variations, especially in turbulent flows and at high heat fluxes. The buoyancy effect and acceleration effect near the pseudocritical point have not been fully verified in the conventional turbulent models. Moreover, Prandtl number, which is usually assumed as a constant in turbulence models but varies strongly in reality, can lead to a considerable error of the numerical results.

Deissler [72] and Schnurr et al. [73] took the effect of variable fluid near the heated wall into account by approach of modifying eddy viscosity in turbulence model. Shiralkar and Griffith [48] used a similar approach to study the effect of different parameters on the heat transfer coefficient and the behaviour of heat transfer deterioration. They found that the numerical results over-predicted the temperature on the heated wall under the mode of deteriorated heat transfer. Furthermore, the computational results indicated that the onset of heat transfer deterioration is due to the reduction in shear stress near the heated wall. It needs to be mentioned that a constant turbulent Prandtl number was used in both of studies.

With the development of the computer capability in recent years, advanced turbulence models have been applied in numerical studies towards supercritical fluids, such as the widely used k-ε and k-ω two-equation turbulence models, which offer a good compromise between numerical effort and computational accuracy. Many studies have been carried out to assess the performance of ε-based and ω-based two-equation turbulence models in terms of their ability to predict the heat transfer behaviour in supercritical fluids.

In order to take the gravity effect into account, Bellinghausen and Renz [74] resolved the near-wall region by using the low Reynolds k-ε model [75] and introduced an additional term to the turbulence model. They found that mainly due to the increase in the specific heat capacity, heat transfer enhancement occurs at low heat fluxes and the bulk fluid temperature close to the pseudocritical point. At high heat fluxes, heat transfer deterioration is obtained over a wide length in upward flows.

Koshizuka et al. [76] carried out a numerical analysis to deteriorated heat transfer in a vertical pipe. The calculation is based on a parabolic solver for steady-state equations. The low Reynolds k-ε model is used in simulations. In the model, non-uniform grids were employed in order to adapt to the strong variations of properties. The mesh adjacent to the wall has the minimum width, where the non-dimensional distance y^+ is lower than 0.1. The calculated results were compared with the experimental data of Yamagata et al. [50] and showed a good agreement.

He et al. [77] [78] performed computational simulations of turbulent mixed-convection heat transfer to supercritical carbon dioxide by solving several two-equation low Reynolds turbulence models. The mesh was compressed towards the heated wall in order to make the non-dimensional distance y^+ lower than 0.5. These studies were aimed at evaluating the performance of these models in terms of their ability to predict heat transfer under conditions of very strong influence of buoyancy. To some extent, the simulations were able to reproduce the effects of very strong influences of buoyancy forces on the heat transfer. However, the models were not able to predict exactly the onset of such effect in comparison with the experimental data [69]. The latest studies performed by He et al. [79] in 2008 were aimed to assess the performance of different low Reynolds turbulence models by comparing with Direct Numerical Simulation (DNS) in supercritical carbon dioxide [80]. Results indicated that most turbulence models tested reproduce the recovery of turbulent kinetic energy reasonably well, but cannot predict the improvement on heat transfer in the strongly buoyancy-influenced cases.

Seo [81] performed studies on heat transfer and flow phenomena in supercritical water using the commercial CFD code FLUENT. The standard k-ε turbulence model and the standard wall function proposed by Launder and Spalding [82] were used in calculation. The non-dimensional distance y^+ is equal to 30. Experimental data from Yamagata et al. [50] and Shitsman [44] have been used to compare with calculated results. Simulations showed a good agreement with measurements under high mass flux density conditions, where buoyancy effects can be neglected. However, the model cannot predict the localized heat transfer deterioration under high heat flux and low mass flux density conditions.

A comprehensive sensitivity study of different turbulence models to the heat transfer in supercritical fluids was carried out by Kim et al. [83]. The vertical upward flow of water in a heated tube at a supercritical pressure was numerically simulated by commercial CFD code FLUENT. In order to examine the reliability of the turbulence model at the supercritical flow, a series of simulations were performed with different turbulence models, such as the standard k-ε turbulence model, the standard k-ω turbulence model, the Shear Stress Transport (SST) k-ω turbulence model developed by Menter [84], the Renormalisation Group (RNG) k-ε turbulence model [85] and several Low-Reynolds number k-ε turbulence models. Again, the experimental data of Yamagata et al. was used to compare with the computational results and to verify the performances of those different turbulence models. Results indicated that the best prediction is obtained by the RNG k-ε turbulence model with the enhanced wall treatment ($y^+ < 1$). It is notable that the Boussinesq's approximation is used to model the density change by the temperature variation in the turbulence kinetic energy transfer equation. This treatment decreased the turbulence kinetic energy when the temperature field is stable.

Roelofs and Komen [86] carried out a sensitivity study of the non-dimensional distance to the wall (y^+) based on the work performed by Kim et al. [83]. The RNG k-ε turbulence mode was used with different wall treatment in which the value of y^+ varied from 0.1 up to

40. As usual, experimental data of Yamagata et al. [50] was used to compare with calculated results. They found that changing the value of y^+ from 0.1 to 40 resulted in a quite limited differences regarding on wall temperature. However, when the heat transfer coefficient was considered, deviation between the various computations with different y^+ values were considerable larger. They recommended that y^+ values from 0.1 to 1 should be applied to the wall treatment.

Cheng et al. [87] investigated numerically the heat transfer of supercritical water in various flow channels by using the commercial CFD code CFX 5.6. The purpose of this work was to obtain a basic knowledge of the heat transfer behaviour for the design of SCWR and to gather the first experience in the application of CFD codes in supercritical fluids. The effects of mesh structures, turbulence models and flow channel configurations were analyzed systematically. Based on the comparison between numerical results and experimental data, the accuracy and applicability of various turbulence models were assessed. Cheng et al. [87] concluded that the ω-based turbulence models coupled with automatic wall treatment are not recommended for further application to simulate the heat transfer in supercritical fluids. The ε-based turbulence models, such as Renormalization Group (RNG) k-ε turbulence model [85] and Speziale-Sarkar-Gatski Reynolds Stress Model (SSG RSM) [88], could result in a good agreement with experimental data when y^+ is smaller than 40. At the end of this publication, they mentioned that the conclusions achieved are only valid for the parameter ranges considered, and the further study is needed.

Yang et al. [89] performed another model sensitivity study by using the commercial CFD code STAR-CD 3.24. This investigation aims at having more understandings about the phenomena happening in supercritical water and for designs of SCWR. Thirteen different two-equation turbulence models were selected to carry out to simulate heat transfer in supercritical water flowing upward in a circular tube. The calculated results were compared with experimental data of Yamagata and other correlations to find suitable models for predicting heat transfer in supercritical water. Based on the results of comparisons, which were carried out both in low bulk temperature region and in high bulk temperature region, Yang et al. found that the two-layer model (Hassid and Poreh [90]) gave a better prediction to the heat transfer than other models. The standard k-ε high Reynolds number model with the standard wall function also showed an acceptable predicting capability. The standard k-ω model and the SST k-ω model gave much lower prediction of the heat transfer coefficients in the pseudocritical temperature region.

In the CFD studies mentioned above, RNG k-ε turbulence model or other ε-based turbulence models are recommended to predict the heat transfer of supercritical fluids. However, it is notable that these conclusions are all based on the validation only with Yamagata experimental data. Furthermore, the enhanced wall treatment was even not considered in some cases. Some authors also mentioned that these conclusions are only valid for the calculations used in this study and further study need to be carried out. Recently, The Shear Stress Transport (SST) k-ω turbulence model developed by Menter

comes into sight. Results of comparison with other experimental data rather than those from Yamagata et al. indicate that SST k-ω turbulence model with enhanced wall treatment has a good ability to predict the heated wall temperature, in particular in mode of deteriorated heat transfer which cannot be well predicted by RNG k-ε turbulence model.

Palko and Anglart [91] performed a numerical investigation of the heat transfer deterioration phenomena using commercial CFD code CFX 11.0. The SST k-ω turbulence model and the standard k-ε turbulence model were used in the calculations. Water properties are coming from the standard IAPWS tables [8]. As the validation of different cases against the experimental data from Ornatskii [57] proved, the SST k-ω turbulence model is fully capable to model the heat transfer to supercritical water even in the deteriorated region, where the standard k-ε model totally failed to predict the heat transfer. Palko and Anglart thought the main reason for the substantial difference in results for these two turbulence models is the near wall treatment. SST k-ω turbulence model allows to resolve the boundary layer numerically. Standard k-ε turbulence model approximates the boundary layer by wall functions with a coarse grid ($y^+ > 5$), which are not suitable for the flows where the thermo-physical properties change rapidly close to the wall. For a finer grid ($y^+ < 1$), the non-linear damping functions required by standard k-ε turbulence model cause the loss of accuracy and consequently result in a considerable deviation from experimental data. In order to examine the influence of buoyancy on heat transfer, they carried out a number of simulations with SST k-ω turbulence model [92]. The results were compared with two sets of experimental data, one at a low coolant mass flux density (G = 430 kg/m^{2}s) by Shitsman [44] and another at a high coolant mass flux density (G = 1500 kg/m^{2}s) by Ornartskii et al. [57]. Results indicated that the heat transfer deterioration at the low mass rate is mainly caused by the influence of the buoyancy which is however negligible for the case at a high mass flux density. Other mechanisms involved in high mass flux density case are the streamwise acceleration and variations in thermo-physical properties.

Visser et al [93] performed a CFD study on heat transfer behaviour in supercritical carbon dioxide upward flows in a tube by using the commercial CFD code FLUENT 6.2. The SST k-ω turbulence model was used with enhanced wall treatment ($y^+ < 1$). Experimental data of Kim et al. [70] has been used to compare with the calculated results. Visser et al. found that the k-ε turbulence model performed better at a high mass flux and the SST k-ω turbulence model seemed to perform better at a low mass flux. Moreover, the SST k-ω turbulence model was suitable to capture the changes in the flow structure which are associated with heat transfer deterioration (HTD). This was further confirmed by sensitivity analyses of properties. Chandra et al [94] extended this study and performed 2D and 3D analysis to demonstrate the potential effect induced by the wire. Results showed that the introduction of the helical wire wrap has a large effect in preventing the occurrence of HTD.

In order to make a further progress to current models based on RANS equations rather than performing the models sensitivity study, Laurien et al. [95] performed a one-dimensional (1D) analysis which allows easy testing of a new model when the effect of downstream flow

development can be neglected. The molecular heat capacity is modified to account for the large fluctuations of properties around the time-mean location of the pseudocritical region. The Reynolds stresses are modeled by the k-ω turbulence model, which is based on the standard eddy viscocity μ_t. In the study the viscous sub-layer was always resolved ($y^+ < 1$) and the commercial CFD code CFX 10.0 was used in all simulations. The results demonstrated the significance of recognizing the difference between the turbulent heat capacity $\overline{c_p}$ and the molecular heat capacity $c_p(\overline{T})$ which is based on Reynolds-averaged temperature. Results also showed that such a model has the potential to improve predictions within the pseudocritical region. As a successive work, Laurien and Rashid [96] carried out a 1D investigation on overheated zones along the wall of strongly heated pipe flow at a supercritical pressure by using the k-ω turbulence model. They found that the onset of overheating can be simulated with 1D model in reasonable agreement with experiments. Based on the results, it is further confirmed that the deterioration in Ornatskii et al. [57] is caused by the decrease in heat conductivity in a layer close to the heated wall, where an insulating viscous sub-layer of low conductivity is formed. Additionally, they pointed out that the most important factor, which a turbulence model has to capture in order to predict the onset of deterioration, is an accurate prediction of the thickness of the laminar sublayer. It is notable that the k-ω turbulence model without any modification is capable to capture this important effect.

Bae et al. [80] [97] performed numerical investigations by means of DNS in order to examine the heat transfer characteristics of turbulence to supercritical fluids flow both in vertical pipes and annular channels under strong buoyancy conditions. The work fluid is the supercritical carbon dioxide with Reynolds numbers of 5400 in pipes and 8900 in annular channels. The temperature peaks on the heated wall were developed in upward flows as a result of a rapid change in turbulence in the flow direction. Bae et al. examined various turbulence statistics and their respective buoyancy production terms to understand the role of free convection in such rapidly changing turbulent flows. Among the various turbulence statistics, the streamwise turbulent heat flux was found to have the most complicated transitional behaviour. Changing its directions as well as its magnitudes under strong influence of buoyancy will cause a rapid rise and fall of the wall temperature in upward flows. Compared to forced convection, the flow acceleration was much stronger in mixed convection due to buoyancy force. They also performed the comparison with empirical correlations. Results showed that the modified Krasnoshchenkov-Protopopov correlation (Equation 1-10) provided a good agreement with DNS in forced convection except for overpredictions in range of $T_b < T_{pc} < T_w$.

Besides the effort to supercritical water flows in simple geometries (circular tubes, annular channels and squared annular channels) as mentioned above, the CFD work on the aspects of complex geometries, for example, a square assembly with 40 fuel rods wrapped by wires relevant to the HPLWR design, have also been performed in recent years.

Laurien and Wintterle [98] performed a CFD investigation for a 1/8 fuel element of a preliminary HPLWR assembly without wire spacer. The aim was to gain insight into the resulting flow patterns as well as into temperature and density distributions within various subchannels. This study confirmed the earlier results obtained by subchannel analysis, which indicated that the axial mass flux is significantly reduced in the corner subchannel of this fuel element. Furthermore, results also provided an estimation of the magnitude of the secondary flows.

Kiss et al. [99] [100] performed 3D simulations for the 1/4 fuel assembly and a whole fuel assembly with one revolution of wrapped wire spacers corresponding to the HPLWR design. It was found that the wire spacers improve the additional mixing and a circulating flow near the outer and inner regions of the fuel element. Some flow features associated with the complex 3D flow with significant transverse velocity components are visualized as the first evaluated result of this investigation. Study of the temperature distribution on rod surface was not yet involved in this investigation due to the use of the wall function.

Himmel et al. [101] carried out three-dimensional CFD calculations of flow in a part of a HPLWR fuel assembly with the wire spacers by using the commercial CFD code STAR-CD 3.26. The aim was to determine the mixing coefficients for the use in the following subchannel analysis. Results confirmed that the forced convective mass transfer induced by the wires dominates over the turbulent mass exchange between subchannels. As a succeeding work, subchannel Analysis of a HPLWR Fuel Assembly with one wire revolution was performed by Himmel et al. [14] based on the isothermal and steady-state analyses. The aim was to demonstrate that the commercial CFD code could be used for full rod bundle analysis by applying minor modifications to it. Results showed that volume forces acting on the fluid cells have enough capacity to account for the impact on flow field of the wires without need of modeling them physically.

Other Studies

Instead of experimental studies and CFD studies, a pragmatic approach to predict heat transfer in flows of supercritical water is the use of a look-up table based on dimensional parameters. It is a cheaper approach compared with running an experimental test and a more precise approach compared with CFD studies to predict the behaviour of the heat transfer. Löwenberg et al. [16] generated a look-up table for heat transfer of supercritical water, which is restricted to heat transfer of supercritical water in smooth tubes, to vertically upward flow and to fully-developed forced convection flow. It is a function of mass flux, heat flux, pressure, tube diameter and bulk enthalpy. The aim of this table is to improve prediction of heat transfer especially in the vicinity of the pseudocritical point, where the look-up table is able to predict the wall temperature with much higher accuracy than any published correlations. A comparison with experimental data used to build up this table shows a mean error of -1.7% and a standard deviation of 10.2%. It clearly shows the advantageous of this look-up table compared to the best available heat transfer correlations.

However, deteriorated heat transfer cannot be covered by this table due to its complex mechanisms.

Exclusion of the HTD in the look-up table is because various mechanisms are involved in the onset of HTD. Anglart [103] performed an investigation to evaluate the importance of particular mechanisms for the onset of HTD. Two tables are generated to list the various criteria for the onset of HTD and to rank the key parameters that are governing the onset of HTD in general and particularly for the HPLWR. As a result, he pointed it out that there are many expressions for the onset of HTD. However those expressions result in very often non-consistent predictions. Therefore the further experimental work needs to be performed to elucidate the various deterioration mechanisms.

1.3 Aim of this Study

In the HPLWR core design, the supercritical water flows into evaporator at 310 ºC and leaves it at 390 ºC. That means, the most significant thermo-physical property variations will occur in the upper part of the evaporator due to the pseudocritical temperature of 384.7 ºC at pressure of 25 MPa. As a consequence of the properties variations, heat transfer is strongly influenced by the changes in properties and could not be predicted by the conventional heat transfer correlations. Additionally, the heat transfer deterioration must be avoided to ensure the safe operation of the system in HPLWR in order to keep the temperature integrity of the fuel cladding. Therefore the mechanisms of HTD in upward channel flow have to be comprehensively investigated. Additionally, the onset of HTD should also be predicted by the model as precisely as possible. Apart from the abnormal heat transfer behaviour, the introduction of the wire spacer in HPLWR design significantly influence the heat transfer behaviour in the core, such as the “sweeping flow” reported by Kiss et al. [100] and Himmel et al. [101] and the local hotspots of the cladding temperature near the contact place between the wire and the fuel rod. This kind of complex, three-dimensional flow situations induced by wire also needs to be investigated in order to understand and quantify the effect of the wire.

The first aim of this study is to better understand the behaviour of the heat transfer of water under supercritical pressure by means of CFD. In particular, the mechanisms of HTD have obtained special attentions because of its self-evident importance to the security of HPLWR. A circular tube (or an annular channel) has been chosen as the first basic geometry in the numerical model for the sake of an easily validation by experimental data. Apart from the first basic geometry, a square annular channel and a square channel with a wire-wrapped rod inside have been chosen to investigate the “geometry effect” and the “wire effect”. Chapter 2 presents the turbulence models sensitivity study and the validations compared with several

experimental datasets corresponding to different geometries. The analysis of the local properties variation in chapter 3 reveals the mechanisms of the onset of the deterioration.

Additionally, a modified heat capacity, which takes the temperature fluctuation into account, is derived in chapter 2 and introduced into the turbulence model instead of the original time-mean heat capacity. With this model modification the better agreement to experiments is obtained, which indicates a potential improvement on the turbulence model dealing with the heat transfer in supercritical fluids.

The second aim of this study is to predict the heat transfer behaviour on geometries and working conditions relevant to the HPLWR design. Based on the validated model, the correction factors used in the heat transfer correlation are derived, which can be implemented into subchannel codes for safety analyses. A high-quality structured mesh has been generated for the geometry of a wire-wrapped rod in a square channel. This mesh fulfils the requirements of both of fully-resolved boundary layer and a reasonable number of the cells. The investigation of the deteriorated heat transfer and the local hotspot is a new task for such geometry, which therefore has been carried out and presented in chapter 4.

2 Numerical and Physical Model

A proper turbulence model is always crucial to a correct prediction on the heat transfer behaviour in supercritical fluids and so does the model configuration. In this chapter, different turbulence models have been discussed in aspect of the performance in supercritical fluids. Furthermore, sensitivity studies on the model configurations are also presented here.

2.1 Turbulence Modeling

It has long been recognized that computational modeling can potentially play a very valuable role in improving the understanding of the physics of convective heat transfer to fluids at supercritical pressure and assist with the development of correlations for engineering applications. A number of such studies have been reported in chapter 1.2.2. For modeling turbulence in CFD three well-developed approaches can be identified: Direct Numerical Simulation (DNS), which is only available at relative low Reynolds numbers with present computational power and therefore out of the consideration in this thesis; Large Eddy Simulation (LES), which requires fine grids and small time steps and hence also leads to high computational needs; Reynolds-Averaged Navier-Stokes (RANS) approach which uses time averaged quantities and has the advantages to shorten the computing time. At present, a general consensus of the performance of RANS turbulence models has not been achieved and the heat transfer process of supercritical fluids flowing in a simple channel can be described as a thermodynamically steady process. Hence, there is still plenty of scope for the further work to take advantages of recent developments in both turbulence modeling and numerical methods in order to improve the predictive capability to the turbulent flow and the heat transfer in the supercritical fluids. In this thesis, the two-equation RANS models will be used and discussed in the following chapters.

2.1.1 RANS Equations

The heat transfer process of fluids under a supercritical pressure can be described as a thermodynamically constant-pressure process, which is a typical assumption for most of heat transfer problems in low-speed incompressible flows with varable density. The general

governing equations which are suitable for the simulation of flow and heat transfer with supercritical fluids are:

Continuity of mass:

$$\frac{\partial \rho}{\partial t} + \frac{\partial}{\partial x_i}(\rho u_i) = 0 \tag{2-1}$$

Momentum equations:

$$\frac{\partial \rho u_i}{\partial t} + \frac{\partial}{\partial x_j}(\rho u_j u_i) = -\frac{\partial p}{\partial x_\mathrm{i}} + \frac{\partial \tau_{ij}}{\partial x_\mathrm{j}} + \rho g \tag{2-2}$$

Energy equation:

$$\frac{\partial \rho c_p T}{\partial t} + \frac{\partial}{\partial x_j}(\rho c_p u_j T) = \frac{\partial}{\partial x_j}\left(\lambda \frac{\partial T}{\partial x_\mathrm{j}}\right) + \frac{\partial}{\partial x_j}(u_i \tau_{ij}) \tag{2-3}$$

In the above equations, u_i denotes a velocity component($u_i = [u_1, u_2, u_3] = \vec{u}$) and x_i stands for a coordinate direction, respectively. The components of viscous stress tensor τ_{ij} in Equations (2-2) and (2-3) are defined as:

$$\tau_{ij} = \mu\left(\frac{\partial u_i}{\partial x_j} + \frac{\partial u_j}{\partial x_i}\right) - \frac{2}{3}\mu \frac{\partial u_k}{\partial x_k}\delta_{ij} \tag{2-4}$$

with Kronecker-Delta δ_{ij}. Due to the negligible hydraulic pressure drop in comparison with the system pressure of 25 MPa, it can be assumed that the thermo-hydraulic properties (ρ, c_p, μ, λ) are functions of temperature rather than functions of pressure. Fourier's law for molecular heat flux has been implemented in the energy equation.

Equations (2-2), (2-3) and (2-4) describe the general flow phenomenon. For the turbulence flow at a relative high Reynolds number, an appropriate approach for the approximate treatment of turbulent flows is time averaging, also called Reynolds Averaging. The methodology is based on the decomposition of the flow variables into a mean and a fluctuating part. The governing equations are then solved for the mean values, which are the most interesting issues for engineering applications. Thus, a velocity u_i can be divided into a time-averaged component, $\bar{u}_i$, and a turbulent fluctuating component, u_i':

$$u_i = \overline{u}_i + u_i' \tag{2-5}$$

where the mean value is denoted by an overbar and the turbulent fluctuations by a prime. The mean values are obtained by an averaging procedure:

$$\overline{u}_i = \lim_{\Delta t \to \infty} \frac{1}{\Delta t} \int_t^{t+\Delta t} u_i(x,\tau)\, d\tau \tag{2-6}$$

As a consequence, the mean value $\overline{u}_i$ does not vary in time, but only in space. In practice, $\Delta t \to \infty$ means that the time interval Δt should be as large as the typical time-scale of the turbulent fluctuations.

For variable-property turbulent flow with large density variations, as is the case for flows of supercritical fluids, it is necessary to employ another averaging approach, the Favre averaging (or mass weighted). It is defined as follows:

$$\tilde{u}_i = \frac{1}{\bar{\rho}} \lim_{\Delta t \to \infty} \frac{1}{\Delta t} \int_t^{t+\Delta t} \rho(x,\tau) u_i(x,\tau)\, d\tau \tag{2-7}$$

When the Favre averaging is used, it is customary to decompose the instantaneous velocity into the mass-averaged part, $\tilde{u}_i$, and a turbulent fluctuating part, u_i'', therefore

$$u_i = \tilde{u}_i + u_i'' \tag{2-8}$$

If Reynolds averaging Equation (2-6) and Favre averaging Equation (2-7) are applied towards other properties in the incompressible Novier-Stokes Equations (2-1), (2-2) and (2-3), the following relations for the mass and momentum conservation can be obtained:

Continuity of mass:

$$\frac{\partial \bar{\rho}}{\partial t} + \frac{\partial}{\partial x_i}(\bar{\rho}\tilde{u}_i) = 0 \tag{2-9}$$

Momentum equations:

$$\frac{\partial \bar{\rho}\tilde{u}_i}{\partial t} + \frac{\partial}{\partial x_j}\left(\bar{\rho}\tilde{u}_j\tilde{u}_i\right) = -\frac{\partial \overline{p}}{\partial x_i} + \frac{\partial}{\partial x_j}\left(\overline{\tau}_{ij} - \bar{\rho}\widetilde{u_i''u_j''}\right) + \bar{\rho}g \tag{2-10}$$

Energy equations:

$$\frac{\partial \bar{\rho} c_p \overline{T}}{\partial t} + \frac{\partial}{\partial x_j}\left(\bar{\rho} c_p \tilde{u}_j \overline{T}\right) = \frac{\partial}{\partial x_j}\left(\lambda \frac{\partial \overline{T}}{\partial x_j} - \bar{\rho} c_p \widetilde{u_j'' T''}\right) \tag{2-11}$$

These equations are the Reynolds-Averaged Navier-Stokes Equations (RANS) for variable-property flows, which are formally identical to the general equations with the exception of the additional terms and the neglected term of viscous energy dissipation in energy equation (2-11). Additionally, the momentum equation (2-10) contains the term $-\bar{\rho}\widetilde{u_i''u_j''}$, which is commonly called the Reynolds Stress tensor:

$$-\bar{\rho}\widetilde{u_i''u_j''} = \tau_{ij}^{Re} \tag{2-12}$$

The Reynolds Stress tensor represents the transfer of momentum due to turbulent fluctuations. In order to solve the τ_{ij}^{Re}, either we use additional Reynolds stress equations (see chapter 2.1.3) to close the system; or we use the Boussinesq hypothesis to model it. The Boussinesq hypothesis assumes that the turbulent shear stress is related linearly to mean rate of strain, as in a laminar flow (see Equation (2-4)). The proportionality factor is the eddy viscosity. Hence, the Reynolds Stress tensor can be modeled as:

$$\tau_{ij}^{Re} = \mu_t\left(\frac{\partial\overline{u}_i}{\partial x_j}+\frac{\partial\overline{u}_j}{\partial x_i}\right)-\frac{2}{3}\rho k\delta_{ij} \tag{2-13}$$

where k denotes the turbulent kinetic energy ($2k = \widetilde{u_i''u_j''}$), and μ_t stands for the eddy viscosity. Unlike the molecular viscosity μ, the eddy viscosity μ_t represents no physical characteristic of the fluid, but it is a function of the local flow conditions. The laminar viscous stress is evaluated by using Reynolds-averaged velocity components:

$$\overline{\tau}_{ij} = \mu\left(\frac{\partial\tilde{u}_i}{\partial x_j}+\frac{\partial\tilde{u}_j}{\partial x_i}\right) \tag{2-14}$$

The similar term as the Reynolds-stress tensor appears on the right side of energy equation (2-11) is so called turbulent heat flux, which can be modeled with the eddy viscosity:

$$q_j^{Re} = -\bar{\rho}c_p\widetilde{u_j''T''} = \frac{\mu_t c_p(\overline{T})}{Pr_t}\frac{\partial\overline{T}}{\partial x_j} \tag{2-15}$$

where Pr_t is the turbulent Prandtl number and its default value in CFX is 0.9. It is notable that a molecular heat capacity $c_p(\overline{T})$ appears in this expression rather than a modeled value $\overline{c}_p(T)$. This approach is used in almost all turbulence models and can be treated as a "standard" approach. In chapter 2.4, an improved approach by means of taking the turbulence fluctuation of heat capacity into account is introduced and results are validated by experiments.

2.1.2 Two Equation Models

In order to complete the closure of RANS equations, the key task of a turbulence model is to compute the eddy viscosity μ_t. The first model to describe the distribution of the eddy viscosity, thus the first proper turbulence model, was suggested by Prandtl in 1925 and is known as the Prandtl mixing-length hypothesis. In this hypothesis, the eddy viscosity μ_t is proportional to a local mean-velocity gradient and can be expressed as:

$$\mu_t = \rho l_{mix}^2 \left| \frac{d\overline{u}}{dy} \right| \tag{2-16}$$

where l_{mix} is the mixing length. This length scale characterizing the size of the large, energy-containing eddies is subject to transport process in a similar manner to the turbulence kinetic energy. Another process influencing the length scale is the eddy dissipation, which destroys the small eddies and thus effectively increases the eddy size.

The *k-ε* model

One of the most popular approaches to computer the eddy viscosity is to choose the turbulence kinetic energy $\boldsymbol{k}$ ($2k = \widetilde{u_i'' u_j''}$) as one of the turbulence parameters and the dissipation per unit mass $\boldsymbol{\varepsilon}$ as the second parameter which is defined by the following correlation:

$$\boldsymbol{\varepsilon} = \nu \overline{\frac{\partial u_i'}{\partial x_k} \frac{\partial u_i'}{\partial x_k}} \tag{2-17}$$

In turbulent flows dissipation rate **ε** depends on how viscosity affects the local small-scale structure of turbulence. Based on these two essential parameters and variable-properties, in particular the density ρ which can lead to axial acceleration effect and lateral buoyancy effect in supercritical flows, the standard ***k-ε*** model is shown as follows:

Eddy Viscosity:

$$\mu_t = \bar{\rho} C_\mu \frac{\boldsymbol{k}^2}{\boldsymbol{\varepsilon}} \tag{2-18}$$

Turbulence Kinetic Energy:

$$\frac{\partial \bar{\rho} \boldsymbol{k}}{\partial t} + \frac{\partial}{\partial x_j}\left(\bar{\rho} \tilde{u}_j \boldsymbol{k}\right) = \frac{\partial}{\partial x_j}\left[\left(\bar{\mu} + \frac{\mu_t}{\sigma_k}\right)\frac{\partial \boldsymbol{k}}{\partial x_j}\right] + \mu_t \frac{\partial \tilde{u}_i}{\partial x_j}\left(\frac{\partial \tilde{u}_i}{\partial x_j} + \frac{\partial \tilde{u}_j}{\partial x_i}\right) - \bar{\rho}\boldsymbol{\varepsilon} \tag{2-19}$$

Dissipation Rate:

$$\frac{\partial \bar{\rho}\boldsymbol{\varepsilon}}{\partial t} + \frac{\partial}{\partial x_j}\left(\bar{\rho}\tilde{u}_j\boldsymbol{\varepsilon}\right) = \frac{\partial}{\partial x_j}\left[\left(\bar{\mu} + \frac{\mu_t}{\sigma_\varepsilon}\right)\frac{\partial \boldsymbol{\varepsilon}}{\partial x_j}\right] + C_{\epsilon 1}\frac{\boldsymbol{\varepsilon}}{\boldsymbol{k}}\mu_t\frac{\partial \tilde{u}_i}{\partial x_j}\left(\frac{\partial \tilde{u}_i}{\partial x_j} + \frac{\partial \tilde{u}_j}{\partial x_i}\right) - \bar{\rho}C_{\epsilon 2}\frac{\boldsymbol{\varepsilon}^2}{\boldsymbol{k}} \quad (2\text{-}20)$$

in which the values of the closure coefficients in the Launder-Sharma model [104] are listed below:

$C_{\epsilon 1}$	$C_{\epsilon 2}$	C_μ	σ_k	σ_ε
1.44	1.92	0.09	1.0	1.3

Table 2–1: Closure coefficients in the ***k-ε*** turbulence model

The ***k-ε*** turbulence model is one of the most widely employed two-equation eddy viscosity model. It becomes very frequently to be used in the simulations for supercritical water due to its good performance in the free-shear layer flows. However, damping functions has to be employed in order to avoid the inherent singular defects in the near wall region. Those damping functions can strongly affect the prediction for ***k*** and ***ε*** especially in supercritical flows where the most significant variation of properties occurs in the near wall region.

It should be mentioned that the value of c_μ = 0.09 was chosen on the basis of experiments in flows in which the production of *k* and dissipation of the turbulence energy were in approximate balance [105]. In supercritical flows, for example mixed convective heat transfer where the velocity difference across the flow is only a small fraction of the convection velocity due to the property variation and the buoyancy effect, the production may be significantly different from dissipation and c_μ = 0.09 is no more correct in this flow condition. Hence the standard ***k-ε*** model might be unsuitable for supercritical flows.

The *k-ω* model

Another approach to compute the turbulence eddy viscosity is to choose the dissipation per unit turbulence kinetic energy **ω** as the second parameter. It is also referred as "turbulence frequency", especially in CFX, since Saffman (1970) described it as "a frequency characteristic of the turbulence decay process under its self-interaction". The basic ***k-ω*** turbulence model, developed by Wilcox [106], is the model of choice in the laminar sublayer. Unlike the ***k-ε*** model, the ***k-ω*** model does not involve damping functions. It has been proved [107] [108] that the behavior of the ***k-ω*** model in both of the laminar region and the logarithmic region is superior to that of the ***k-ε*** model in compressible flows. The standard ***k-ω*** turbulence model is as follows:

Eddy Viscosity:

$$\mu_t = \bar{\rho}\frac{\boldsymbol{k}}{\boldsymbol{\omega}} \tag{2-21}$$

Turbulence Kinetic Energy:

$$\frac{\partial \bar{\rho}\boldsymbol{k}}{\partial t} + \frac{\partial}{\partial x_j}\left(\bar{\rho}\tilde{u}_j\boldsymbol{k}\right) = \frac{\partial}{\partial x_j}\left[\left(\bar{\mu} + \frac{\mu_t}{\sigma_k}\right)\frac{\partial \boldsymbol{k}}{\partial x_j}\right] + \mu_t\frac{\partial \tilde{u}_i}{\partial x_j}\left(\frac{\partial \tilde{u}_i}{\partial x_j} + \frac{\partial \tilde{u}_j}{\partial x_i}\right) - \beta^*\bar{\rho}\boldsymbol{k}\boldsymbol{\omega} \tag{2-22}$$

Specific Dissipation Rate:

$$\frac{\partial \bar{\rho}\boldsymbol{\omega}}{\partial t} + \frac{\partial}{\partial x_j}\left(\bar{\rho}\tilde{u}_j\boldsymbol{\omega}\right) = \frac{\partial}{\partial x_j}\left[\left(\bar{\mu} + \frac{\mu_t}{\sigma_\omega}\right)\frac{\partial \boldsymbol{\omega}}{\partial x_j}\right] + \alpha\frac{\boldsymbol{\omega}}{\boldsymbol{k}}\mu_t\frac{\partial \tilde{u}_i}{\partial x_j}\left(\frac{\partial \tilde{u}_i}{\partial x_j} + \frac{\partial \tilde{u}_j}{\partial x_i}\right) - \beta\bar{\rho}\boldsymbol{\omega}^2 \tag{2-23}$$

in which the values of the closure coefficients used in CFX 12.0 are listed below:

α	β^*	β	σ_k	σ_ω
5/9	0.09	0.075	2.0	2.0

Table 2–2: Closure coefficients in the ***k-ω*** turbulence model

One of the most notable advantages of the ***k-ω*** model is the near wall treatment. In the boundary layer the ***k-ω*** model has an outstanding performance which has been proved in this work, (see further below).

The SST *k-ω* turbulence model

In this work, the Shear Stress Transport (SST) ***k-ω*** turbulence model developed by Menter [84] has been recommended, which merges the ***k-ω*** model with a high Reynolds number ***k-ε*** model (transformed into the ***k-ω*** formulation). All transport equations and constants, as well as the blending functions, are given in the Appendix A1.

The SST model seeks to combine the positive features of both models. Therefore, the ***k-ω*** approach is employed in the sublayer of the boundary layer and the standard ***k-ε*** model will be activated in the outer wake region or in free shear layers. Because the ***k-ω*** model needs no damping function, this leads, for similar accuracy, to a significantly higher numerical stability in comparison with the ***k-ε*** model especially for supercritical flows in the near wall layer. Furthermore, the ***k-ω*** model is also utilized in logarithmic part of the boundary layer, where it is superior to the ***k-ε*** model in variable properties flows. On the other hand, the ***k-ε*** model is employed in the outer portion of the boundary layer because the ***k-ω*** model is

strongly sensitive to the freestream value of $\boldsymbol{\omega}$ [109], and properties variation in this region is less important for supercritical flows.

Besides the combination of two models, one distinct feature of the SST turbulence model is the modified eddy-viscosity function, which is shown as below:

$$\mu_t = \frac{\rho \alpha_1 \boldsymbol{k}}{\max(\alpha_1 \boldsymbol{\omega};\ \Omega F_2)} \tag{2-24}$$

where F_2 is a function that is one for boundary-layer flows and zero for free shear layers and the Ω ($\Omega = \partial u_i / \partial x_j$) is taken to be the absolute value of the vorticity for general flows. The modification accounts for the transport of the turbulence shear stress in order to improve the accuracy of prediction of flows with a strong non-equilibrium between the production of k and its dissipation. This non-equilibrium can be caused by the adverse pressure gradient and also by the dramatic variation of properties and the buoyancy effect in the laminar sublayer in channel flows under a supercritical pressure.

Furthermore, the SST model has shown [84] its better performance than the ***k-ε*** model in the backward-facing step flow which is similar to the flow condition when the wire spacer is introduced into the flow domain.

In general, the SST ***k-ω*** turbulence model retains the robust and accurate formulation of the Wilcox ***k-ω*** model in the near wall region and takes advantage of the freestream independence of the ***k-ε*** model in the outer part of the boundary layer. It has proven to be very stable even in complex applications. Additionally, the SST ***k-ω*** turbulence model consumes only insignificantly more computing time compared with standard ***k-ω*** model. Hence, although the freestream effect is no need for concern with regard to the pipe flow, the SST ***k-ω*** turbulence model has been chosen to be the standard turbulence model in this work.

The Renormalization Group (RNG) *k-ε* Turbulence Model

Another two-equation turbulence model utilized in this thesis is the RNG ***k-ε*** model which is developed by Yakhot et al. [85] and has been also recommended by some other researchers [83] [86]. In the RNG ***k-ε*** model, the eddy viscosity, turbulent kinetic energy and dissipation rate are still given by Equations (2-17) and (2-18). However, the model uses a modified coefficient, $C_{\epsilon 1RNG}$, which attempts to account for the different scales of motion through changes to the production term. It is defined by

$$C_{\epsilon 1RNG} = C_{\epsilon 1} - \frac{C_\mu \eta^3 (1 - \eta/\eta_0)}{1 + \beta \eta^3}, \qquad \eta = \frac{\boldsymbol{k}}{\boldsymbol{\varepsilon}} \sqrt{2 S_{ij} S_{ij}} \tag{2-25}$$

$C_{\epsilon 1}$	$C_{\epsilon 2}$	C_{μ}	σ_k	σ_{ε}	η_0	β
1.42	1.68	0.0845	0.7194	0.7194	4.38	0.012

Table 2–3: Closure coefficients in the RNG turbulence model

The RNG ***k-ε*** model still needs damping functions in the near wall region in order to avoid the singular point in the dissipation equation, which results in a stiff performance in the laminar sublayer. Furthermore, since the model yields a log layer with a von Ќarmán constant κ of 0.4, it is assumed that flow is in local equilibrium, meaning the production of *k* and its dissipation are nearly equal. This assumption may not be valid if the fluid properties vary strongly in the near wall region. In chapter 3, the near wall analyses proved that damping functions and the equilibrium assumption result in an ill-prediction of all thermal hydraulic properties.

2.1.3 Reynolds Stress Turbulence Models

In the previous chapter, the Boussinesq eddy-viscosity approximation (2-13) assumes that the Reynolds-stress tensor, τ_{ij}, is related linearly to mean rate of strain tensor, S_{ij}, at all points in a turbulent flow. The coefficient of proportionality between τ_{ij} and S_{ij} is the eddy viscosity ν_T, which actually depends upon many details of the flow under consideration, such as the shape of the flow channels and flow-history effects. Although the two-equation model based on the Boussinesq hypothesis can provide good predictions for many flows of engineering interest, there are some applications for which predicted flow properties differ greatly from corresponding measurements.

Reynolds stress models (RSM) are based on transport equations for all components of the Reynolds stress tensor and the dissipation rate. These models do not use the eddy viscosity hypothesis, but solve an equation for the transport of Reynolds stresses in the fluid. For HPLWR, wire spacers induce strong swirl effect on the coolant flow in the core. Considering the advantages of the RSMs with regards to highly swirling flows, the SSG model and ω-based RSM (ωRSM) are introduced in this study and used later in the simulations which have a non-circular flow channel. The two models relate to each other in a similar way as the standard k-ε model and standard k-ω model. The transport equations of Reynolds stresses and the turbulence dissipation for the SSG model and the ω-based RSM are shown in Appendix A2 with the auxiliary relations and the closure coefficients.

2.2 Integration Domain and Boundary conditions

In HPLWR the design of a three-pass core shown in Figure 1–2 and wire spacers shown in Figure 1–3 raise several challenging issues with regard to the heat transfer behaviour of the water under a supercritical pressure. First, the heat transfer behaviour of water flowing in the square fuel assemblies differs from the flow in a circular tube. It means the available empirical correlations cannot accurately predict the heat transfer anymore due to the non-circular flow channels. Hence, the numerical study should take this geometrical effect into consideration. Second, Heat transfer deterioration is a special and important issue in this study which needs to be solved for the safety concern. The mechanisms of the onset of HTD have not been fully understood, and none of the empirical correlations can predict it. Therefore, the second task is to examine the performances of different turbulence models with respect to predicting the onset of the HTD with a rather simple geometry. Third, the wire spacers lead to a good mixing and a low pressure drop in the fuel assembly. The heat transfer behaviour is affected significantly by the wire and differs from that in tubes. The effect coming from wire spacers needs to be quantified. More importantly, the local hotspot needs to be investigated as well.

Based on all the reasons mentioned above, the geometries of circular tubes and annular channels have been chosen as the basic geometry in order to gain more knowledge about the heat transfer behaviour of the supercritical water upward flow. In particular, the mechanisms of the HTD also have to be understood for the purpose of the safety analysis. The geometries of a fuel rod with and without wrapped wire inside a square channel have been chosen as the simplified geometries to investigate the mixing effect of wire and the hotspot on the rod surface. These three basic geometries are shown in Figure 2–1.

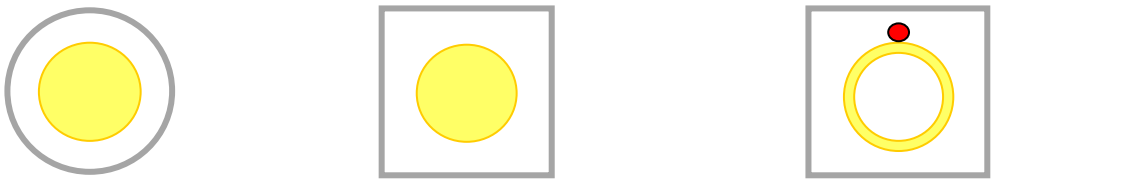

• Annular Channel • Bare rod in a Square Channel • Wire-wrapped Rod in a Square Channel

Figure 2–1: Top view of the three basic flow channels in this study

2.2.1 Annular Channel

Many experiments to observe the flow characteristics at the supercritical pressure have been conducted for water ($P_{critical}$= 22.1 MPa, $T_{critical}$ = 647 K) and CO_2 ($P_{critical}$ = 7.38 MPa, $T_{critical}$ = 304 K) which has been studied widely as a substitute of water due to the similar

heat transfer characteristics at the supercritical pressure. These studies are comprehensively summarized by Pioro and Duffey [110]. However, most of the studies are carried out in terms of water or CO_2 flowing in the circular pipes rather than in the annular channels which are thermodynamically more similar to the actual condition of annular geometry with wire wraps in the next stage of investigation study. The objective of the work in this chapter is to evaluate the performance of the SST k-ω turbulence model in terms of predicting the heat transfer behaviour of the supercritical fluids upward flow in an annular channel. Additionally, the ability of capturing the onset of the HTD is also an important criterion to judge whether the model is appropriate to be used under the supercritical conditions.

In this section the computational test cases regarding to the annular channels are described. The basic geometry for the numerical simulation is an annular vertical channel, in which the fluid flows around a heated rod at the pressure of 8.12 MPa for carbon dioxide (CO_2) and 25 MPa for water. The flow is treated to be two dimensional and axisymmetric.

Calculation Parameters

The experiments in supercritical CO_2 (see Bae et al., [71]) were carried out in a vertical annular channel with a rod diameter of 8 mm and a tube diameter of 10 mm. The experiments were performed at a supercritical pressure of 8.12 MPa, which is slightly higher than the critical pressure of CO_2 (7.38 MPa). The pseudocritical temperature T_{pc} is 308 K at the pressure of 8.12 MPa. The test matrix covering the selected cases is listed in

Pressure, (*P*)	Mass flux density, (*G*)	Heat flux, (*q*)
MPa	*kg/m²s*	*kW/m²*
8.12	400, 1200	30, 50

Table 2 – 4: Test matrix for supercritical CO_2 flowing in an annular channel

The experimental tests in supercritical water were carried out by Glushchenko et al. [60] in an inner-heated, vertical annular channel. The width of the annular gap is kept constant at the value of 1 mm. The test matrix covering the selected cases is listed in Table 2-5. The ranges of variation of the working parameters are as follows: pressure kept at a constant value of 23.5 MPa, specific wall heat flux of up to 2.96 MW/m^2, mass flux density was 2200 kg/m^{2}s. The pseudocritical temperature T_{pc} is 652.5 K at pressure of 23.5 MPa.

Pressure, (*P*)	Mass flux density, (*G*)	Heat flux, (*q*)
MPa	*kg/m²s*	*MW/m²*
23.5	2200	1.15, 2.41, 2.96

Table 2 – 5: Test matrix for supercritical water flowing in annular channel

Mesh Structures and Boundary Conditions

A schematic diagram of the flow domain is shown in Figure 2–2. The computational domain can be considered as two-dimensional and axi-symmetric (a 5° wedge sector of an annular channel with only one layer of cells along the angular direction). The model describes a single phase, steady state, almost isobaric, turbulent flow. As illustrated in the Figure, the width of the annular channel is 1 mm with a length of 1500 mm in CO_2 cases and 700 mm in water cases, respectively. The heat flux (q) is imposed on the inner side of the computational domain and adiabatic boundary condition is used to the outer wall. The bottom position of the inlet boundary indicates that the fluid flows upward in the channel. To obtain a fully-developed flow field at the inlet of the heated region, an additional hydraulic calculation is performed previously to provide a fully-developed flow condition. The inlet temperature of the simulation is selected to get a similar range of the bulk enthalpy corresponding to the range in the experiment. Outlet boundary condition with constant pressure is chosen at the outlet of flow domain.

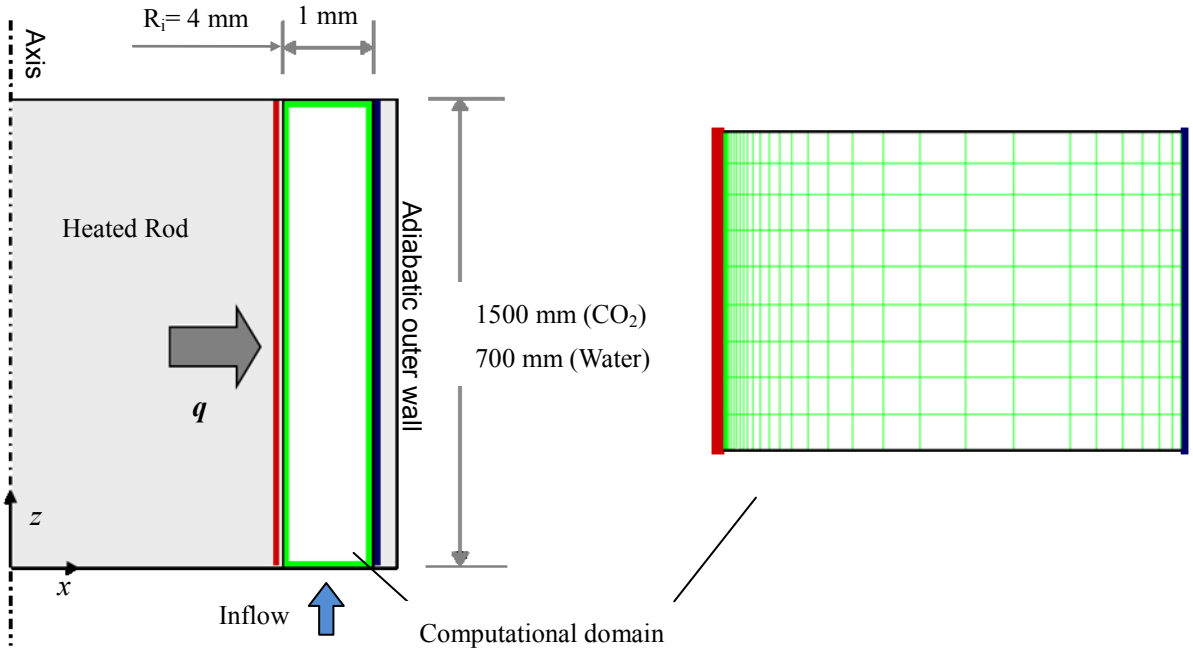

Figure 2–2: Schematic diagram of the flow domain and the mesh of an annular channel

In order to fully resolve the laminar sublayer instead of using standard wall functions, the mesh is uniformly distributed along the flow direction and strongly compressed towards the heated side by the use of the Bi-exponential mesh law. The nodes distribution along with the radial direction is shown in Figure 2–3. The sensitivity studies towards y_1^+ and the number of the nodes are carried out in order to verify the model. Depending on the results of sensitivity study, a proper mesh structure will be used in the following numerical simulations to predict the selected test cases of water and CO_2.

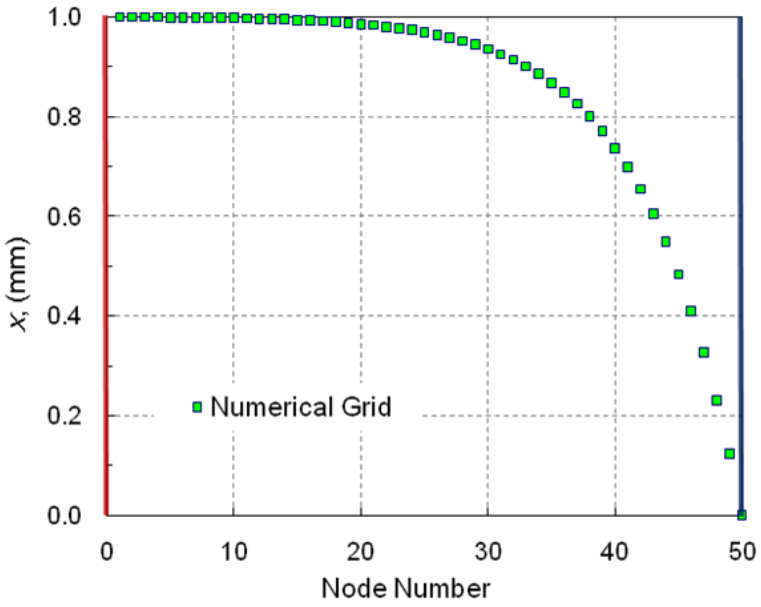

Figure 2–3 : Numerical grid distribution along the radial direction (50 nodes)

If the increase of the bulk enthalpy throughout the whole computational domain is smaller than the value in the experiment, which occurs very likely in the case at a low heat flux, stepwise calculations are necessary so that the simulation results can be compared with experimental data within the entire range of the measured bulk enthalpy.

The mesh structures and boundary conditions for the tube are quite similar as those for the annular channel. The differences are the boundary conditions corresponding to the inner and outer walls. The “symmetry” boundary condition is given to the inner wall, and a specific heat flux is given to the outer wall.

2.2.2 Bare Rod in a Square Channel

Many studies for the heat transfer behaviour in supercritical water have been performed for vertical circular tubes or annular channels. Some criteria for onset of the HTD have been developed for circular geometries as well. However, the development of the turbulent and convective heat transfer parameters due to the radial properties variation, acceleration and buoyancy can be strongly depending on the shape of the flow ducts. For example, when the heat transfer correlation developed for circular tubes is used to predict the heat transfer behaviour of the water flowing in a square annular channel, it may cause a considerable deviation away from the measured value. Furthermore, the local hotspot which needs a special concern in the sub-channel flows does not exist under a circular tube condition.

The CFD studies for supercritical water are mostly concentrated to circular tubes. The turbulence models used in these studies are mainly limited to the two-equation models, which assume an isotropic behaviour of the turbulence. However, in the flow channels other

than a circular tube, e.g. sub-channels of a fuel assembly, anisotropic behaviour of turbulence and secondary flow are observed due to the interaction among the anisotropic Reynolds stresses. Turbulence models, which are capable of predicting these anisotropic Reynolds tresses, are therefore required for the analysis of heat transfer in non-circular flow channels. The main objective of the research on the square annular channel is to study the channel shape effect on the heat transfer behaviour in the supercritical water.

Calculation Parameters

The experimental investigation of the heat transfer behaviour of supercritical water flowing upward in a square annular channel is performed by Licht et al. [65]. The square annular test section geometry is a 10.7 mm diameter heated rod within a 28.8 mm wide flow channel. The total heated length is 1010 mm with a rod cladding thickness of 0.4 mm. The ranges of the working conditions are listed in Table 2 – 6. In this table, pressure is kept at a constant value of 25 MPa; specific wall heat flux is of up to 440 kW/m^2; mass flux density varies from 315 kg/m^{2}s to 1000 kg/m^{2}s. The pseudocritical temperature (T_{pc}) is 658 K at pressure of 25 MPa.

Pressure, (*P*)	Mass flux density, (*G*)	Heat flux, (*q*)
MPa	*kg/m²s*	*kW/m²*
25	315, 1000	220, 440

Table 2 – 6: Test matrix for supercritical water flowing in a square annular channel

Mesh Structures and Boundary Conditions

A cross-sectional schematic diagram of a 3D computational domain is shown in Figure 2 – 4. The geometry used for the model is a 1/8 section with a length of 1.1 m. The inlet and outlet boundary conditions are mass flux density and outflow, respectively. Non-wall edges are designed as symmetry boundaries. As illustrated in the figure, the cladding material has been already taken into account. The mesh in the flow domain is compressed towards heated rod in order to fully resolve the viscous sublayer ($y_1^+ < 1$). The mesh in the solid domain is also gradually refined towards the liquid-solid interface to make a smooth mesh transition from the flow domain to the solid domain. In order to give a fully-developed flow as initial boundary condition at the inlet, a hydraulic simulation, which is calculated isothermally with translational periodicity boundary conditions designed at both inlet and outlet, has been previously performed.

For the geometry of square annular channel, the ωRSM is used in the 3D simulations. The two-equation models are not able to capture the secondary motions in non-circular straight channels due to the inherent shortcoming in anisotropic turbulence (see [98], [111]). In addition, buoyancy effect has been taken into consideration in the simulations.

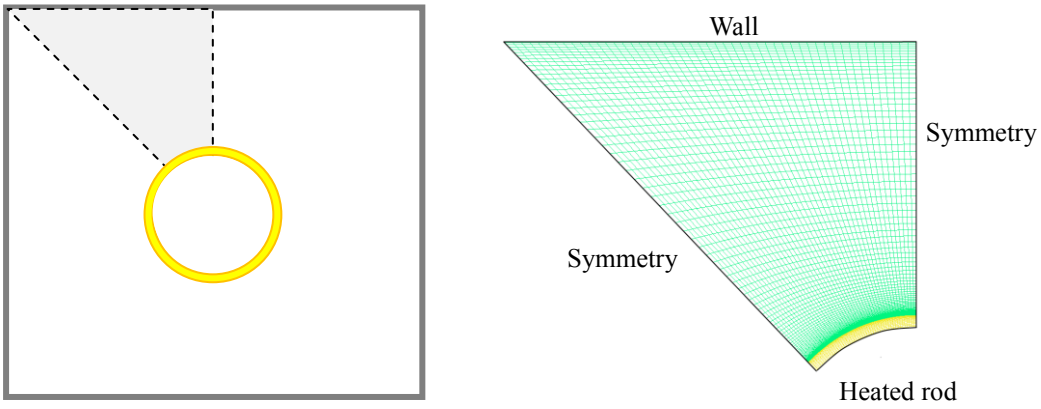

Figure 2 – 4: Cross-sectional view of the geometry (a) and meshing scheme (b)

2.2.3 Wire-Wrapped Rod (WWR) in a Square Channel

Numerical analysis of wire-wrapped fuel pins for HPLWR is challenging for several reasons. The presence of the wire inside the fuel assembly results in a strong flow mixing and sweeping among sub-channels. It is therefore very difficult to accurately and quantitatively predict the thermal hydraulic behaviour by current turbulence models especially for supercritical water. Furthermore, the wire induces extra difficulties to the mesh generation. The point contact between the wire and the rod will result in a large number of cells in this region with very poor quality, which therefore has to be avoided and simplified in the model. Furthermore, in order to fully resolve the viscous sublayer on the surface of the heated rod, a refined mesh around the rod is necessary, which will considerably increase the number of cells. Hence, a proper structured mesh with a reasonable number of cells is very important for this investigation.

Calculation Parameters

The experimental investigation of the heat transfer behaviour for a heated wire-wrapped rod inside a square vertical channel is performed by Li et al.[66]. As illustrated in Figure 2–5, the square annular test geometry is a Ø10mm × 2.5mm ($D_{rod} \times \delta$) stainless steel circular pipe within a 15 mm wide flow channel. The wire wrapping helically around the rod is made of ceramic material with a diameter of 2.5 mm (D_{wire}). As to be noticed obviously, a geometric simplification is implemented in the junction region between the wire and the rod. The purpose is to avoid low quality cells which have too small angles due to the point contact. For the same reason the wire diameter has to be slightly smaller than the original value of 2.5 mm. One pitch of the wrapped wire is 200 mm which is consistent with the design of HPLWR. Experimental conditions used in simulations are listed in Table 2 – 7, which included pressure of 25 MPa, mass flux density of 800 kg/m^{2}s and heat flux of 400-650 kW/m^2.

Pressure, (P)	Mass flux density, (G)	Heat flux, (q)
MPa	*kg/m²s*	*kW/m²*
25	800	400, 650

Table 2 – 7: Test matrix for a wire-wrapped rod in a square annular channel

Mesh Structures and Boundary Conditions

The mesh strategy is one of the most important issues associated with the wrapped-wire geometry. Figure 2–6 illustrates a structured mesh, which discretizes the flow and solid domain with hexahedral elements. The mesh is composed of two parts: a circular mesh in the core and a wall mesh. Both of them are stretched along the axis from an initial 2D surface mesh. The core mesh is then axially stretched and rotated with a certain angle in each layer. This angle is carefully calculated in order to ensure a one-to-one correspondence of the nodes between the core mesh and the wall mesh in their interfaces.

Based on this mesh strategy, a proper and acceptable number of the total mesh can be generated with a fine local resolution near the heated rod surface. The mesh in the flow domain is compressed towards heated rod in order to fully resolve the viscous sublayer ($y_1^+ < 1$), which is a prior condition to predict the cladding temperature precisely and furthermore to capture the onset of a possible DHT. The mesh in the solid domain is also gradually refined towards the liquid-solid interface to make a smooth mesh transition from the flow domain to the solid domain.

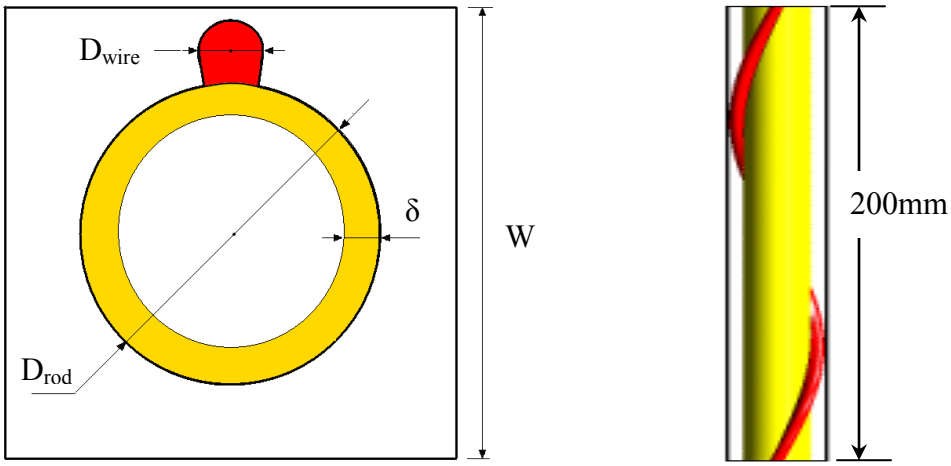

Figure 2–5: Schematic diagram of a wire-wrapped rod inside a square annular channel

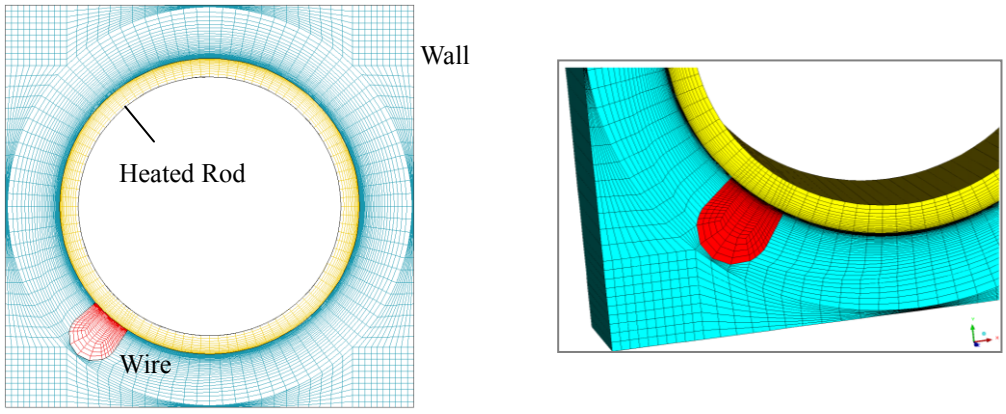

Figure 2–6: Mesh structure of a wire-wrapped rod within a square channel

As same as what have been done in the case of the square annular channel, a hydraulic simulation is performed before the thermal-hydraulic cases in order to provide a fully-developed flow for the inlet boundary condition. In thermal-hydraulic simulations, mass flux density and temperature is prescribed at the inlet. A relative pressure is given at the end of the channel to be an outlet boundary condition. Volumetric heat source is prescribed in the solid domain to simulate the direct heating approach by using the alternating current in the experimental test.

A channel with a length of 2000 mm (10 wire pitches) is used as a standard geometry to cover the enthalpy region as much as possible with an acceptable number of cells. However, stepwise calculation, which means the outlet information in a previous calculation will be used as the inlet boundary condition in the following calculation, is necessary here in order to develop the flow over a wider and a comparable range of enthalpy in comparison with the experimental data.

2.3 Verification and Validation

Because of the necessity to model many of the unsolved details of supercritical flows, it is necessary to assess the accuracy of the CFD method with the help of experimental data. The validation test is a method to minimize and quantify modeling errors and ensure that the CFD model being solved is a good representation of reality. Based on the validated model, further investigations, e.g. the derivations of form-factors in this study, can be carried out with a certain confidence.

According to the Best Practice Guidelines [112], sensitivity study is the first which has to be done before the validation. The objective of a sensitivity study is to examine the effect on the predictions of the variation of any particular parameter in the simulation. In the first

instance this technique can be used to examine the predicted flow over a range of certain flow parameters and boundary conditions whose exact value may not be defined correctly, such as the node number along the radial direction or the distance of the first node away from wall (y_1^+). In addition such sensitivity analyses can be carried out to examine the effect of various model parameters, empirical constants, physical properties, code default options, discretization schemes, grid types and mesh size.

The sensitivity study is a highly time-consuming process due to a strong mesh refinement (factor is 4 in this study). That means even for simple cases the study has to be limited in a certain scope. In this chapter, the sensitivity analyses have been performed only to some key issues: node number along the radial direction, distance of the first node away from wall (y_1^+), grid types, turbulence models and buoyancy conditions.

2.3.1 Mesh Sensitivity Study for Annular Channels

Mesh sensitivity study is used to quantify the discrepancy induced by the mesh size. In this study, the SST k-ω turbulence model is chosen as the standard turbulence model due to its pre-exhibited capability in supercritical fluids. In order to fully resolve the boundary layer, the non-dimensional distance of the first computational node away from the wall (y_1^+) has to be given properly. Another essential issue for a good performance of the model is the number of computational nodes in the boundary layer. Because the same mesh law is used for each of cases, the more nodes in the total length of gap result in the more nodes in the boundary layer. Hence, sensitivity studies of y_1^+ and the node number along radius are carried out. One set of experimental data for supercritical water [60] and one for supercritical CO_2 [71], which both belong to the mode of DHT, have been selected to compare with the calculated results in this mesh sensitivity study. Working conditions are described in Table 2 – 4 and Table 2 – 5, respectively.

The results of sensitivity studies for supercritical water are shown in Figure 2–7. In the left chart three different values of y_1^+ are used in simulations with an identical node number of 200 along the radius. It can be found that the calculated result shows a considerable deviation from the experimental data and did not capture the onset of the HTD when the value of y_1^+ is bigger than 1 (green curve). Once the condition of y_1^+ less than 1 is fulfilled, the agreement between calculated value and measured value is improved. In particular, the onset of the HTD has been captured by the model. The difference between the finest mesh (y_1^+=0.1, blue curve) and the middle mesh (y_1^+=0.7, orange curve) is negligible. In the right chart three different values of node number along radius are used in simulations with an identical y_1^+ value of 0.1. The coarse mesh has a node number of 50 and the refine-factor is 4 for middle mesh (200) and fine mesh (800). As is shown in the chart, the results become independent of the node number when it is more than 200.

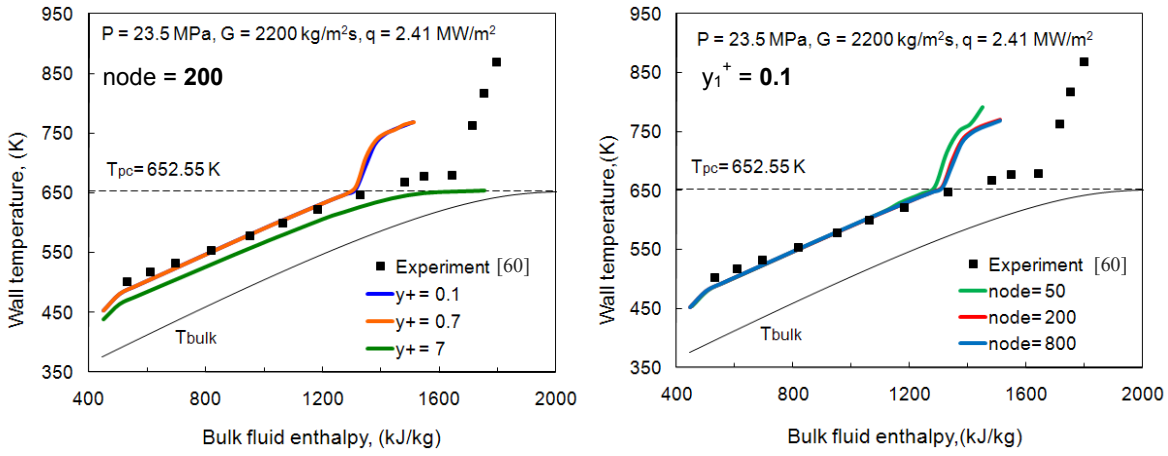

Figure 2–7: Sensitivity studies of y_1^+ (left) and node number along radius (right) for **Water**

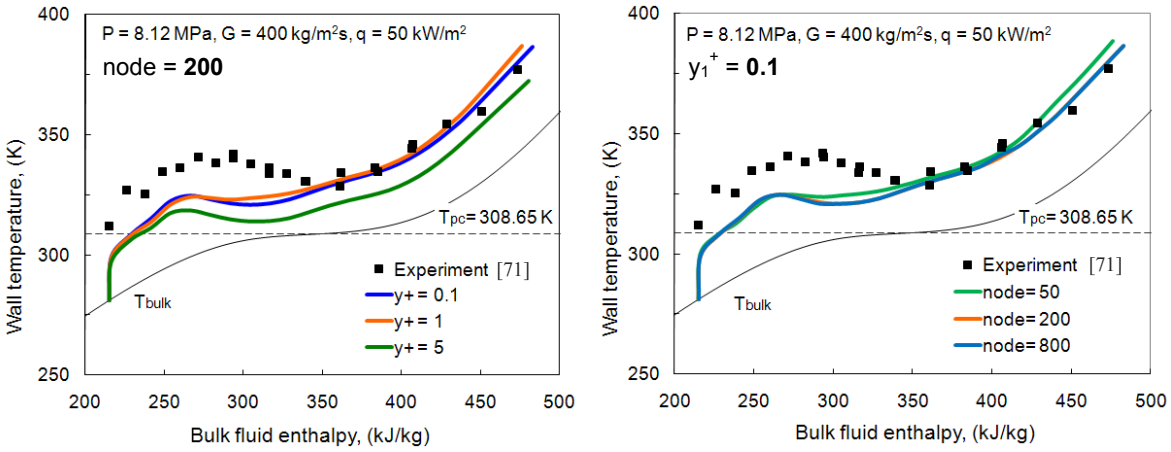

Figure 2–8: Sensitivity studies of y_1^+ (left) and node number along radius (right) for **CO_2**

Figure 2–8 illustrates the results of the sensitivity studies for supercritical CO_2 flowing upward in an annular channel. In the left chart three different values of y_1^+ (0.1, 1, 5) are used in simulations with an identical node number of 200 along the radius. All three curves show the local peak of wall temperature in the lower enthalpy region. However, the green curve (y_1^+=5) has an obvious disagreement with experimental data in the whole enthalpy region. Disagreement also exists in comparison with both of the blue curve (y_1^+=0.1) and the orange curve (y_1^+=1), nevertheless, they show a good agreement with experimental data in the higher enthalpy region. Furthermore, the blue curve (y_1^+=0.1) has qualitatively captured the decrease of the wall temperature after the local peak at enthalpy of 265 kJ/kg. The value of 0.1 is therefore used in the following cases. In the right chart three different values of node number along radius are used in simulations with an identical y_1^+ value of 0.1. Three meshes used here have the node number of 50, 200 and 800, respectively. As is

shown in the chart, results are almost identical with a slight difference before the pseudocritical enthalpy (i_{pc}).

To sum up all the information revealed by Figure 2–7 and Figure 2–8, it is clear that the y_1^+ value of 0.1 and the node number of 200 can be treated as a standard mesh configuration near the heated wall. Those two values will be used later in the 3D models for the square annular channel and the channel with a wire-wrapped rod inside.

2.3.2 Buoyancy Sensitivity Study for Annular Channels and Tubes

Once the correct model configurations are obtained, the influence of buoyancy on heat transfer could be studied. This study is performed by comparison of the solution obtained with and without the buoyancy terms in the governing equation (2-10). The expected influence of buoyancy can be examined by the ratio of Grashof number and Reynolds number. Jackson and Hall [113] developed a useful criterion (see Equation (2-26) derived from simple boundary layer theory. This criterion can be used as a simple prediction of the onset of HTD. For vertical tubes, the criterion for negligible buoyancy effects can be expressed as below:

$$\overline{Gr}/Re^{2.7} < 10^{-5} \tag{2-26}$$

Under the normal operating conditions of PWR, this ratio is small due to very high flow velocities. The criterion (2-26) is fulfilled. Therefore the buoyancy influence on heat transfer could be neglected for typical operating conditions of PWR.

However, in the HPLWR operating conditions, even though the flow velocity is relative high, a strong change of thermo-physical properties happens in the flow channel. Thus the ratio of Grashof number and Reynolds number cannot be kept constant and the criterion (2-26) may not be fulfilled anymore. It should be pointed out that the buoyancy is not the only reason causing the HTD. Its influence strongly depends on the flow conditions. Other effects, such as the streamwise acceleration and the change of the thermo-physical properties near the wall, could also cause the heat transfer to deteriorate.

Two different experiments are chosen for validation. One comes from Glushchenko [60] and another from Shitsman [44]. Both experiments measure the heat transfer in a highly deteriorated region. The experiment from Glushchenko is performed with a very high coolant mass flux density, where the buoyancy effect should be negligible on the heat transfer according to criterion (2-26). On the contrary, the experiment from Shitsman is in the region of strong buoyancy influence due to its relative low coolant mass flux density. The simulations are carried out by using SST k-ω turbulence model. The mesh used in the model is described in chapter 2.2.1 with the y_1^+ value of 0.1 and the node number of 200 along radius, which are coming from results of the mesh sensitivity study.

Buoyancy effect at high coolant mass flux density

A buoyancy sensitivity study for high coolant mass flux density has been performed. The calculated results are compared with the experimental data. In this case, the mass flux density of the coolant is 2200 kg/m^{2}s and the heat flux imposed to the rod is 2.41 MW/m^2. The gap width of the vertical annular channel is 1 mm. Supercritical water is under pressure of 23.5 MPa.

Numerical results and the comparison are shown in Figure 2–9 where the wall temperature is plotted against the bulk fluid enthalpy. It is very clear that the buoyancy has no effect on the heat transfer. There must be other mechanisms which cause the decrease in heat transfer. The decrease of viscosity and increase of specific heat capacity may lead to the heat transfer deterioration.

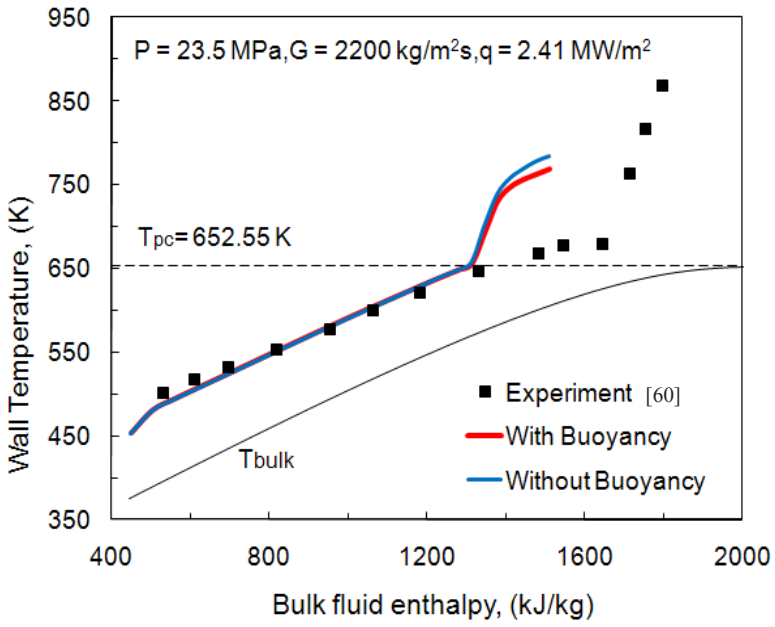

Figure 2–9: Buoyancy sensitivity study at a **high** coolant mass flux density

Buoyancy effect at low coolant mass flux density

Flow simulation at a low coolant mass flux density is demonstrated in the experiment by Shitsman. This experiment is performed with supercritical water at pressure of 23.3 MPa in a pipe with inner diameter of 8 mm. The pipe is uniformly heated with a heat flux of 319.87 kW/m^2 and a coolant mass flux density of 430 kg/m^{2}s. For these parameters, the criterion of negligible buoyancy effect is not fulfilled anymore, which indicates that the buoyancy may have a strong influence on the heat transfer.

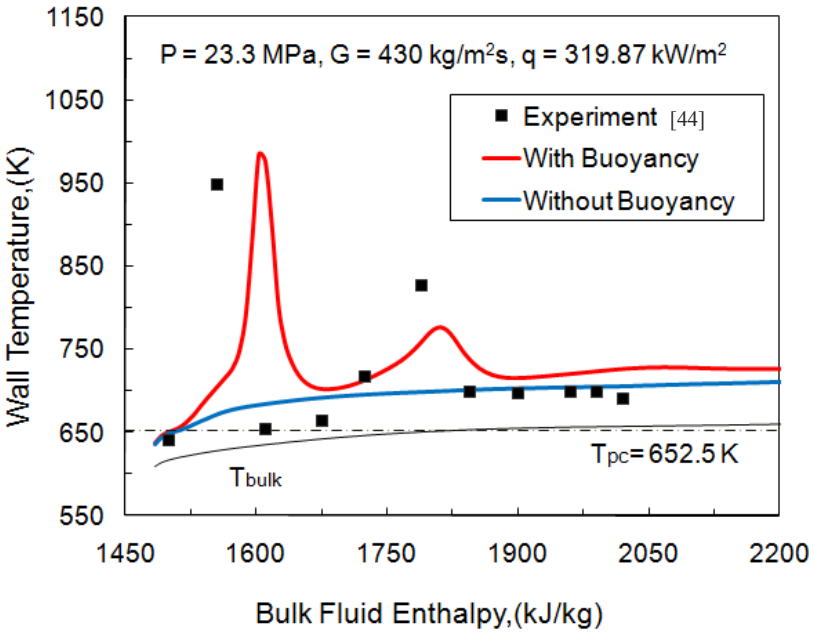

Figure 2–10: Buoyancy sensitivity study at a **low** coolant mass flux density

Comparison of the numerical results with the experimental data is shown in Figure 2–10. The calculated results with buoyancy term turning on reach a good agreement with experimental data. The model is capable to capture the whole deteriorated region which is represented by the two obvious peaks in the wall temperature.

The same model with an identical numerical grid without buoyancy term in the equations leads to a considerable under-prediction in the wall temperature. This means that the buoyancy term in the Navier-Stokes equations is responsible for the increase of the wall temperature, in other words, the heat transfer deterioration under such flow conditions is caused by buoyancy effect. A possible explanation of this phenomenon is that the buoyancy accelerates the flow close the wall, which then leads to a flat velocity profile, thus effectively reduces the shear stress in the region and consequently impairs the heat transfer. More analyses of the buoyancy effect are written in chapter 3.1.

Conclusions of Buoyancy Sensitivity Study for Annular Channels and Tubes

Buoyancy influence on the heat transfer deterioration was investigated for both of high and low coolant mass flux density. The results reveal that buoyancy is one of the important factors that dominate the heat transfer deterioration, mainly under the working conditions with low coolant mass flux density and relative high heat fluxes. For the high coolant mass flux density, buoyancy effect can be neglected.

Regarding on the computing time, there is no difference between the cases with and without buoyancy term in the Navier-Stokes equations. Hence, in all the simulations, a full buoyancy model is always used in the model configuration.

2.3.3 Turbulence Models Sensitivity Study for Annular Channels and Tubes

The last task of the sensitivity study for annular channels and tubes is to test the performances of two turbulence models. Selection of a turbulence model is one of the crucial factors for the successful estimation by CFD. It is well known that numerical simulations with different turbulence models show different results, when they are applied to simulate the flows with additional elements involved in, such as acceleration effect, buoyancy effect, curvature and so on. It is possible to expect that results obtained by various turbulence models are different, especially when the flow encounters strong change of properties at the supercritical pressure. In this section several simulations are carried out to evaluate the performance between the RNG k-ε turbulence model and the SST k-ω turbulence by comparing the simulations with the experimental data.

The mesh used for both models are exactly identical which is described in chapter 2.2.1 with the y_1^+ value of 0.1 and the node number of 200 along radius. Experiments used to compare with simulations are performed in four individual facilities by different researchers. The parameters of these four datasets are listed in Table 2–8, shown as below:

	Serial Number	Flow Direction	Pressure, *MPa*, (*P*)	Mass flux density, *kg/m²s*, (*G*)	Heat flux, *kW/m²*, (*q*)
Glushchenko et al. [60]	A2	upward	23.5	2200	2410
Ornatskii et al. [57]	B1	downward	25.5	1500	1320
	B2	downward			1630
	B3	upward			1810
Yamagata et al. [50]	C1	upward	24.52	1260	233
	C2				465
	C3				698
	C4				930
Shitsman et al. [44]	D1	upward	23.3	430	319.87

Table 2–8: Parameters of experiments in supercritical water for model sensitivity study

The case A2 is performed in a vertical annular channel. The others are performed in vertical tubes. In most of cases the heat transfer is deteriorated at a high mass flux density, which means the buoyancy effect can be neglected according to the conclusion drawn in the buoyancy sensitivity study. There are two cases, B1 and B2, in which the supercritical water is flowing downward in vertical tubes. The results of those two cases can be used to analyse the flow situation in the superheat I

Glushchenko (case A2)

The result of the turbulence model sensitivity study to vertical upward flow in an annular channel is shown in Figure 2–11, which shows the comparison of predictions and experiments of wall temperature at the case A2. Before the wall temperature pass through the pseudocritical point, the value predicted by the SST model (red curve) gives a good agreement with the measured value and shows an abrupt increase in wall temperature which just passes the pseudocritical value of 652.5 K. On the contrary, the RNG model (blue curve) seems like it is insensitive to pass through the pseudocritical point. It also over-predicts the wall temperature in the lower enthalpy region (500 kJ/kg – 1400 kJ/kg).

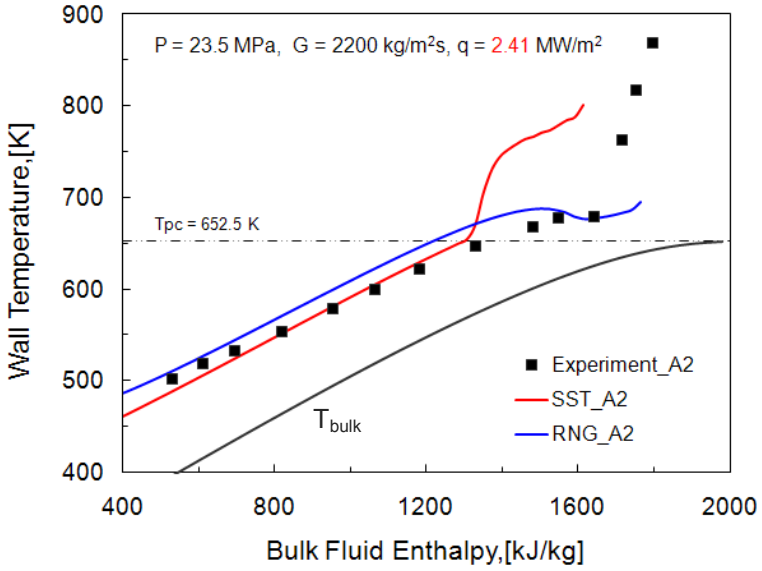

Figure 2–11: Model sensitivity study for annular channel (Glushchenko et al. [60])

Ornatskii (case B1, B2, B3)

Figure 2–12 compares the wall temperature between simulation and experiment at the cases of B1, B2 and B3. At a heat flux of 1320 kW/m^2 both the RNG model and the SST model show a good agreement with the measured wall temperature. However, the SST model captured the abrupt increase of the wall temperature when the pseudocritical temperature is lower than wall temperature and bigger than bulk temperature ($T_w > T_{pc} > T_b$). The RNG model is not capable of capturing the onset of HTD. It shows an enhanced heat transfer in the vicinity of T_{pc} and a tendency of deterioration in the high enthalpy region. The result at a heat flux of 1630 kW/m^2 is similar as the previous case B1. In the low enthalpy region ($i_b <$ 1400 kJ/kg) both of two models correctly predicted the wall temperature. In the high enthalpy region ($i_b >$ 1400 kJ/kg) the SST model captured the onset of deterioration with

certain deviation compared with measured value. The RNG model still failed to capture the onset of HTD in the vicinity of T_{pc} and gives the deterioration at a higher enthalpy of 1800 kJ/kg. It needs to be noted that at the cases of B1 and B2 supercritical water flows downward in the vertical tube, which is different with the case B3.

The last chart in Figure 2–12 shows the results at a heat flux of 1810 kW/m^2. Supercritical water flows upward in the vertical tube. It is clear that the SST model gives a very good agreement with experiment in wall temperature before the heat transfer becomes restored. More importantly, the onset of the HTD is captured by the SST model in the correct position where the wall temperature just over-strides T_{pc}. Furthermore, the following development of wall temperature predicted by the SST model is almost the same as the experiment until its local peak. The tendency of the restored heat transfer has been also predicted out. The RNG model gives an acceptable prediction before the onset of the HTD. However, it failed to predict the onset of the HTD in the correct position and shows no restored heat transfer in the whole enthalpy region measured in experiment.

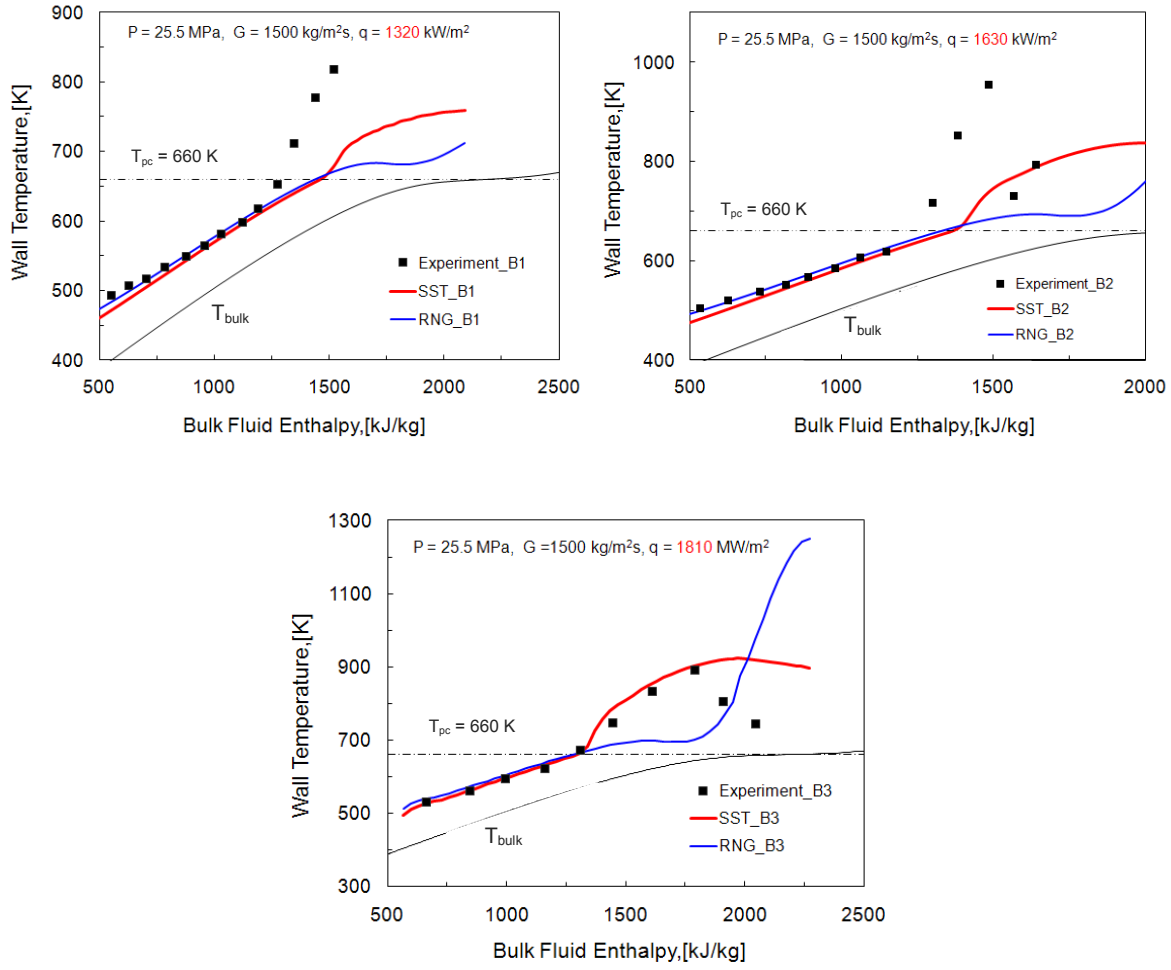

Figure 2–12: Model sensitivity study for tubes (Ornatskii et al. [57])

Yamagata (case C1, C2, C3, C4)

In Figure 2–13, the numerical results are compared with Yamagata et al.'s experimental data (1972). Those experimental data is one of the most popular data and widely used to validate other numerical results. At a heat flux of 233 kW/m^2, the SST model and the RNG model showed quite similar results which are acceptable in the whole enthalpy region measured in experiments. Both of them underpredicted the wall temperatures slightly in the low enthalpy region. At a heat flux of 465 kW/m^2 the SST and the RNG give a good agreement with experiment, except for a slight over-prediction of SST model in high enthalpy region and a slight under-prediction of the RNG model near the pseudocritical enthalpy of 2146 kJ/kg.

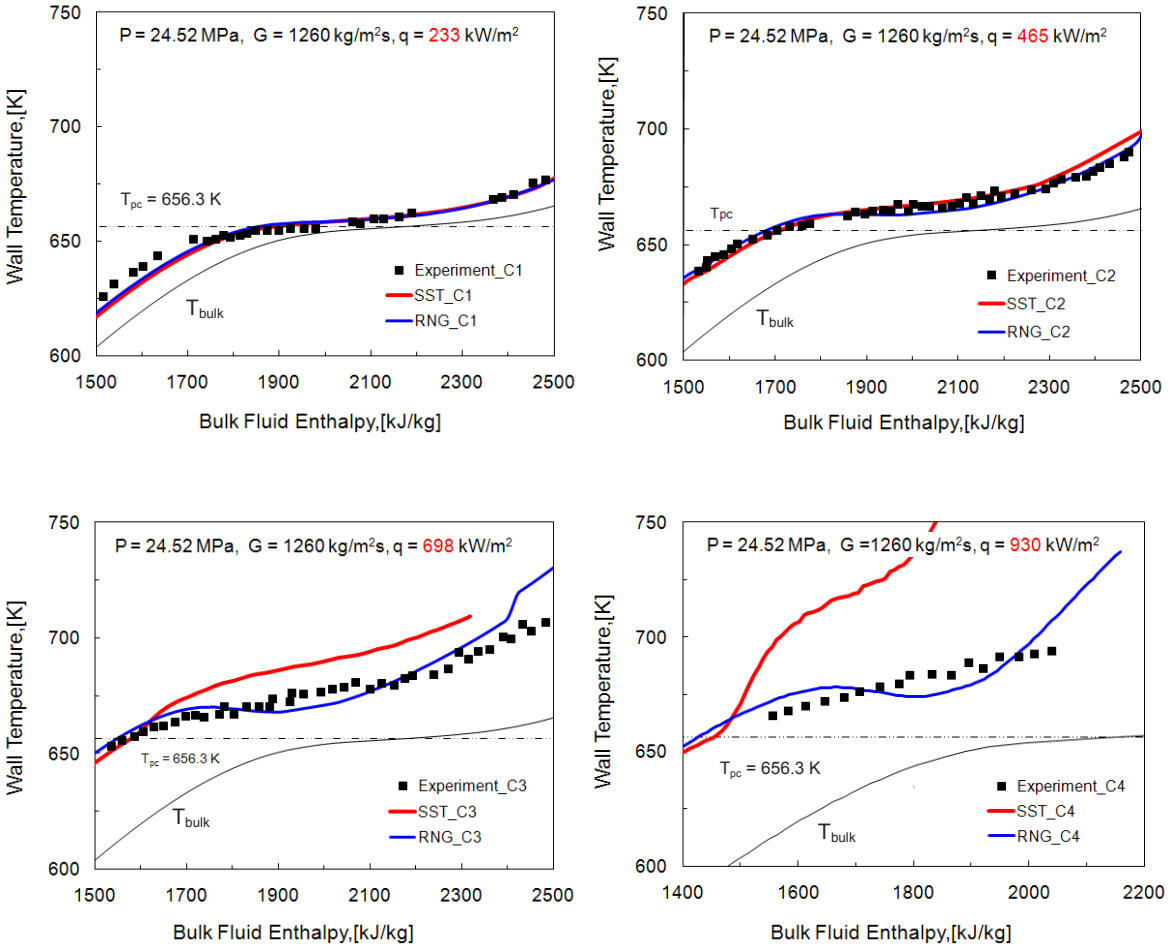

Figure 2–13: Model sensitivity study for tubes (Yamagata et al. [50])

At a heat flux of 698 kW/m^2 the deviation between the prediction by the SST model and the experiment becomes obvious when the all temperature passes beyond the pseudocritical temperature ($T_w > T_{pc}$). It is worth to be mentioned that the difference in wall temperature between the prediction and the experiment keeps constant after a mild impaired heat transfer predicted by the SST model. This correct tendency indicates that the SST model can

predict the flow in the high enthalpy region if the information near the inlet is given. In this case, the RNG model shows a better prediction than the SST model. However, the enhanced heat transfer near the enthalpy of 1900 kJ/kg, which also exists in the previous investigations, is not observed in experimental data.

In the last case C4, the wall temperature of the first measured point is already higher than the T_{pc}. This is similar as the experiment performed in supercritical CO_2 which is shown in Figure 2–8. The SST turbulence model failed to predict the wall temperature in this case. The reason is that the SST model is very sensitive to the changes of properties and turbulent parameters happening in the near wall sublayer. When the inlet temperature in experiment is very close to the pseudocritical temperature, the boundary layer in the inlet region becomes unsteady and therefore is very hard to predict by the SST model. It directly results in an ill-prediction of the flow development in the high enthalpy region. In the chapter 3.1.2, the local analysis in the properties proved that the RNG model is not capable of predicting the properties variation in the near wall region, and its better agreement with the measurement is a coincidence.

Shitsman (case D1)

In those previous simulations the RNG model has been found that it is insensitive to heat transfer deterioration in the vicinity of pseudocritical temperature. This insensitivity becomes more obvious in the case where buoyancy has a strong effect on the heat transfer. Buoyancy sensitivity study demonstrated that the Shitsman's data is strongly influenced by the buoyancy. Figure 2–14 shows that the RNG model completely failed to predict the heat transfer under such flow conditions. On the contrary, the SST model shows an outstanding performance. The prediction captures not only the first peak in wall temperature, but also the second deterioration with the following restoration of the heat transfer.

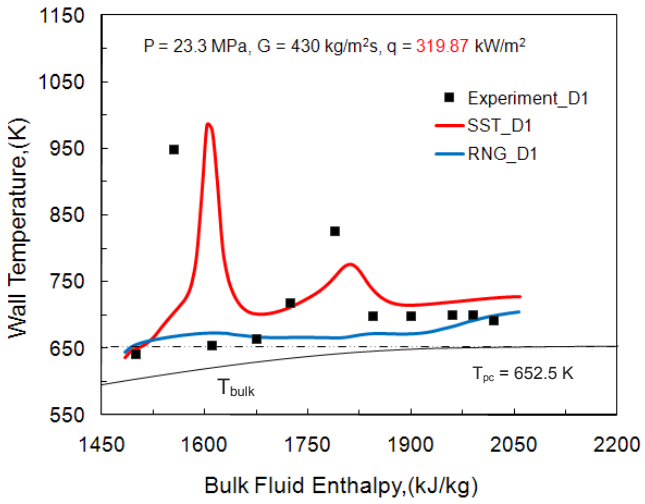

Figure 2–14: Model sensitivity study for tubes (Shitsman et al. [44])

Conclusions of Model Sensitivity Study for Annular Channels and Tubes

In order to test the capability of the SST model and the RNG model in terms of predicting heat transfer for supercritical water, four different datasets were used in this model sensitivity study. It has been demonstrated that under the same mesh structure and model configurations, the SST turbulence model has a better capability to predict the heat transfer behaviour of supercritical water flowing in vertical annular channel and tubes, especially when the heat transfer becomes deteriorated. The reason is that the SST model can deal with the turbulence situation near the wall much better than the RNG model does. More details about the near wall analyses are discussed in the chapter 3.1.

Hence, the SST k-ω turbulence model is recommended to be used under similar working conditions which have been tested in this study.

2.3.4 Turbulence Models Sensitivity Study for a Square Annular Channel

The purpose of this sensitivity study is to test the model performance in the non-circular channels, which is closer to the realistic flow channel in the fuel assembly. For the first sensitivity study, the SST k-ω model and the ωRSM are compared. The SST k-ω model has shown a good ability in circular tubes. However, a well-known shortcoming of the two-equation turbulence models is the inherent inability to predict the secondary flow which exists in the non-circular flow channels. That is the reason why the Reynolds Stress Models are used in this study. The model geometry and working conditions come from the experimental test performed by Li et al. [66]. Mass flux density is 800 kg/m^{2}s, and heat flux is 400 kW/m^2.

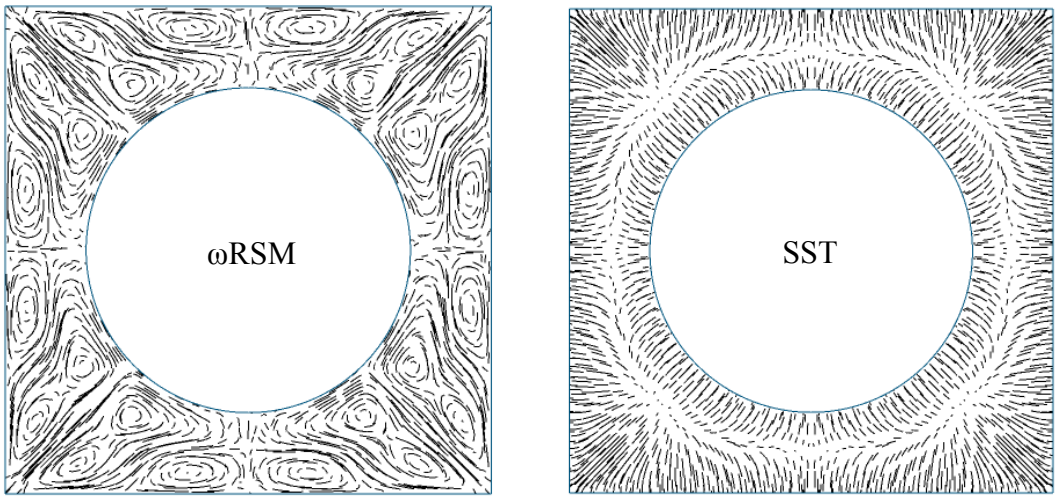

Figure 2–15: Top view of the flow streamlines in a square annular channel. Left: ωRSM, Right: SST

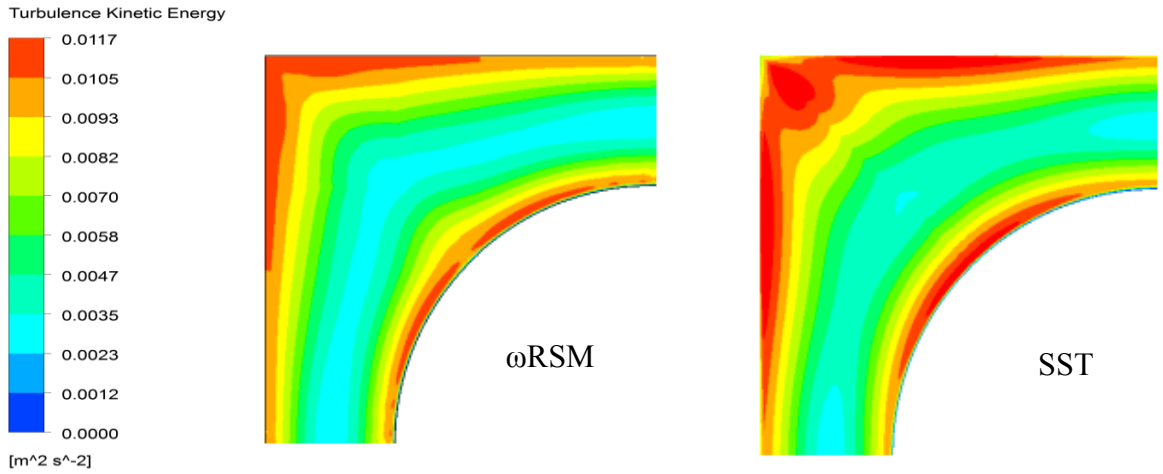

Figure 2–16: Turbulence kinetic energy comparison of ωRSM and SST

The water flow through a square annular channel has computed hydraulically without heat input. It means that the flow is fully developed in the flow channel. In Figure 2–15 the flow streamlines at a certain cut section in the channel are shown in a top view. The left figure illustrates a secondary-flow structure with 24 vortices as seen in the simulation. In the right figure there is no secondary flow predicted by the SST model using the Boussinesq approximation. Although there is no direct experimental data to compare with, the ωRSM obviously shows a better capability of capturing this feature.

Figure 2–16 shows the difference of the turbulence kinetic energy between the ωRSM and the SST. The *k* predicted by the SST model near the wall and on the surface of the rod is higher than that predicted by the ωRSM. Especially on the surface of the rod, the high-value layer of the *k* is discontinued in the middle, where it is the interface formed by two vortices, see Figure 2–15. This low value of *k* will result in a local hotspot in the temperature on the rod surface. The SST model shows a uniform layer on the rod surface, which means there will be no hotspot appearing in this region.

The second sensitivity study is carried out between the ωRSM and the SSG RSM model. The simulations are performed at a mass flux density of 315 kg/m^{2}s and at heat fluxes of 220 and 440 kW/m^2. Experimental test were stepwise performed with different inlet temperatures, and so do simulations. At a lower heat flux, the wall temperature can be correctly predicted by both of the ωRSM and the SSG RSM model in the lower enthalpy region, as shown in Figure 2–17 (left chart). However, when the wall temperature is higher than the pseudocritical temperature (T_{pc}), the SSG model failed to predict the abrupt increase of the wall temperature. On the contrary, the ωRSM results in a good agreement with measured data. This phenomenon is consistent with the model study for tubes and annular channel performed in chapter 2.3.3.

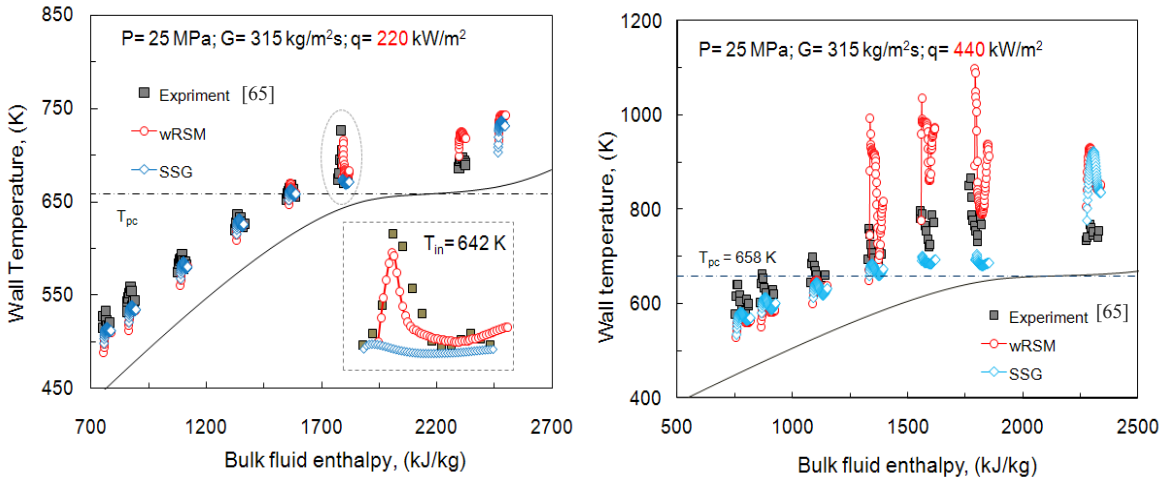

Figure 2–17: Model sensitivity study for a square annular channel.
Left: **low** heat flux; Right: **high** heat flux

The right chart in Figure 2–17 shows the comparison of calculated and measured results at a higher heat flux of 440 kW/m^2. Both of two models keep a good performance in low enthalpy region. In the higher enthalpy region (2000 kJ/kg > h > 1250 kJ/kg), the SSG model is still insensitive of the higher heat input and therefore shows an under-prediction in the wall temperature. The ωRSM results in a much higher wall temperature than experiments when the wall temperature passes through the pseudocritical point. Divergence between both of two models disappears when the bulk temperature is higher than the pseudocritical temperature ($T_w > T_b > T_{pc}$).

Considering the insensitivity of the SSG model and the good performance of the ωRSM, the latter will be used in the simulations for square annular channels.

2.3.5 Mesh Sensitivity Study for a WWR inside a Square Channel

A structured mesh for a WWR inside a square channel has been described in chapter 2.2.3 and shown in Figure 2–6. Compared with the unstructured mesh in Figure 2–18, this structured mesh allows us to distribute a fine mesh along the radial direction and a relative coarse mesh along the axial direction. The obvious advantage is that with an acceptable number of the elements, a good resolution can be achieved near the rod surface. At the same time, a length long enough to cover the whole enthalpy rise which is measured in experiment. Table 2–9 shows the comparison between unstructured and structured mesh on aspects of four parameters. With a same number of the elements, the structured mesh can reach a lower value of y_1^+ and a length five times longer than unstructured mesh. This could considerably save the computing time and ensure the viscous sublayer be fully resolved.

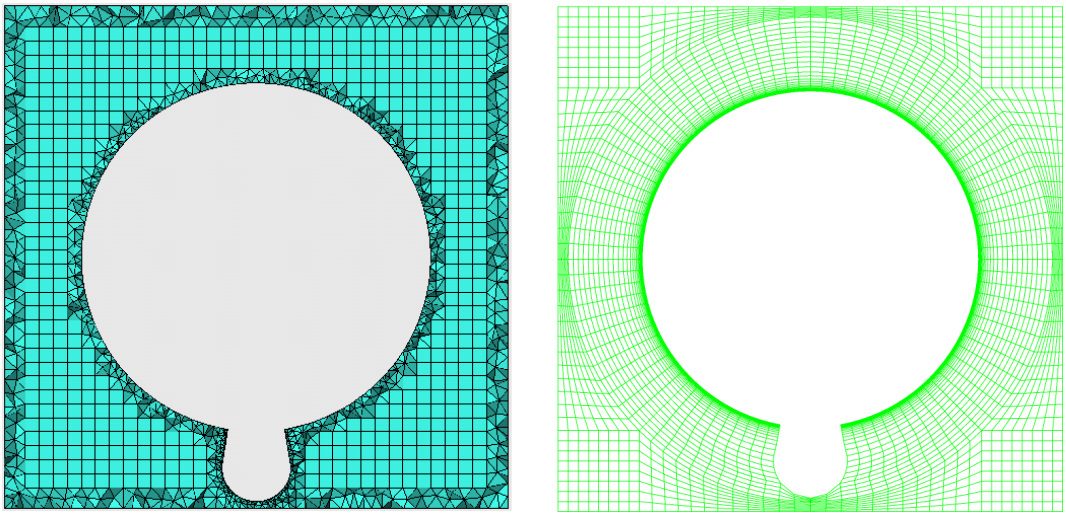

Figure 2–18: Unstructured mesh and Structured mesh for a WWR in a square channel

Mesh	cells number	y_1^+ to rod (the best we can do)	length (mm)	enthalpy rise
Unstructured	5×10^6	20	200	22 kJ/kg
Structured	5×10^6	0.1	1000	110 kJ/kg

Table 2–9: Comparison between unstructured and structured mesh

In order to evaluate the independency of the results on the computational mesh, a mesh independency study is performed for the structured mesh. In total 3 different mesh setups with 0.48×10^6 cells (Mesh I), 1.62×10^6 cells (Mesh II) and 5.73×10^6 cells (Mesh III) are investigated. The cell sizes are varied within the fluid domain. The y_1^+ value keeps constant in all three meshes, and the aspect ratio of the cells is changed depending on different meshes.

Figure 2–19 shows the results obtained by these three mesh setups. It needs to be mentioned that the surface temperature of the heated rod is non-uniform with local higher-temperature regions in the vicinity of the wire due to the interaction between the wire and the inner-corner of the square channel. Therefore it is necessary to distinguish the average cladding temperature (T_{ave}) from the maximum cladding temperature (T_{max}).

In Figure 2–19 three of the T_{ave} curves have no obvious differences. It means that the average cladding temperature is independent of the meshes. On the aspect of the maximum cladding temperature, the mesh II shows the best performance on the balance between the computing time and the accuracy. It is therefore chosen as the preferable mesh setup in the simulations for a wire-wrapped rod in a square channel.

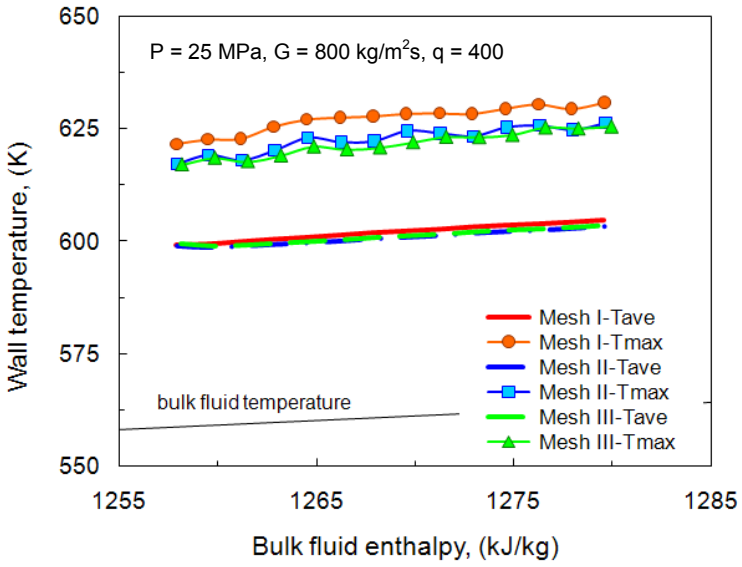

Figure 2–19: Mesh independency study for a WWR in a square channel

.

2.3.6 Turbulence Models Sensitivity Study for a WWR in a Square Channel

The sensitivity study is performed among three models, SSG RSM model, ωRSM and SST k-ω model. The aim of this study is to test the performance of the second-order closure model in the complex geometry, and in particular, to test the performance of the two-equation model for the purpose of shortening the computing time. The results of the comparisons are shown in Figure 2–20.

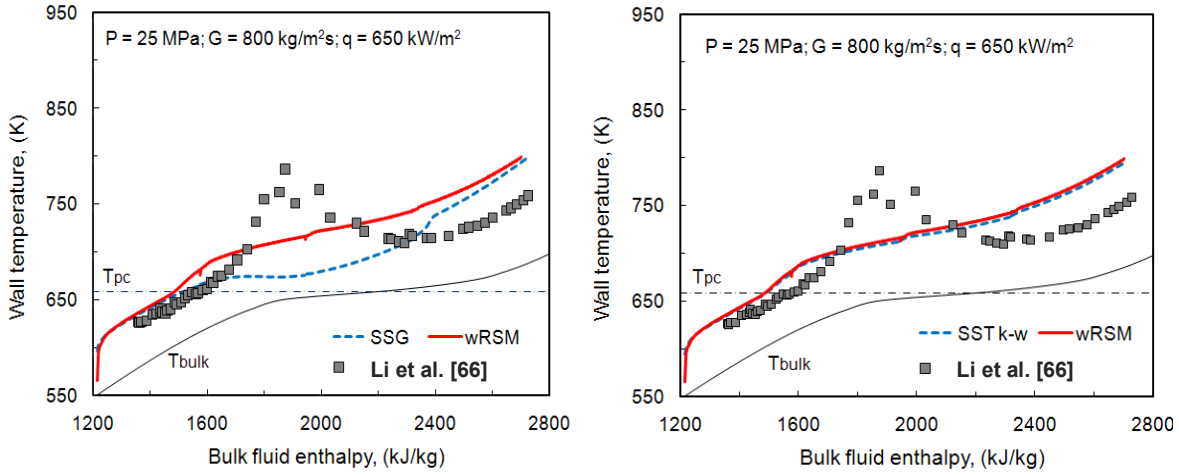

Figure 2–20: Comparisons among SSG, ωRSM and SST models for a WWR in a square channel. Left: SSG vs. ωRSM; Right: SST vs. ωRSM

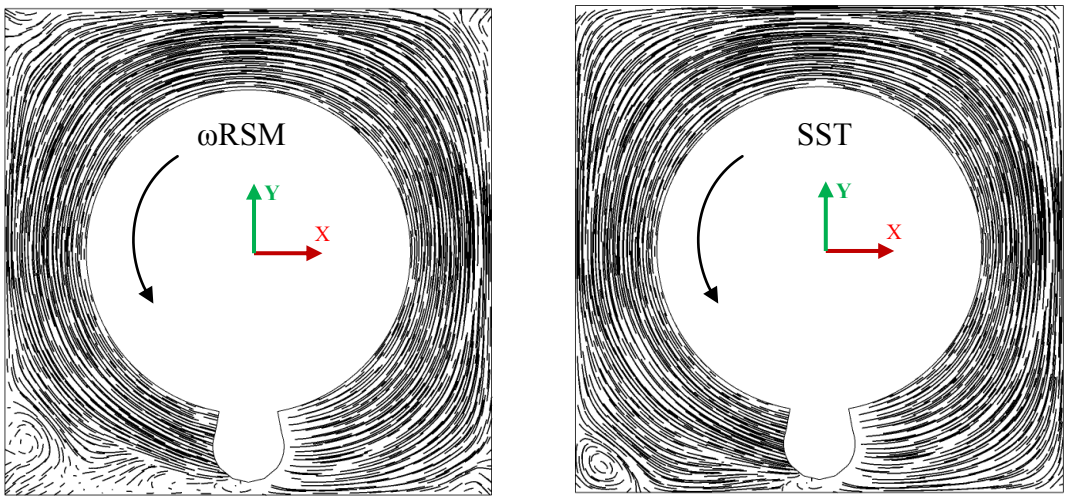

Figure 2–21: Top view of the flow streamlines for a WWR in a square annular channel.
Left: ωRSM, Right: SST

The experiment used for validation is carried out by Li et al. [66] and has been described in chapter 2.2.3. The experimental data is at a mass flux density of 800 kg/m^{2}s and a heat flux of 650 kW/m^2. The heat transfer is deteriorated under such a working condition and characterized by a local peak in the wall temperature.

As shown in the left chart, both of the SSG RSM model and the ωRSM cannot predict the local peak in the wall temperature. However, the ωRSM gives a rapid increase in the wall temperature when it passes through the pseudocritical point. On the contrary, an enhanced heat transfer is predicted by the SSG model near the bulk enthalpy of 1800 kJ/kg, where the measured heat transfer is just deteriorated. Although the ωRSM did not agree with the experiment perfectly, it shows a better performance than the SSG RSM model did in the case of HTD.

In the right chart the results predicted by the SST model and ωRSM are almost same. This is not surprising. Because under such a flow condition, the eddy viscosity generated mainly by gradients of the axial velocity component is too high for the representation of turbulent stresses acting as the secondary motion. Figure 2–21 illustrates that the swirl is generated by external forces (wire effect). This swirl differs from the secondary motions which are induced by non-isotropy of the stress tensor components in a non-circular channel (see Figure 2–15). This is the reason why those two streamlines charts in Figure 2–21 are almost identical.

After the model sensitivity study, it is clear that the SST model should be used in the simulation for a WWR in a square channel. The computing time consumed by the SST model is nearly half of that consumed by the ωRSM due to the six less equations. Furthermore, the simulations are much easier to converge by using the SST model.

2.4 Extension of the Turbulence Model

At positions where the pseudocritical temperature lies between the bulk and the wall temperatures ($T_w > T_{pc} > T_b$), the heat transfer may exhibit unusual behaviours such as the enhancement and the deterioration. Those phenomena are mostly caused by the properties variation near the heated wall. In order to account for the temperature-dependent effects some methods have been used to modify constant-property model. One of the methods uses the reference temperature to take the arithmetic mean of bulk and wall temperature as the characteristic temperature. Another method is the property ratio method which introduces an additional dimensionless function of values taken at bulk and wall temperature. At present, variable properties of the supercritical water have been implemented in the CFX 12.0 and other CFD codes. Different working groups obtained reasonable agreement in a certain range of parameters, but the overall accuracy is still unacceptable. This may be due to the fact that specific properties of turbulence in supercritical fluids are not taken into account in turbulence models, which have been developed for constant property fluids.

The variable properties implemented in the CFD code can be used directly for the laminar flow computation. However, the flows we are interested in are turbulent. In most of the CFD predictions, turbulence is accounted for by time-averaging in the RANS models, which is acceptable for the flow with constant properties. For supercritical fluids simulations, due to the nonlinear dependency of the fluid properties, it may be inappropriate to simply use the averaged value of the instantaneous parameters as the characteristic parameters in a turbulent flow. In general, any property taken at the local average temperature may differ from the mean property based on instantaneous temperature:

$$\overline{\phi}(T) \neq \phi(\overline{T}) \tag{2-27}$$

The divergence becomes more obvious in the vicinity of the pseudocritical point. For example, Bae et al. [80] found that the difference between $\overline{\rho}(T)$ and $\rho(\overline{T})$ is over 40% in the pseudocritical region. In particular, the error for the specific heat capacity, which varies most dramatically among all the properties, may then be unacceptable. Therefore a modified turbulence model, which is based on the probability distribution of the temperature T, is required. The previous work has been done by Laurien et al. [95].

2.4.1 Turbulence Modeling

In this study only the specific heat capacity c_p is modeled since it has the greatest variation among all the properties. The Reynolds stresses and the turbulent heat flux are modeled by the SST k-ω model. As described in chapter 2.1.2, the turbulent heat flux can be modeled with the molecular heat capacity $c_p(\overline{T})$ shown as follows:

$$q_j^{Re} = -\rho c_p \overline{u_j' T'} = \frac{\mu_t c_p(\overline{T})}{Pr_t} \frac{\partial \overline{T}}{\partial x_j} \tag{2-28}$$

where the turbulent Prandlt number is equal 0.9 in CFX. This is the standard approach which is used by almost all turbulence models. However, this molecular heat capacity $c_p(\overline{T})$ may not represent the correct heat transfer ability of the vortex heated up on one side and transferring the heat to the other side. As the pseudocritical temperature is between the bulk temperature and the wall temperature ($T_w > T_{pc} > T_b$), the heat capacity will exhibit a local maximum within the flow channel. However, the standard approach is inappropriate because the temperature fluctuations in time and space exist at any radial direction in a turbulent flow. That means, the exact pseudocritical temperature will only persist for a short time at a given radial direction. However, the molecular heat capacity $c_p(\overline{T})$ is determined directly from the mean temperature without accounting for the temperature fluctuations.

In order to take the temperature fluctuation into account, we denote the modified heat capacity as a "turbulent" heat capacity $\overline{c}_p(\overline{T})$. To examine the potential effects on the heat capacity by the temperature fluctuations, we approximate the statistical behaviour of any fluctuation via a Gaussian distribution. The probability for temperature fluctuation T' is expressed by Equation (2-29) and shown in Figure 2–22.

$$P(T', \sigma) = \frac{1}{\sqrt{2\pi\sigma}} \exp\left(-\frac{T'^2}{2\sigma^2}\right) \tag{2-29}$$

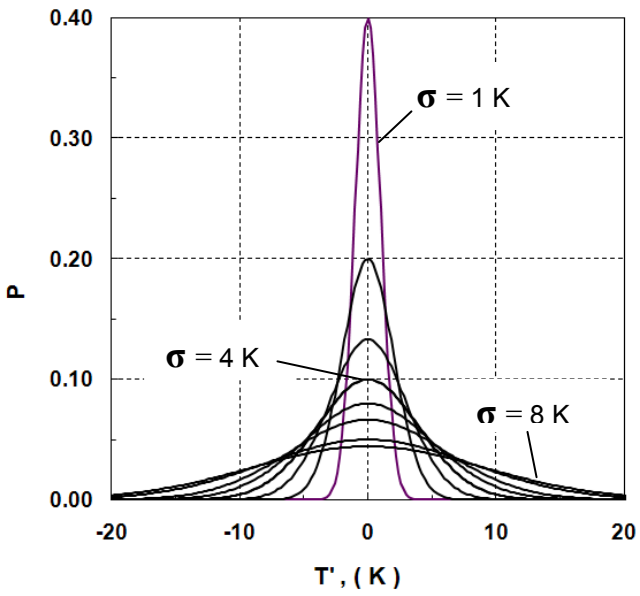

Figure 2–22: Gaussian density probability distribution of the temperature fluctuations

where σ is a parameter describing the probability density distribution. This parameter can be regarded as a measure for the normalized fluctuation intensity of turbulence. Based on this pdf-model, the "turbulent" heat capacity $\overline{c}_p(\overline{T})$ can be modelled by taking the temperature fluctuation into account. It is expressed as follows:

$$\overline{c}_p(\overline{T},\sigma) = \int_{-\infty}^{\infty} c_p\left(\overline{T}+T'\right)\cdot P(T',\sigma)\mathrm{d}T' \tag{2-30}$$

Here the temperature fluctuation T' is the integration variable. For practical calculations, the integration bounds are taken close to the values where P becomes almost zero. The modeled "turbulent" heat capacities $\overline{c}_p(\overline{T})$ are plotted in Figure 2–23.

As shown in Figure 2–23, the local peak of the effective heat capacity is significantly reduced in comparison with the original molecular $c_p(\overline{T})$ as the fluctuation level sigma (σ) increases. This is because the pseudocritical temperature becomes less and less likely to occur instantaneously in the vicinity of the pseudocritical point as the fluctuation level becomes higher and higher. The Gaussian function therefore acts as a smoothing operator with σ as a characteristic scale.

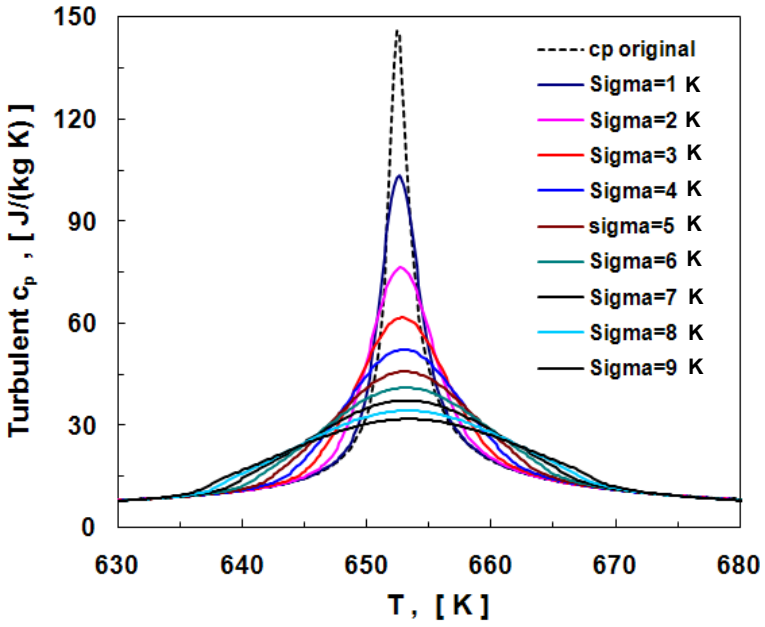

Figure 2–23: "Turbulent" specific heat capacity of water at 23.5 MPa.

This modified turbulence model results in a different relationship between the mean quantities $\overline{T}$ and $\overline{h}$. In the CFD code CFX, the mean enthalpy $\overline{h}$ is integrated once in a

pre-processing step when the thermal energy model is used. The general changes in enthalpy can be expressed as follows:

$$dh = \left(\frac{\partial h}{\partial T}\right)_p dT + \left(\frac{\partial h}{\partial p}\right)_T dp \tag{2-31}$$

However, for supercritical fluids of interest, it can be assumed that the properties are the functions of the temperature, but not the functions of the pressure. Hence, Equation (2-31) can be rewritten as:

$$dh = \overline{c}_p(\bar{T})dT \tag{2-32}$$

The enthalpy pre-process produces a table in which the mean temperature and the mean enthalpy are related together in the form of $\bar{T}(\bar{h})$. This relationship is later used at runtime to determine $\bar{T}$ from $\bar{h}$ whenever the mean temperature is needed.

Up to here, the whole idea of this modified turbulence model has been represented. Now the following question is: how to implement this model into a CFD code. The ideal implementation of this model requires two steps:

First step: Determination of the value of σ. The σ for a developed pipe flow can be expressed by:

$$\sigma = c \cdot l_T \left|\frac{\partial \overline{T}}{\partial r}\right| \tag{2-33}$$

where l_T is the local characteristic length scale of turbulence according to turbulence theory. It can be calculated by other turbulent parameters, e.g. $l_T = \sqrt{k}/\omega$ for the k-ω model. The parameter *c* can be used to adjust the model, and its value will be determined by the model validation.

Second step: variable σ utilization in the runtime. After the value of σ is determined in the first step, Equation (2-32) will be integrated and the results are stored in the form of tables in the pre-processing step in CFX. At the run time the respective array depending on variable σ will be used.

However, the ideal implementation is limited by technical reasons in CFX, which only allows a single array $\bar{T}(\bar{h})$ to be computed in the pre-processing step and the single corresponding table to be stored later. In other words, only a single value of σ could be used for each computational case in the present work. It means an assumption must be made that the turbulent fluctuation level is known and constant in the whole flow domain. Although the assumption results in an imperfect representative on the real situation, still the results

based on the assumption can be regarded as a useful approximation to examine the potential of the modified turbulence model.

2.4.2 Curve Fit of the "Turbulent" Heat Capacity

As shown in Figure 2–23, nine "turbulent" heat capacities need to be fitted and then implemented into the CFX by the so-called CFX Expression Language (CEL). A polynomial equation is used to fit the variable $\overline{c}_p(\overline{T})$ curve, shown as below:

$$\overline{c}_p(\overline{T},\sigma) = b1 + \frac{b2}{b3 \times (\overline{T} - b5)^2 + b4} \tag{2-34}$$

The constants in Equation (2-34) are listed in Table 2–10:

	b1	b2	b3	b4	b5
Original	4.836	-13000936.460	-20093.00	-98500.305	652.800
Sigma 1K	4.780	-6400688.802	-5580.272	-79058.992	653.000
Sigma 2K	4.758	-5898688.802	-4880.272	-81758.992	652.906
Sigma 3K	4.695	-5098688.037	-3080.813	-91775.182	652.900
Sigma 4K	4.608	-4218688.790	-2080.311	-91758.279	653.047
Sigma 5K	4.567	-4318688.036	-2080.545	-101775.541	653.091
Sigma 6K	4.516	-4317690.044	-1880.516	-111746.537	653.063
Sigma 7K	4.384	-8917871.822	-2900.033	-285746.233	653.214
Sigma 8K	4.307	-9718230.000	-3009.400	-330924.290	652.910
Sigma 9K	4.258	-9718230.152	-3009.04058	-335710.8437	653.049

Table 2–10: Constants in the polynomial equation (2-34).

The fitting approach (or fitting equation) differs from the one in the previous work [95], in which a blending function and an additional term are used with two basic equations to fit the curve of specific heat capacity. The current polynomial equation gives a simple and consistent form for all nine curves. In the future work, this polynomial equation could be easier implemented in a subroutine by CEL to realize the ideal variable-sigma in the modified turbulence model.

2.4.3 Results and Discussion on the Turbulent Heat Capacity

The model is tested in comparison with two experiments of Glushchenko [60] for an annular channel flow with a gap width of 1mm. The experimental data is at a mass flux density of 2200 kg/m^{2}s and a relative low heat flux of 1150 kW/m^2.

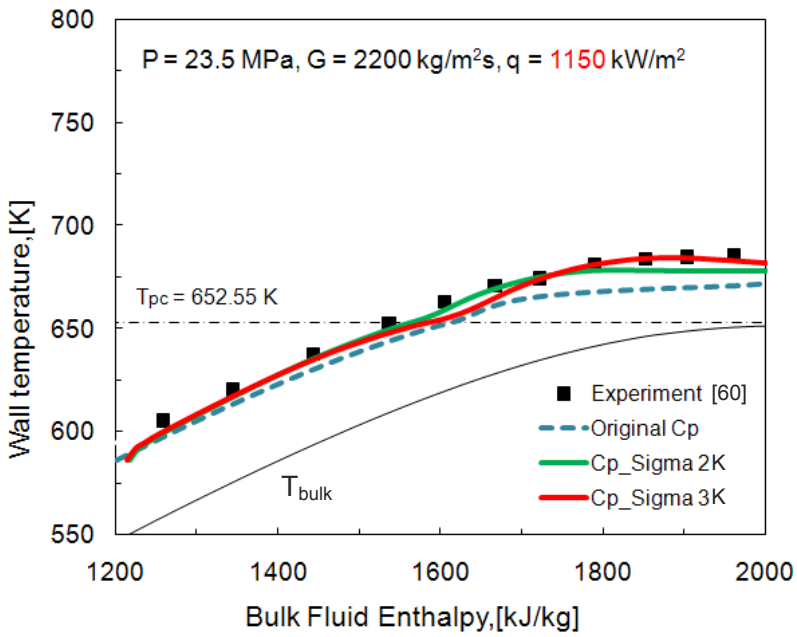

Figure 2–24: Comparison of modified and original turbulence model in a case of NHT

This case can be classified as the type of normal heat transfer (NHT). The comparison results are shown in Figure 2–24.

At a lower heat flux, the standard approach based on the original heat capacity leads to an under-prediction of the wall temperature as compared to the experiment in the wall temperature. The deviations to experiments become larger in the high enthalpy region. In contrast, modified model improves the agreement to the experiment in some places when the wall temperature starts to pass through the pseudocritical point. σ=2K results in an improvement when the wall temperature just passes beyond the T_{pc}, and σ=3K gives the improvement downstream in the higher enthalpy region, respectively.

In order to obtain more details about the improvement caused by the modified model, we choose three axial positions at different enthalpies for a deeper investigation. Those three positions are illustrated in Figure 2–25, where the wall temperature versus bulk fluid enthalpy is plotted. The first position (green rhombus) at the enthalpy of 1500 kJ/kg represents the case in which there is no obvious difference in the wall temperature between the modified and standard model (original heat capacity). The second position (orange dot) at the enthalpy of 1640 kJ/kg represents the case in which σ=2K improves the agreement to the experiments while the σ=3K does not. The third position (blue triangle) at the enthalpy of 1800 kJ/kg represents the case in which good agreement is found between σ=3K and experiment. All three gray squares mean the results predicted by the standard model at the same enthalpy corresponding to the modified model, respectively.

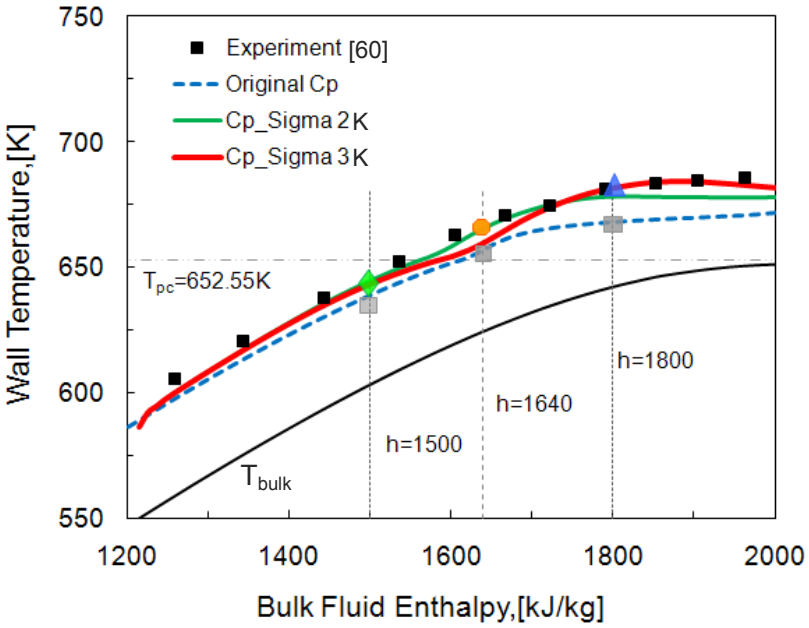

Figure 2–25: Illustration of the different axial positions for the details analysis

For the modified model with a sigma value of 3K, we take two positions to demonstrate the effect of the "turbulent" heat capacity. One is at the wall temperature below pseudocritical temperature ($T_w < T_b$) where the results predicted by σ=3K and original heat capacity are nearly the same, and anther is at the region of $T_w > T_b$ where the σ=3K shows an improvement on the heat transfer prediction and results in a better agreement with the experiment.

The associated cp profiles versus bulk fluid enthalpy are plotted in Figure 2–26 (a). At a bulk enthalpy of 1500 kJ/kg, the heat capacities are nearly the same. It is because the heat capacities differ from each other only in the vicinity of the pseudocritical point. The heat capacities variations occurring only near the wall region indicate that the wall temperature is developing closer to the T_{pc}. On the contrary, the difference of heat capacities at the enthalpy of 1800 kJ/kg is more remarkable. The high value of heat capacity in the standard model (original heat capacity) leads to a greater ability of this flow to store the thermal energy coming from the heated wall. Therefore the wall temperature is lower than that in the case of σ=3K which matches better with the experiment.

The effect resulted from "turbulent" heat capacity is more obvious in Figure 2–26 (c), in which the turbulent kinetic energy (k) versus radial direction is plotted. As shown in the chart, the standard model predicted higher value of the turbulent kinetic energy in the near wall region and hence results in an optimistic ability in heat transfer and the lower wall temperature compared with the experiment.

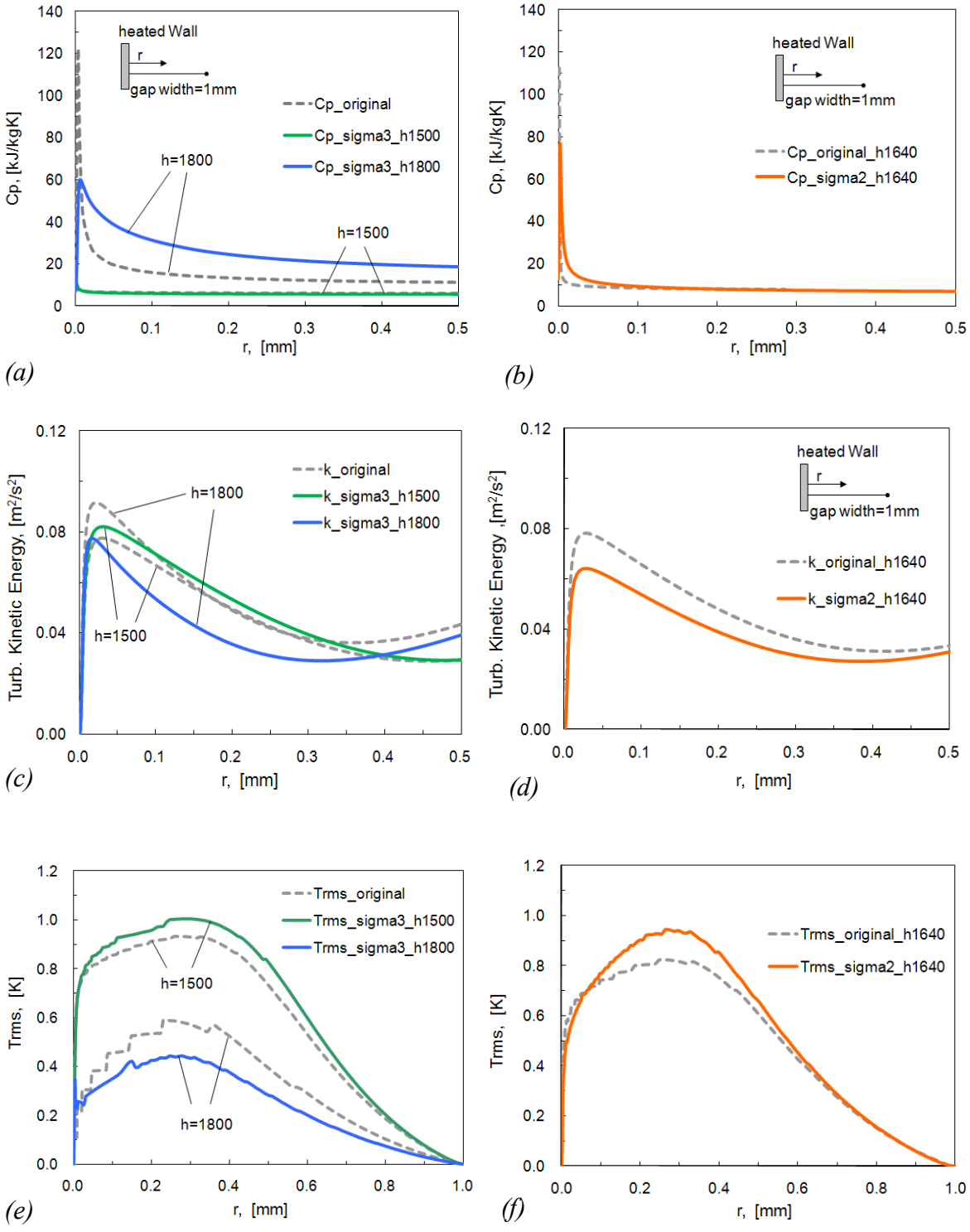

Figure 2–26: Comparison between modified and standard model at three different enthalpy positions. (a) and (b): Heat capacity, (c) and (d): Turbulent kinetic energy; (e) and (f): Root mean square of *T* Left column: σ=3K. Right column: σ=2K

For the modified model with a sigma value of 2K, we take the enthalpy of 1640 kJ/kg as the reference position to compare the modified model and standard model. Figure 2–26 (b) shows the comparison of the σ=2K and original heat capacity along with the radial direction. The standard model results in a peak of heat capacity, whose value is almost twice than the value of cp predicted by the modified model. And similarly, modified model leads to a lower value of the turbulent kinetic energy than that predicted by the standard model. The improved agreement with experiment demonstrates that the modified model with a sigma value of 2K predicts the turbulent situation correctly near the enthalpy of 1640 kJ/kg.

In order to check the ability of the SST k-ω model to predict the anticipated fluctuation level, the root mean square (rms) value of temperature (T_{rms}) for σ=2K and σ=3K are plotted along with radial direction in Figure 2–26 (e) and (f), respectively. It can be seen that the profiles of T_{rms}, estimated by $T_{rms} = l_T|\partial\bar{T}/\partial r|$, show similar trends in simulations of the modified and standard models; however, there are slight difference in the magnitude. Based on these results, the parameter c in Equation (2-33) can be estimated by the expression of $c = \sigma / max(T_{rms})$. The data in Figure 2–26 (e) and (f) suggest the value of c = 7.5 in the high enthalpy region and the value of c=2 in the low enthalpy region, respectively.

Preliminary Conclusions for the pdf-Turbulence Model

A new statistical model, which takes the effect of the turbulent temperature fluctuations on the specific heat capacity into account, is presented here. It uses an effective heat capacity (or turbulent heat capacity) in the simulation rather than the molecular heat capacity.

The preliminary results shown above demonstrate the significance of recognizing the difference between $c_p(\bar{T})$ and $\overline{c}_p(\bar{T})$, as well as the potential capability of this pdf-turbulence model improving the prediction of the heat transfer in the supercritical water.

However, the improvement occurring in the different enthalpy region indicates that a constant sigma cannot correctly represent the temperature fluctuations in the whole enthalpy region and is therefore inappropriate in an ideal pdf-turbulence model. An ideal implementation of this model in a CFD code should use the numerically predicted fluctuation level, e.g. calculated in Equation (2-33), rather than a constant value. This pdf-turbulence model needs to be further investigated and validated in details. Data from DNS or experimental data with turbulent quantities measured carefully is therefore required.

3 Results and Discussion

In the previous chapter, comprehensive sensitivity studies have been performed with respect to the near wall treatment, the mesh independency, the buoyancy effect and the turbulence models. Based on the results of those studies, appropriate turbulence model with a correct model configuration and a suitable mesh strategy can be generated and utilized on the flow conditions which we are interested in. Furthermore, by carrying out all those sensitivity studies, we have obtained not only the way to generate a correct model, but also some knowledge to understand the heat transfer characteristics in supercritical fluids. In this chapter, the study on the heat transfer behaviour of the supercritical fluids will continue and extend to a wider range of working conditions to gain a deeper insight into the heat transfer behaviour and also the mechanisms of heat transfer deterioration, which is one of the most important targets in this work.

Before starting with the results of simulations, it is worth mentioning the importance of the experimental data which are used to validate the models in this study. The quality of the experimental data, which is mainly evaluated by the error bounds provided by the experimentalists, is of primary importance for a successful validation exercise. Unfortunately, most experiments still do not provide this information. Moreover, even if error estimates are available, they cannot exclude systematic errors by the experimentalist. It is therefore desirable to have an overlap of experimental data, which allow testing the consistency of the measurements. For example, different experimental groups in different facilities have carried out the experiments with similar flow structures and flow physics. This is the reason why we extend the validation study for tubes to a wide range of experimental datasets, which are performed by different researchers.

In order to provide confidence in the experiments and the quality of the experimental data, a careful check to the quality and accuracy of any measurement used as a validation test data is one of the prerequisites for a correct validation. The availability and reliability of the water data in tubes has been tested and summarized by Löwenberg et al. [16]. In this study, part of the tubes data is coming from Löwenberg's database which does not take the HTD into account, and the other tubes data (HTD) is coming from the researchers whose other data (non-HTD) has been already tested by Löwenberg. The reliability testing for other experimental data is hardly carried out due to its uniqueness. Good reputation of the researchers and a comprehensive description of the experiment proved the reliability of those data to a certain extent.

3.1 Annular Channels and Tubes

3.1.1 Annular Channel Flow of Supercritical CO_2

Three cases of vertical upward flow in an annular channel are simulated based on the test conditions from Bae and Kim [71]. Figure 3–1 shows the comparison of predictions and experiments at different mass flux densities and wall heat fluxes. The fluid flows upward in a vertical annular channel with a gap width of 1 mm. The SST k-ω turbulence model is used with an y_1^+ value of 0.1 on the heated wall.

For a low mass flux density and a low heat flux (G = 400 kg/m^{2}s, q = 30 kW/m^2), the wall temperature versus bulk fluid enthalpy is plotted in Figure 3–1 (a). The wall temperature T_w shows a slight discrepancy in the magnitudes in the low enthalpy region ($i_b < i_{pc}$), while a good agreement between predictions and experiments is found in the high enthalpy region ($i_b > i_{pc}$).

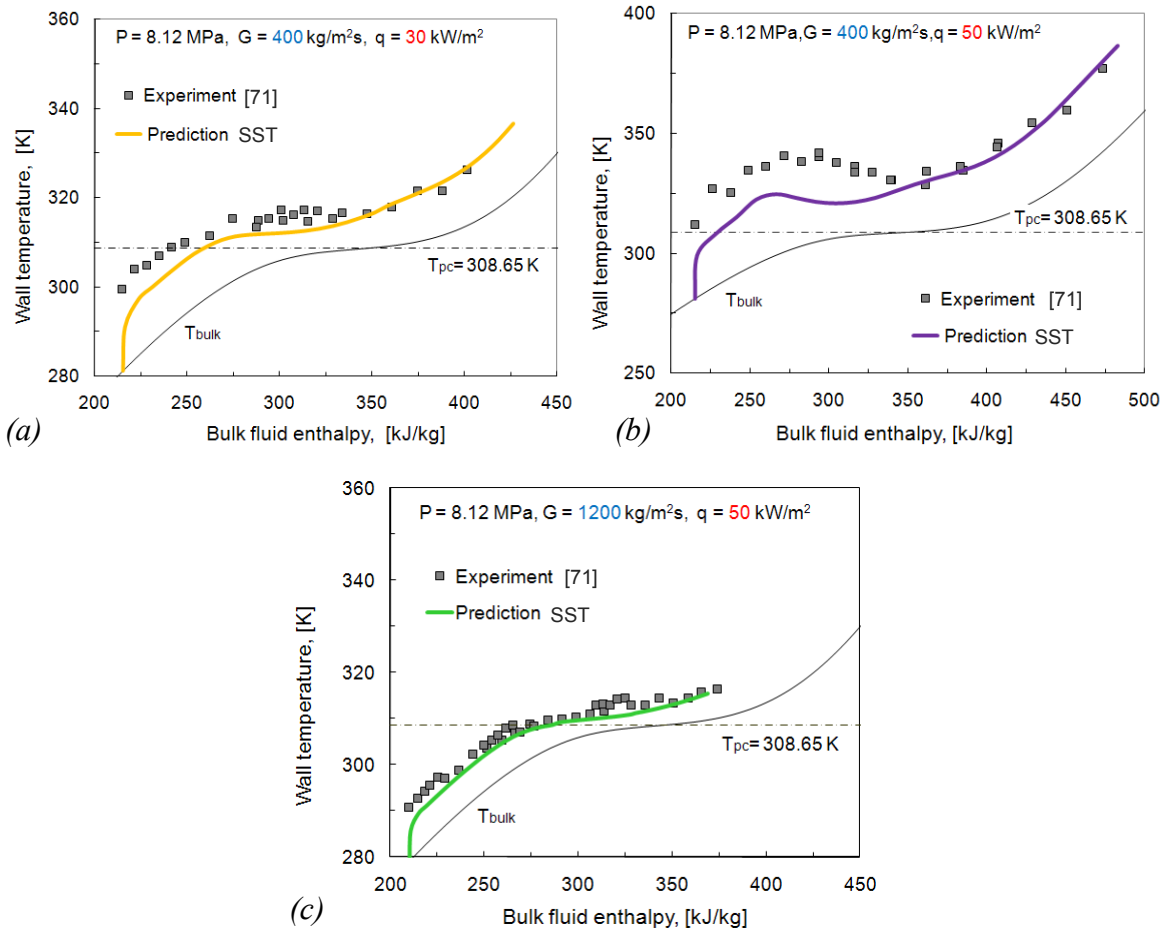

Figure 3–1: Comparison of predictions and experiments in the wall temperature at the cases of CO_2

As the heat flux is increased, the wall temperature measured in experiment strongly increases at the beginning of the heated section. Figure 3–1 (b) shows that the wall temperature is already above the pseudocritical temperature in the first measuring point. This type of HTD is strongly influenced by the inlet conditions where the thermal boundary layer has not yet been fully developed and therefore is difficult to be numerically predicted. As seen in the Figure 3–1 (b), the present numerical failed to predict this inlet effect. The measured and simulated wall temperatures show similar trends, however, there is a non-negligible difference in magnitude near the inlet region. As the flow develops to the higher enthalpy region ($i_b > i_{pc}$), the good agreement is found between predictions and experiments.

For a high mass flux density (G = 1200 kg/m^{2}s), the wall temperature versus bulk fluid enthalpy are plotted in Figure 3–1 (c). Along the whole enthalpy region, the agreement between predicted and measured wall temperature has been considerably improved, especially near the inlet region. It is because that in this measurement the inlet temperature is far below the T_{pc} and therefore leads to a much weaker inlet effect on the heat transfer.

It can be found out that in all three cases the predictions match well with the experiments in the high enthalpy region ($i_b > i_{pc}$) and show discrepancy in the low enthalpy region ($i_b < i_{pc}$). The difference seen between simulations and the measurements is probably due to the factors that are not modeled in CFD code. These effects could be very likely induced by the missed inlet information. Nevertheless, the measured and simulated results show a good similarity at all three working conditions.

At a low mass flux density (400 kg/m^{2}s), it is possible that the buoyancy effects strongly affect the flow and consequently cause the HTD. In order to test the buoyancy effect, simulations with and without buoyancy are performed with identical model configurations. The comparison result shown in Figure 3–2 indicates that the buoyancy has a very limited effect on the heat transfer. The HTD in this case is caused by other factors.

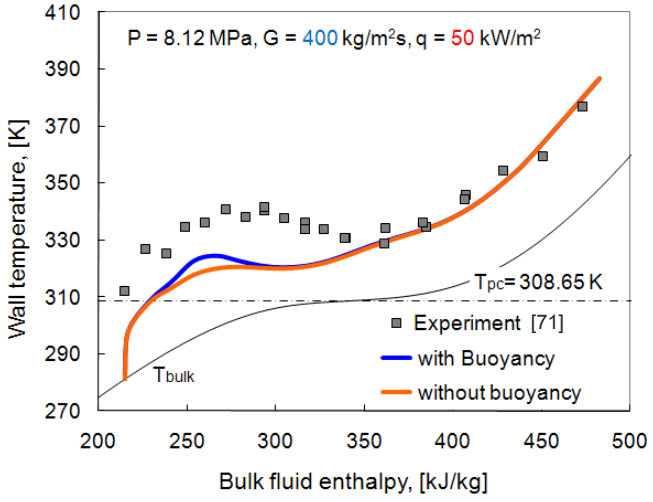

Figure 3–2: Buoyancy effect study in a HTD case of supercritical CO_2, SST k-ω model

3.1.2 Annular Channel Flow and Pipe Flow of Supercritical Water

There are four experimental datasets at different working conditions and diameters used for simulation in this study. These experiments are performed by different researchers individually: Glushchenko et al. (23.5 MPa, gap width of 1mm), Ornatskii et al. (25.5 MPa, D = 3 mm), Yamagata et al. (24.52 MPa, D = 7.5 mm) and Shitsman et al. (23.3 MPa, D = 8 mm). Simulation results by SST k-ω model and further discussions are described below.

Glushchenko (case A)

The experimental tests to supercritical water were carried out by Glushchenko et al. [60] in an inner-heated, vertical annular channel. The width of the annular gap is 1 mm. The test matrix covering the selected cases is listed in Table 3–1. The ranges of variation of the working parameters are as follows: pressure kept at a constant value of 23.5 MPa, specific wall heat flux of up to 2.96 MW/m^2, mass flux density of 2200 kg/m^{2}s. The pseudocritical temperature T_{pc} is 652.5 K at pressure of 23.5 MPa.

	Pressure, (P)	Mass flux density, (G)	Heat flux, (q),	Flow direction
A1	23.5 MPa	2200 kg/m²s	1.15 *MW/m²*	upward
A2			2.41 *MW/m²*	upward
A3			2.96 *MW/m²*	upward

Table 3–1: Working conditions in the cases of Glushchenko et al. [60]

Three cases for supercritical water at different heat fluxes are simulated and compared with measurements in the wall temperature. Figure 3–3 represents the results in charts of wall temperature versus bulk fluid enthalpy. For a low heat flux (q = 1.15 MW/m^2), good agreement is found in the whole region of enthalpy measured in experiment, seen in Figure 3–3 (a). The slight discrepancy between predictions and experiments is likely due to the ill-predicted temperature fluctuation, which has been explained in the chapter 2.4.

For a higher heat flux (q ≥ 2.41 MW/m^2), the measured wall temperature increases abruptly as it passes beyond the T_{pc}. This type of HTD differs from the one in the case of CO_2. First, the onset of HTD is far away from the flow inlet, rather than beginning at the inlet. Second, the heat transfer is not restored in the measurement, in other words, the wall temperature does not decrease after the onset of HTD. At a heat flux of 2.41 MW/m^2, Figure 3–3 (b) shows a good agreement between predictions and experiments in the low enthalpy region ($i_b < i_{pc}$). Most importantly, the onset of HTD has been captured with a slight shift to a lower enthalpy. This slight difference perhaps results from the turbulence model and the unmodeled factor, e.g. the wall roughness.

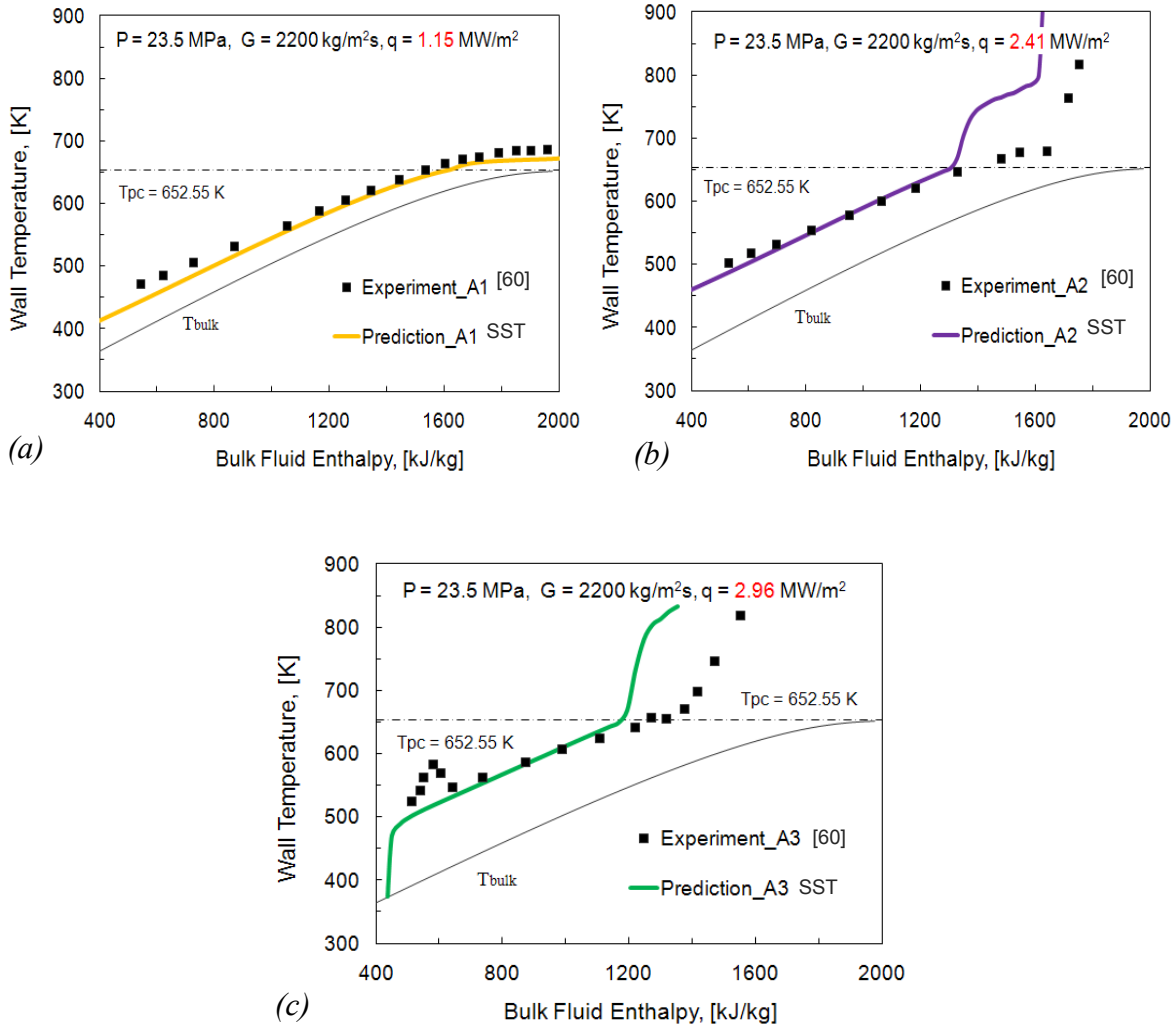

Figure 3–3: Comparison of predictions and experiments for the cases of Glushchenko et al. [60], SST k-ω model

At a heat flux of 2.96 MW/m^2, the comparison result between predictions and experiments is quite similar as that in case A2: a good agreement found in the low enthalpy region ($i_b < i_{pc}$) and an "earlier" prediction of the onset of HTD. However, there is an apparent temperature spike occurring at the beginning of the experiment, which is not predicted by the model. The mechanism responsible for this temperature spike is likely due to the unmodeled inlet effect, which was also mentioned by the experimentalist in his paper [60].

In chapter 2.3.3 the result of model sensitivity study for case A2 demonstrated that the SST model shows a better performance than the RNG model with respect to the HTD prediction. In order to gain more knowledge on the differences between those two models and further explain the physical details of the onset of the HTD, the case A2 at a heat flux of 2.41 MW/m^2 is investigated in further detail.

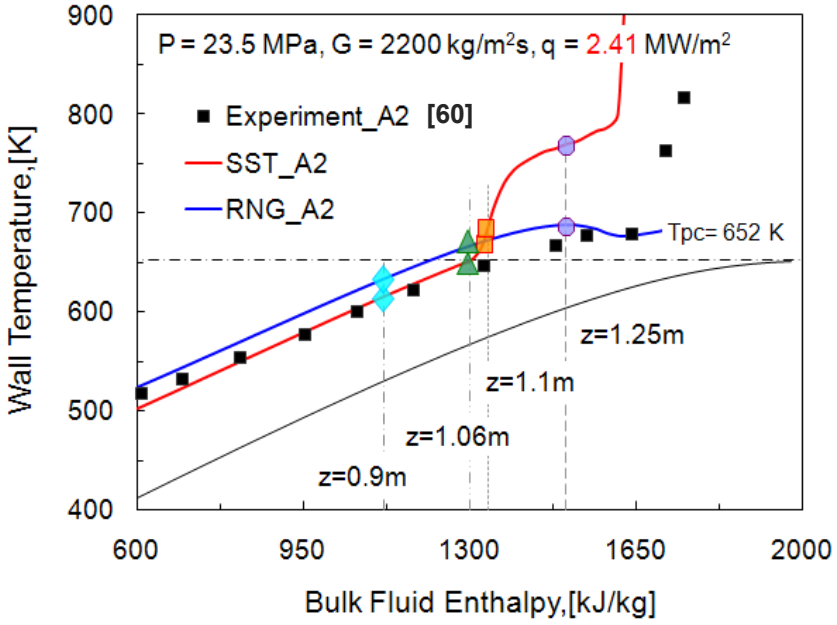

Figure 3–4: Illustration of 4 different axial positions in case A2 for analysis in detail

As shown in Figure 3–4, four axial positions are used to illustrate the development of fluid properties and other local parameters. Because of the identical mesh and model configuration, same axial position corresponds with same enthalpy. Therefore those four axial positions can be plotted in a chart of the wall temperature versus bulk fluid enthalpy.

Figure 3–5 shows the development of fluid properties and other local parameters versus the radial direction for case A2. These fluid properties and local parameters used here are specific heat capacity (cp), thermal conductivity, density, turbulent kinetic energy (k) and axial velocity (W). Results predicted by the SST mode are listed in the left column, and those predicted by RNG are listed in the right column. The non-dimensional coordinate y^+ is regarded as a "wall unit" relevant for the extension of the different layers of the wall-bounded turbulence. It can be calculated by:

$$y^+ = (R-r)^+ = \frac{(R-r)\cdot u_\tau \cdot \rho}{\mu}, \quad u_\tau = \sqrt{\tau_w/\rho} \tag{3-1}$$

The value of y^+ equal to 12.8 is often regarded as the thickness of the laminar sublayer, within which turbulence effects are less important. In all these charts, $y^+ \approx 12.8$ has been plotted in the corresponding radial direction. It can be seen that enough mesh nodes have been distributed in the laminar sublayer which is surely fully-resolved.

Because all important processes occur very close to the heated wall, the near wall region is therefore zoomed in, and an additional sketch illustrates the gap width (or diameter for tubes) and the position of the heated wall.

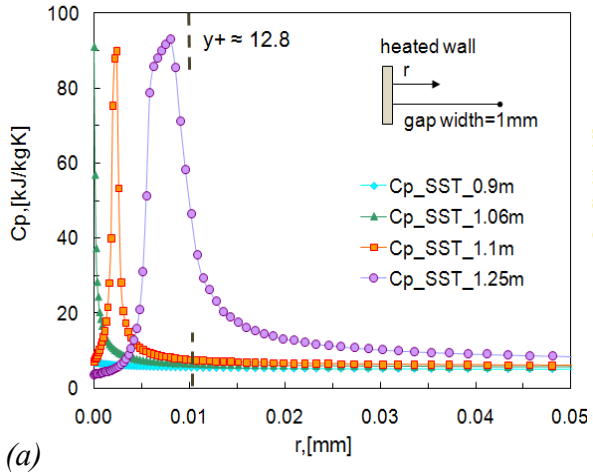
y+ ≈ 12.8
heated wall
r
gap width=1mm
Cp_SST_0.9m
Cp_SST_1.06m
Cp_SST_1.1m
Cp_SST_1.25m
Cp,[kJ/kgK]
r,[mm]

(a)

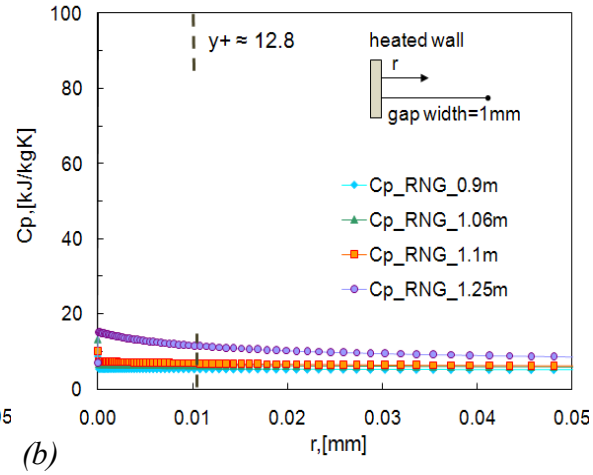
y+ ≈ 12.8
heated wall
r
gap width=1mm
Cp_RNG_0.9m
Cp_RNG_1.06m
Cp_RNG_1.1m
Cp_RNG_1.25m
Cp,[kJ/kgK]
r,[mm]

(b)

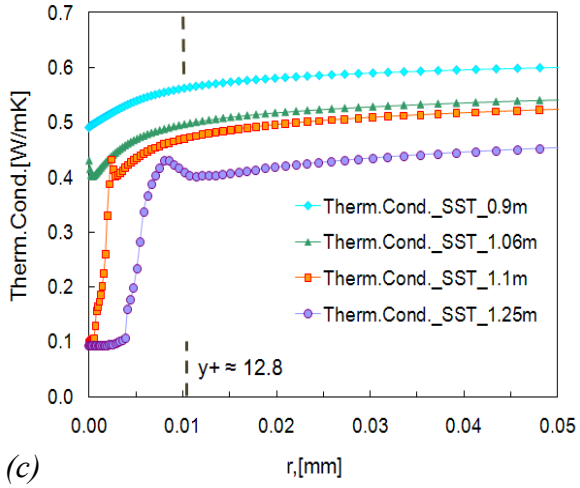
Therm.Cond._SST_0.9m
Therm.Cond._SST_1.06m
Therm.Cond._SST_1.1m
Therm.Cond._SST_1.25m
y+ ≈ 12.8
Therm.Cond.[W/mK]
r,[mm]

(c)

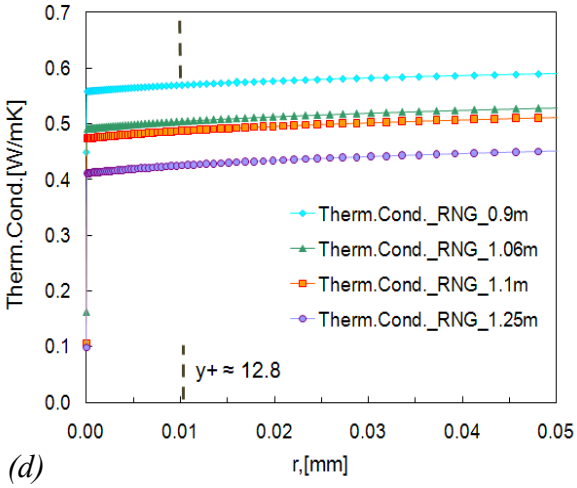
Therm.Cond._RNG_0.9m
Therm.Cond._RNG_1.06m
Therm.Cond._RNG_1.1m
Therm.Cond._RNG_1.25m
y+ ≈ 12.8
Therm.Cond.[W/mK]
r,[mm]

(d)

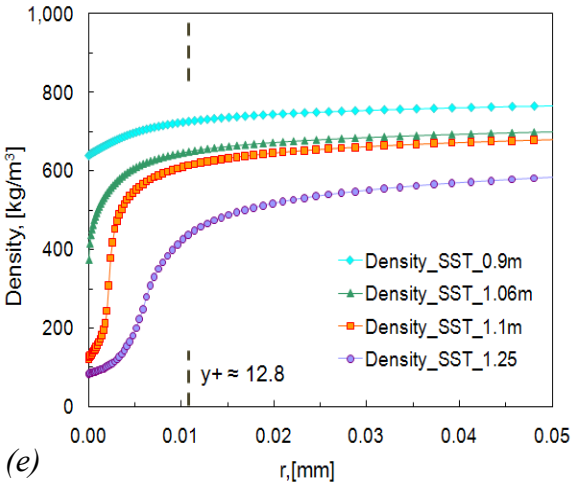
Density_SST_0.9m
Density_SST_1.06m
Density_SST_1.1m
Density_SST_1.25
y+ ≈ 12.8
Density, [kg/m3]
r,[mm]

(e)

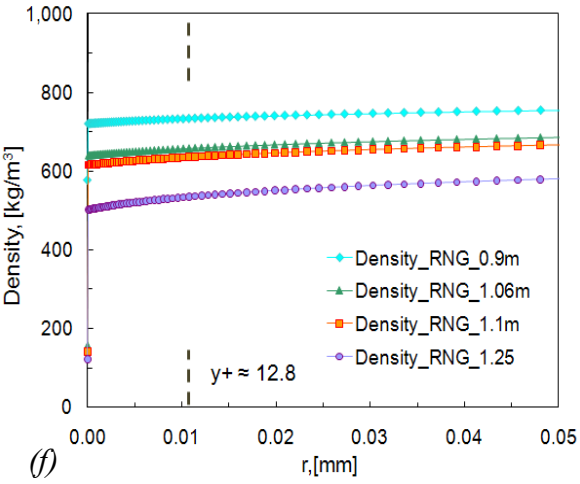
Density_RNG_0.9m
Density_RNG_1.06m
Density_RNG_1.1m
Density_RNG_1.25
y+ ≈ 12.8
Density, [kg/m3]
r,[mm]

(f)

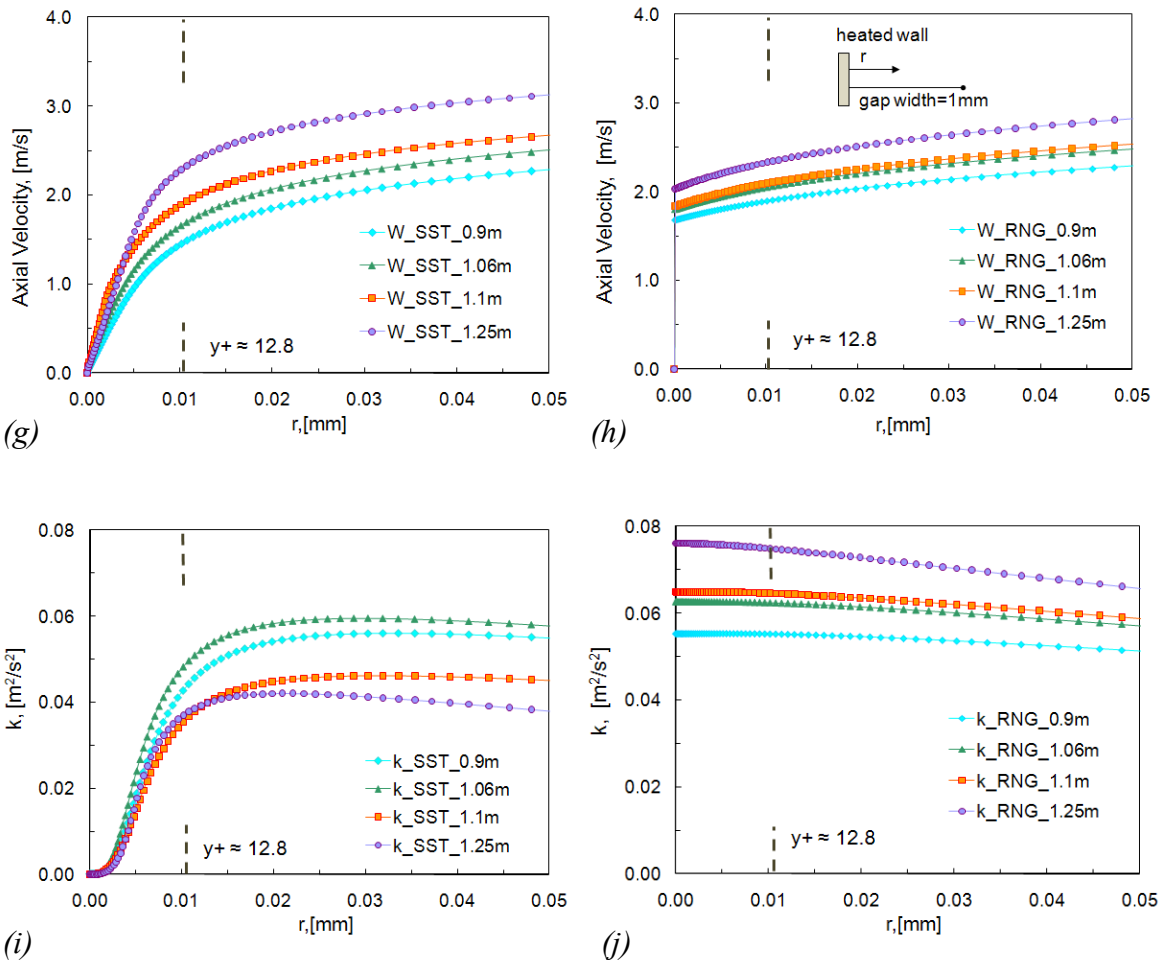

Figure 3–5: Radial profiles of thermal-hydraulic properties (a)-(f); turbulent kinetic energy (i)-(j); and axial velocity (g)-(h) at different axial cross sections (Case A2).
Left column: SST. Right column: RNG

For the SST model, the heat capacity (cp) and thermal conductivity profiles along with axial position are plotted in Figure 3–5 (a) and (c), respectively. It can be seen that the cp starts to increase near the heated wall (orange squares) as the wall temperature increases close to the T_{pc}, which indicates an increasing ability of near wall fluid to absorb the heat from the heated wall. However, the heat conductivity decreases simultaneously and forms a low-value layer near the wall which results in an impaired ability of the heat conduction in the laminar sublayer. These two effects, the positive one from the high-value layer of cp and the negative one from the low-value layer of heat conductivity, are canceled out to each other and therefore have no effect on the heat transfer before the pseudocritical point. When the wall temperature is beyond the T_{pc} (purple dots and green triangles), the high-value layer of heat capacity moves away from the heated wall and becomes more localized within the laminar sublayer. On the contrary, the low-value layer of heat conductivity has been formed near the wall and impairs the heat transfer acting as a “heat insulation layer”. Consequently, the integral effect of both heat capacity and heat conductivity results in the heat transfer deterioration.

For the SST model, the density and axial velocity profiles along with radial direction are plotted in Figure 3–5 (e) and (g), respectively. As the flow develops downstream, the density near the heated wall strongly decreases along with the wall temperature passing beyond the T_{pc}. However, this dramatic variation of the density does not lead to an obvious shape change of the velocity profile along the radial direction due to a large mass flux density. In Figure 3–5 (i) the turbulent kinetic energy (k) increases laterally from the value of zero at the wall to a constant value of about $0.05 m^2/s^2$ in the core. The downstream decrease of k is mainly due to the acceleration effect caused by the axial density variation. Hence, the deterioration occurred in the vicinity of T_{pc} is independent of the buoyancy effect and can be classified into the first type of HTD. The second type of HTD will be discussed in the case of Shitsman.

For the RNG model, all results are listed in detail in the right column shown in Figure 3–5. It is clear that the RNG model cannot predict the properties variation in the near wall region. All of the thermo-physical properties and the other local parameters have almost been treated constant. In the core region, the SST and RNG show quite the same behaviours for the prediction of the properties. However the ill-prediction of properties in the near wall region results in a flat profile of the wall temperature and thus no HTD occurs near the T_{pc}.

Ornatskii (case B)

In this section, the experimental tests in supercritical water flow in tubes were carried out by Ornatskii et al. [57]. The pipe diameter is 3 mm. The test matrix covering the selected cases is listed in Table 3–2. The first two cases are downward flow in tubes and the last case B3 is upward flow in a tube. The ranges of variation of the working parameters are as follows: pressure kept at a constant value of 25.5 MPa, specific wall heat flux of up to 1810 kW/m^2, mass flux density of 1500 kg/m^2s. The pseudocritical temperature T_{pc} is 660 K at a pressure of 25.5 MPa.

	Pressure, (P)	Mass flux density, (G)	Heat flux, (q), kW/m^2	Flow direction
B1	25.5 MPa	1500 kg/m^2s	1320	downward
B2			1630	downward
B3			1810	upward

Table 3–2: Working conditions in the cases of Ornatskii et al. [57]

Three cases of the supercritical water with different heat fluxes are simulated and compared with measurements in the wall temperature. The results are shown in Figure 3–6 in charts of wall temperature versus bulk fluid enthalpy. For the downward flow (cases B1 and B2), good agreement can be found in the low enthalpy region ($i_b < i_{pc}$), seen in Figure 3–6 (a)

and (b). However, the onset of HTD is predicted with a shift towards the higher enthalpy region compared with measurement.

For an upward flow (case B3), Figure 3–6 (c) shows the results at a heat flux of 1810 kW/m^2. Very good agreement is found for the wall temperature before the heat transfer is restored at the enthalpy of 1800 kJ/kg. The onset of HTD is captured by the model at the correct position where the wall temperature just passes beyond the T_{pc}. Furthermore, the following development of the wall temperature predicted by the SST model is almost the same as those measured until its local peak. After this local peak, there is a discrepancy in the wall temperature profile between predictions and experiments. Nevertheless, the similar trends of the restored heat transfer indicate that the current model can predict not only the onset of HTD, but also the following restoration of the heat transfer.

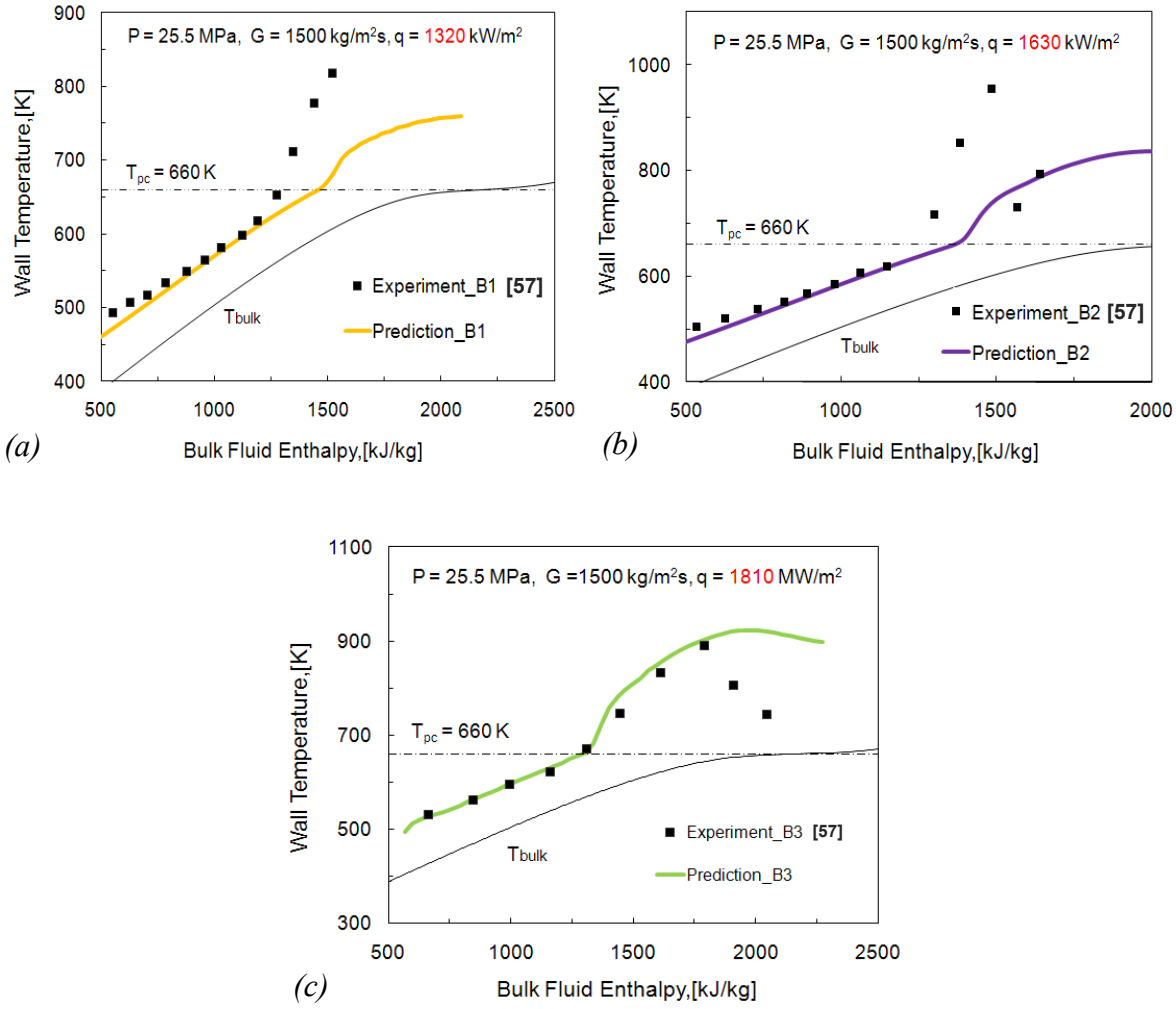

Figure 3–6: Comparison of predictions (SST k-ω model) and experiments for the cases of Ornatskii et al. [57]

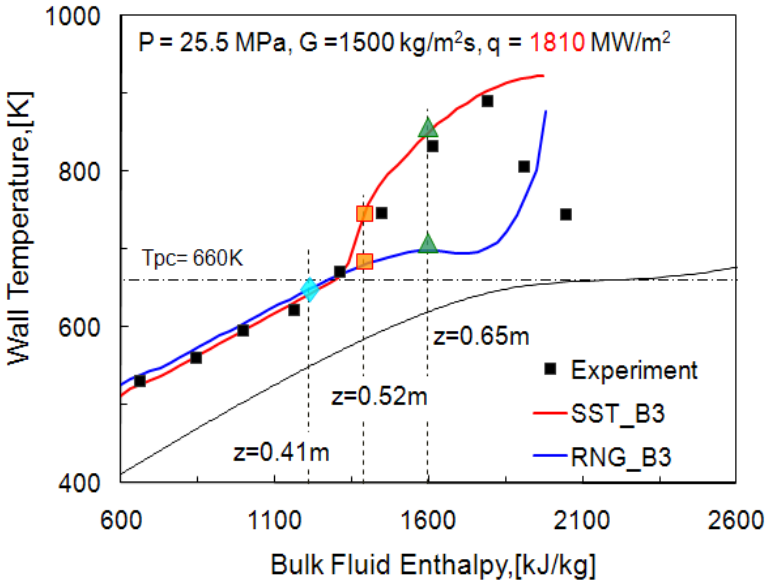

Figure 3–7: Illustration of 3 different axial positions in case B3 for analysis in detail

In order to gain more knowledge on the mechanisms of the HTD in the cases of Ornatskii's experiments, three axial positions, which locate before and behind the pseudocritical point, are chosen to perform the detailed analysis. The axial positions and the comparison results between the predictions and measurement are plotted in Figure 3–8. The position of $y^+ \approx 12.8$ calculated by Equation (3-1) is drawn in each of the charts to represent the laminar sublayer.

For the SST model, the heat capacity (cp) and thermal conductivity profiles along with axial position are plotted in Figure 3–8 (a) and (c), respectively. It can be seen that the cp starts to increase near the heated wall (blue rhombuses) as the wall temperature increases close to the T_{pc}, and the heat conductivity decreases simultaneously forming a low-value layer near the wall which results in an impaired ability of the heat conduction in the laminar sublayer. When the wall temperature is beyond the T_{pc} (orange dots and green triangles), the high-value layer of heat capacity moves away from the heated wall and becomes more localized within the laminar sublayer. The "heat insulation layer" formed by the low-value of heat conductivity increases the thermal resistance and cancels out the benefit from the high-value of heat capacity. The integral effect leads to the deterioration on the heat transfer.

Figure 3–8 (e) and (g) show the density and axial velocity profiles along with the radial direction for the SST model. It can be seen that the density variation along the radial direction has still no effect on the heat transfer, although a slight shape change of the velocity profile is found in the near wall region as the wall temperature passes beyond the T_{pc} (orange dots).

These phenomena are quite similar as those observed in the cases of Glushchenko. However, there is a restoration of the heat transfer which is characterized by the decrease in the wall temperature found in the measurement. The similar trends are predicted by the model. Figure 3–8 (i) shows the turbulent kinetic energy (k) profile along with the radial direction. As the HTD occurs, it is associated with a reduction in the turbulent kinetic energy (orange dots). When the slope of the increase in the wall temperature becomes flatter, which indicates a restoration of the heat transfer, an increased turbulent kinetic energy is illustrated by the green triangles in the vicinity of the laminar sublayer (y+ ≈ 12.8)

For the RNG model, all results in detail are listed in the right column in Figure 3–8. The profiles of the thermo-physical properties, axial velocity and k are almost constant only with a small variation near the heating region. The ill-prediction of properties in the near wall region results in a flat profile in the wall temperature and thus no HTD occurs near the T_{pc}.

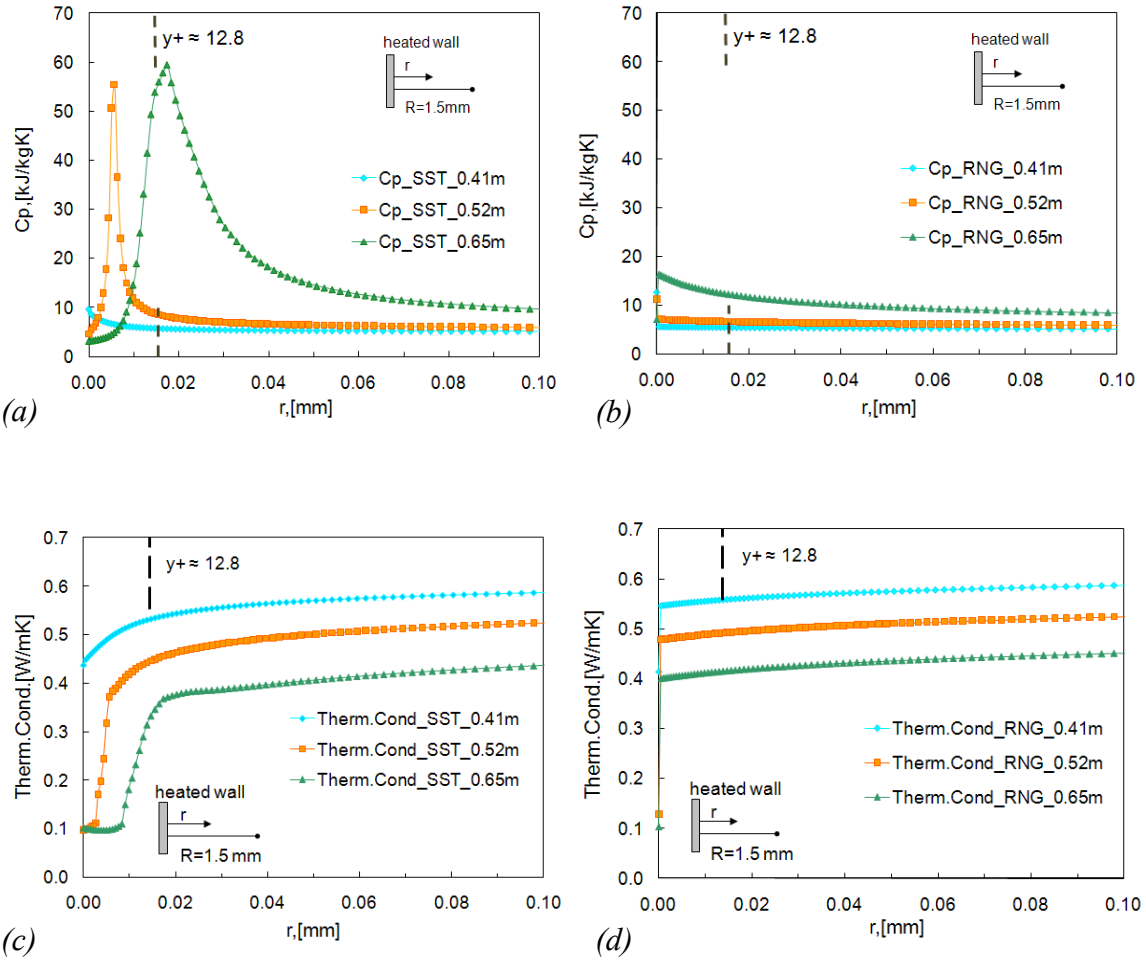

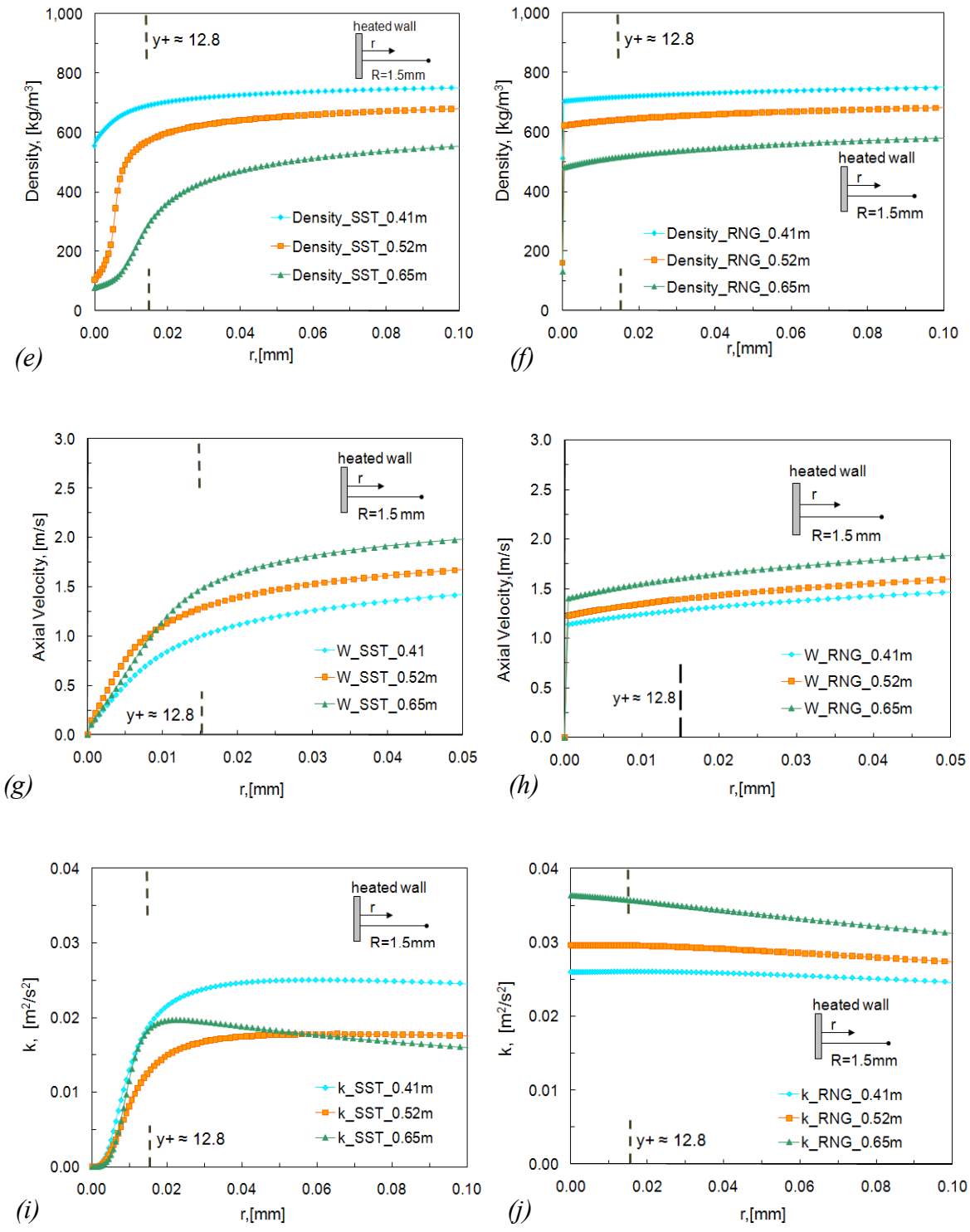

Figure 3–8: Radial profiles of thermal-hydraulic properties (a)-(f); turbulent kinetic energy (i)-(j); and axial velocity (g)-(h) at different axial cross sections (case B3).
Left column: SST. Right column: RNG

Yamagata (Case C)

Yamagata et al. [50] carried out the experimental tests to supercritical water flow in tubes, which are one of the most popular data and have been wildly used to validate the numerical model. The pipe diameter is 7.5 mm. The test matrix covering the selected cases is listed in Table 3–2. The first two cases are downward flow in tubes and the last case B3 is upward flow in a tube. The ranges of variation of the working parameters are as follows: pressure kept at a constant value of 24.5 MPa, four specific wall heat fluxes of up to 930 kW/m^2 and a mass flux density of 1260 kg/m^{2}s. The pseudocritical temperature T_{pc} is 656.3 K at the pressure of 24.52 MPa. SST k-ω turbulence model has been used in all simulations.

	Pressure, (P)	Mass flux density, (G)	Heat flux, (q), *kW/m²*	Flow direction
C1	24.5 MPa	1260 kg/m²s	233	upward
C2			465	upward
C3			698	upward
C4			930	upward

Table 3–3: Working conditions in the cases of Yamagata et al. [50]

For all four cases, the comparison of predictions and experiments is plotted in the charts of wall temperature versus bulk fluid enthalpy (see Figure 3–9). At low heat fluxes of 233 and 465 kW/m^2, a good agreement between the predictions and measurements is found along the whole enthalpy region, as seen in Figure 3–9 (a) and (b). The slight discrepancy near the low enthalpy region may be due to the unmodeled parameters at the inlet of measurement.

At a heat flux of 698 kW/m^2, the deviation between predictions and experiments becomes obvious when the wall temperature passes beyond the pseudocritical temperature ($T_w > T_{pc}$), as shown in Figure 3–9 (c). However, the similar trends in the wall temperature indicate that the agreement may be improved in the high enthalpy region if more information near the inlet is given. At a heat flux of 930 kW/m^2, the model failed to predict the wall temperature since the first measured point. The difference between predictions and experiments is more remarkable at this heat flux. It is probably still due to the unmodeled parameters at the inlet. Actually, calculating from the outlet upstream to the inlet might be a promising solution to deal with this type of heat transfer, which is strongly affected by the inlet condition.

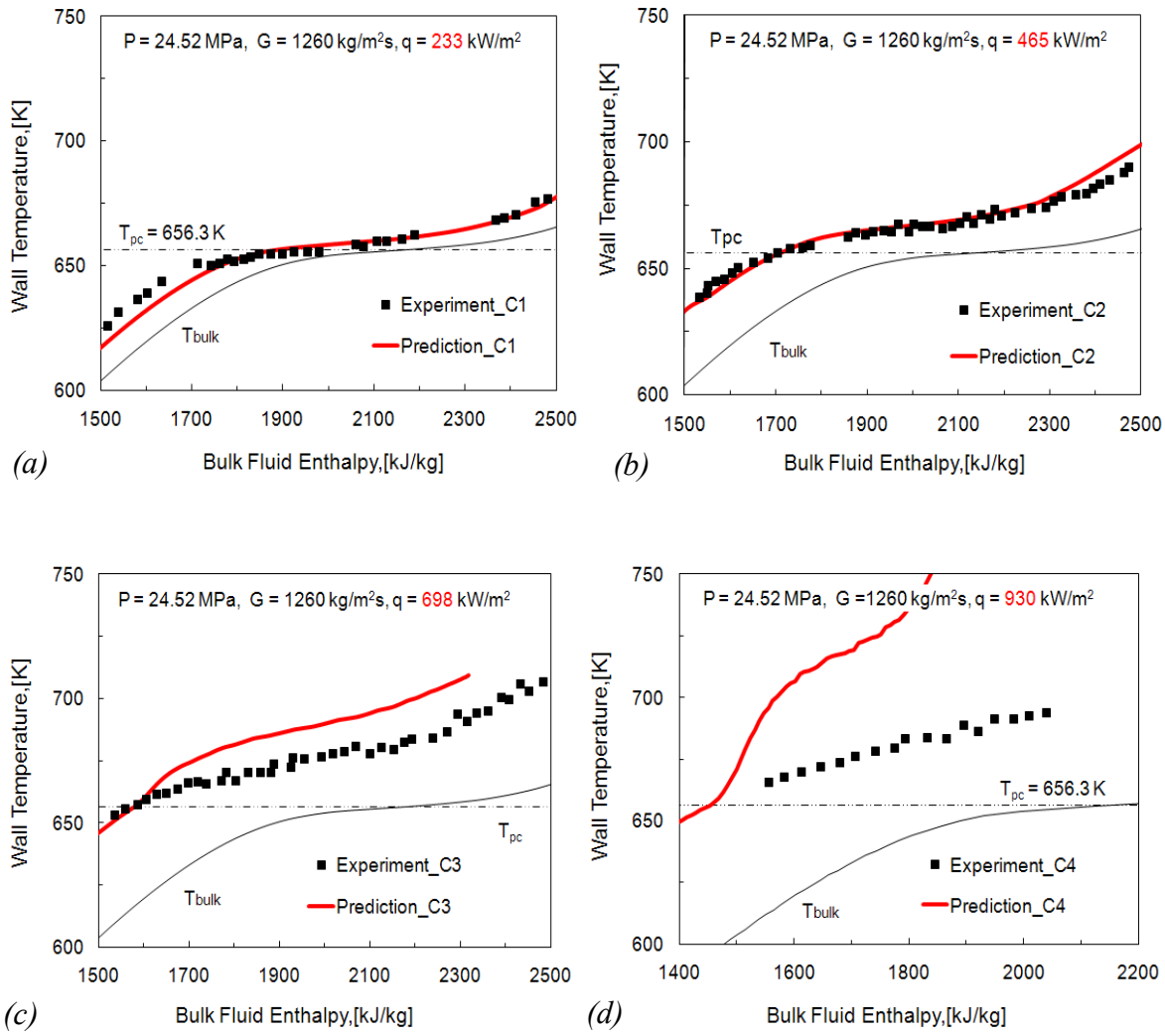

Figure 3–9: Comparison of predictions (SST k-ω turbulence model) and experiments for the cases of Yamagata et al. [50]

Figure 3–10 illustrates three axial positions along the pipe for the SST and RNG model, respectively. The different performance between the SST and RNG model in case C4 has been discussed with respect to the development tendency in the model sensitivity study (chapter 2.3.3). The RNG model shows a better prediction than the SST model in terms of the average value of wall temperature. However, the enhanced heat transfer near the enthalpy of 1900 kJ/kg is not observed in experimental data. On the contrary, the SST model gives a similar trend in the wall temperature compared with measurement. Hence, from an essential point of view, the prediction by SST model represents the heat transfer behaviour better than the RNG model. This opinion can be proved by an investigation on the local parameters, such as thermo-physical properties, axial velocity and turbulent kinetic energy. The analyses in detail are shown in Figure 3–11.

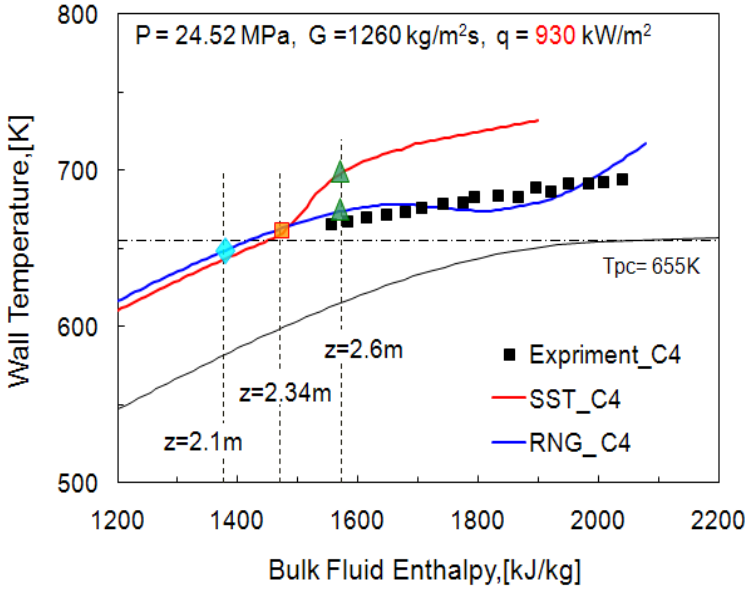

Figure 3–10: Illustration of three different axial positions in case C4 for analysis in detail

For the SST model, the heat capacity (cp) and thermal conductivity profiles along with the axial direction are plotted in Figure 3–11 (a) and (c), respectively. It can be seen that the cp starts to increase near the heated wall (blue rhombuses) as the wall temperature increases close to the T_{pc}, and then its peak moves towards the core of the tube along with the temperature increasing. The heat conductivity near the wall decreases and forms a low-value layer increasing the thermal resistance in the laminar sublayer. Based on the indication of $y^+ \approx 12.8$, it can be found that the abrupt variations of both of properties are occurring mostly in the laminar sublayer, and the values of cp and thermal conductivity keep constant in the core region. These phenomena have been observed by many experiments and therefore are correct in terms of thermo-physical process. For the RNG model, however, the heat capacity profile shows a much wider region with high-values, and the thermal conductivity varies slightly in the near wall region with a high value more than twice than that predicted by the SST model. That means the prediction of the RNG model is too optimistic for the wall temperature.

Figure 3–11 (e) and (g) show the density and axial velocity (W) profiles along with the radial direction for the SST model. The density variation does not cause a shape change of the axial velocity, but results in flow acceleration downstream along the axial direction. In Figure 3–11 (i) the turbulent kinetic energy (k) increases laterally from the value of zero at the wall to a constant value of about $0.015 m^2/s^2$ in the core. It is worth mentioning that the transition area of the k developing from zero to a constant value matches well with the position of $y^+ \approx 12.8$ which is calculated by Equation (3-1). It demonstrates that the SST model has an outstanding ability of predicting the thermal-hydraulic behaviour in the near wall region.

Depending on the previous analyses, it is no surprise that the RNG model predict the density and axial velocity invariably in the near wall region (see Figure 3–11 (f) and (h)). The turbulent kinetic energy is also over-predicted, which leads to an enhanced heat transfer in the vicinity of the T_{pc}. Hence, it can be concluded that the better agreement shown in the charts of T_w versus i_b is a coincidence due to the ill-predicted properties and turbulent parameters.

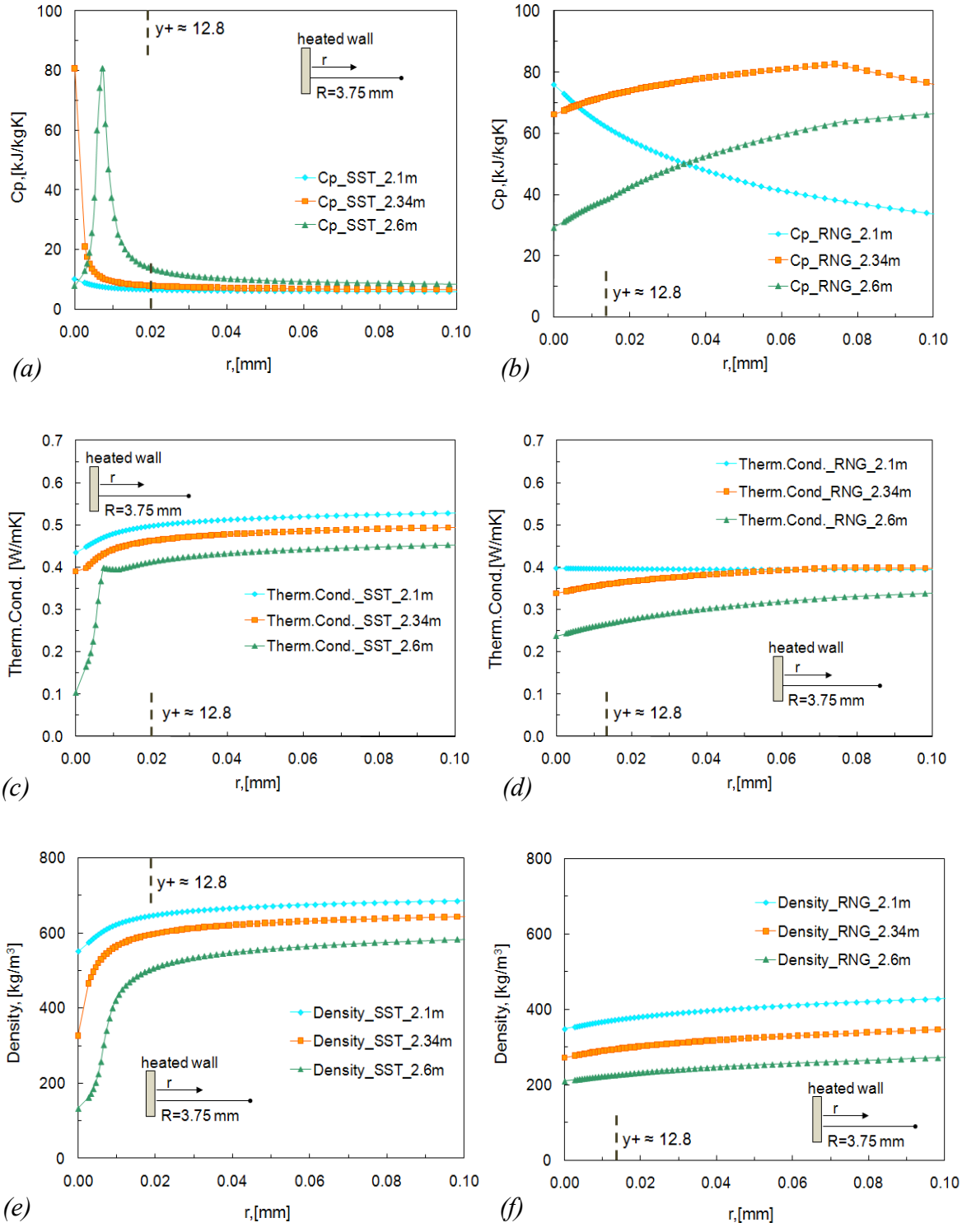

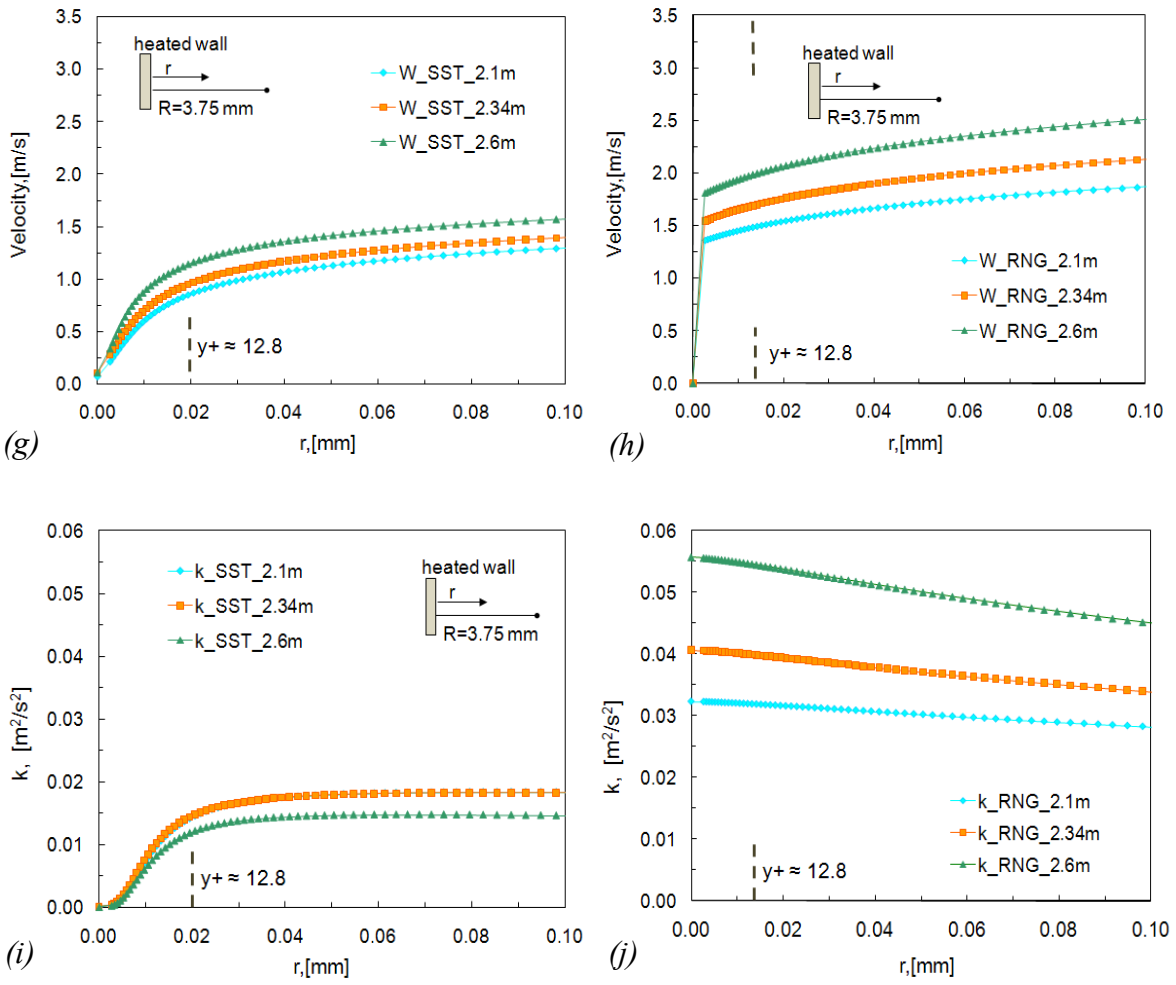

Figure 3–11: Radial profiles of thermal-hydraulic properties, turbulent kinetic energy and axial velocity at different axial cross sections (case C4). Left column: SST. Right column: RNG

Shitsman (Case D)

Shitsman et al. [44] carried out the experimental test to supercritical water flow in a tube. The water flows upward in a pipe of a 8mm diameter. As listed in Table 3–4, the mass flux density and the specific wall heat flux are 430 kg/m²s and 319.87 kW/m^2, respectively. The pseudocritical temperature T_{pc} is 652.55 K at a system pressure of 23.3 MPa. A difference between case D and the other cases discussed above is the low mass flux density. Jackson and Hall [113] state that at a low mass flux density the turbulent diffusivity is reduced for upward flow when the low-density wall layer becomes thick enough to reduce the shear stress in the region where energy is typically fed into the turbulence. It is so called “near wall buoyancy effect”. In the previous cases A, B and C the near wall buoyancy effects do not occur due to the high mass flux density. Therefore this case is chosen in order to represent the second type of HTD caused by buoyancy effect at a low mass flux density.

	Pressure, (P)	Mass flux density, (G)	Heat flux, (q),	Flow direction
D1	23.3 MPa	430 kg/m²s	319.87 kW/m²	upward

Table 3–4: Working condition in the case of Shitsman et al. [44]

The comparison between predictions and experiments is shown in Figure 3–12. Good agreement is found in the whole enthalpy region with a slight discrepancy in the magnitude. Previous studies in chapter 2.3 have revealed the inability of the RNG model and the importance of the buoyancy effect, which are illustrated in Figure 2–10 Figure 2–14 respectively. In this section, analyses of the development process of the local properties and parameters are carried out in order to gain more insights on the mechanisms of the buoyancy affected HTD. Comparison between the SST model and the RNG model is not the main topic here anymore since the inability of the RNG model in the near wall region has been proved by the previous studies.

As shown in Figure 3–13, the heat transfer process has been divided into two stages: the first HTD and heat transfer restoration (left charts), the second HTD and heat transfer restoration (right charts). Three axial positions for each of the charts are plotted to represent the downstream process of the heat transfer. The profiles of specific heat capacity, heat conductivity, density, axial velocity and turbulent kinetic energy along with the radial direction are plotted in Figure 3 – 14.

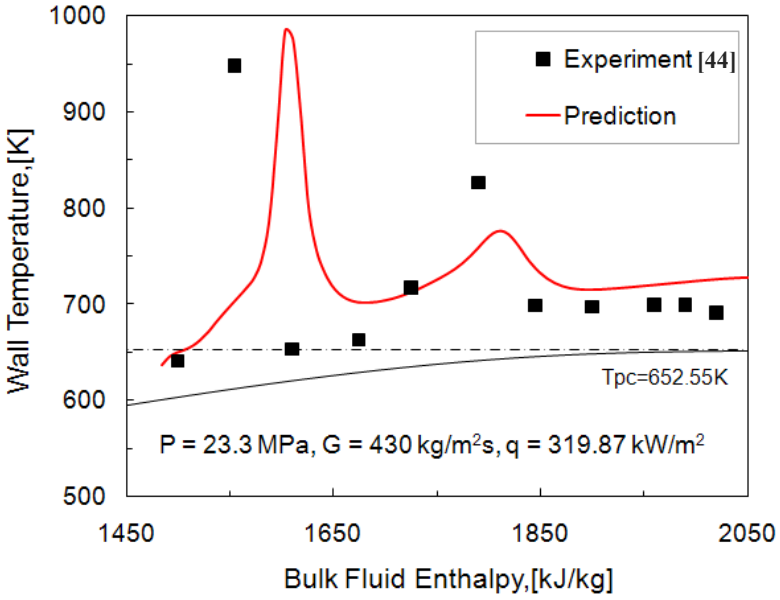

Figure 3–12: Comparison of predictions (SST k-ω turbulence model) and experiments for the case of Shitsman et al. [44]

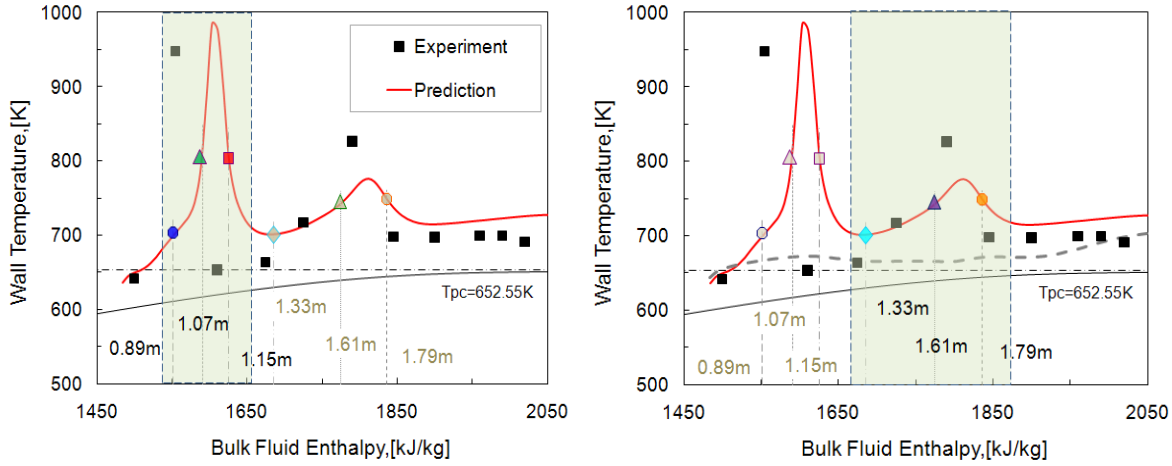

Figure 3–13: Illustration of 6 axial positions in case D1 for analysis in detail.
Left: the first HTD and heat transfer restoration. Right: the second HTD and heat transfer restoration

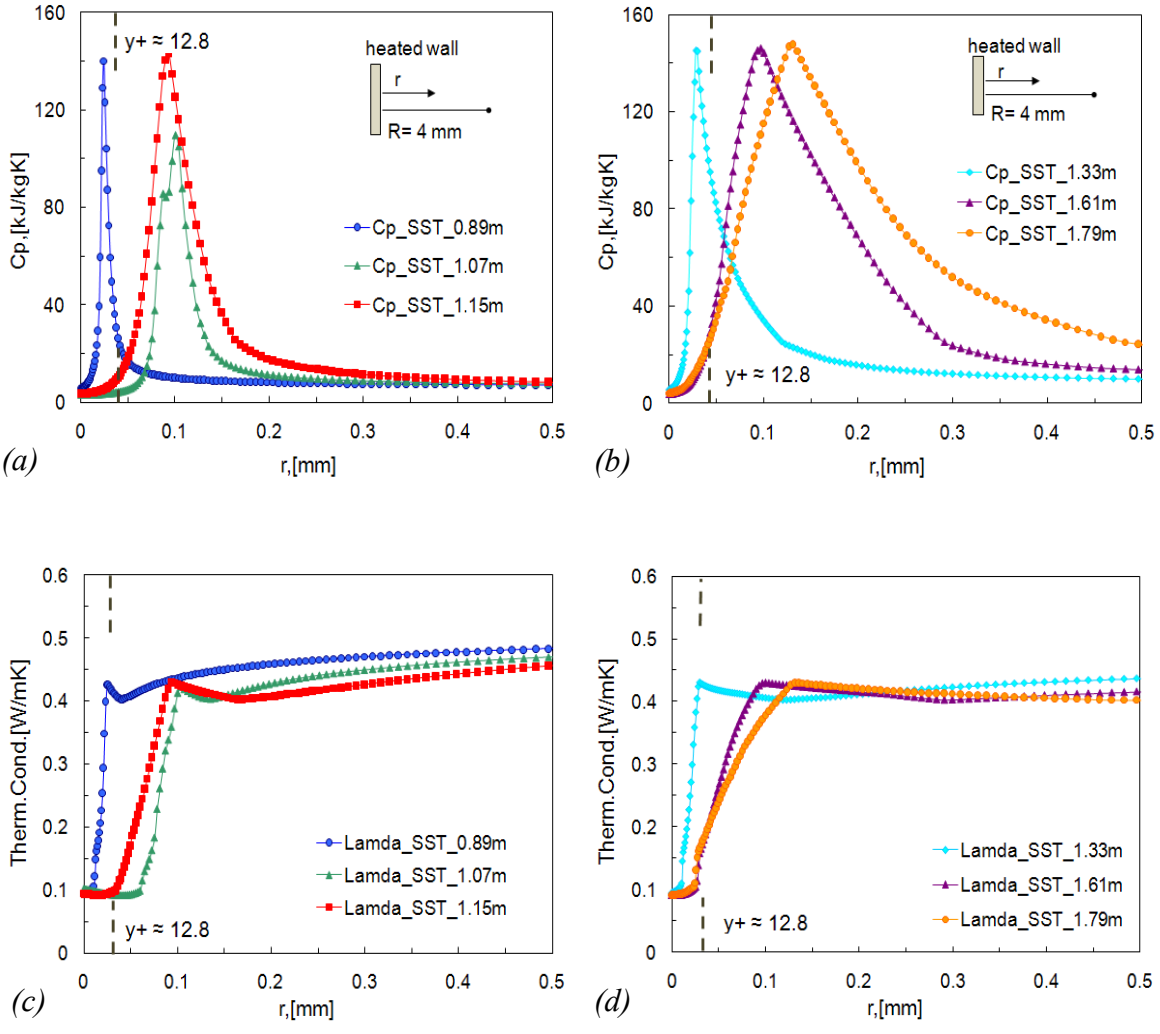

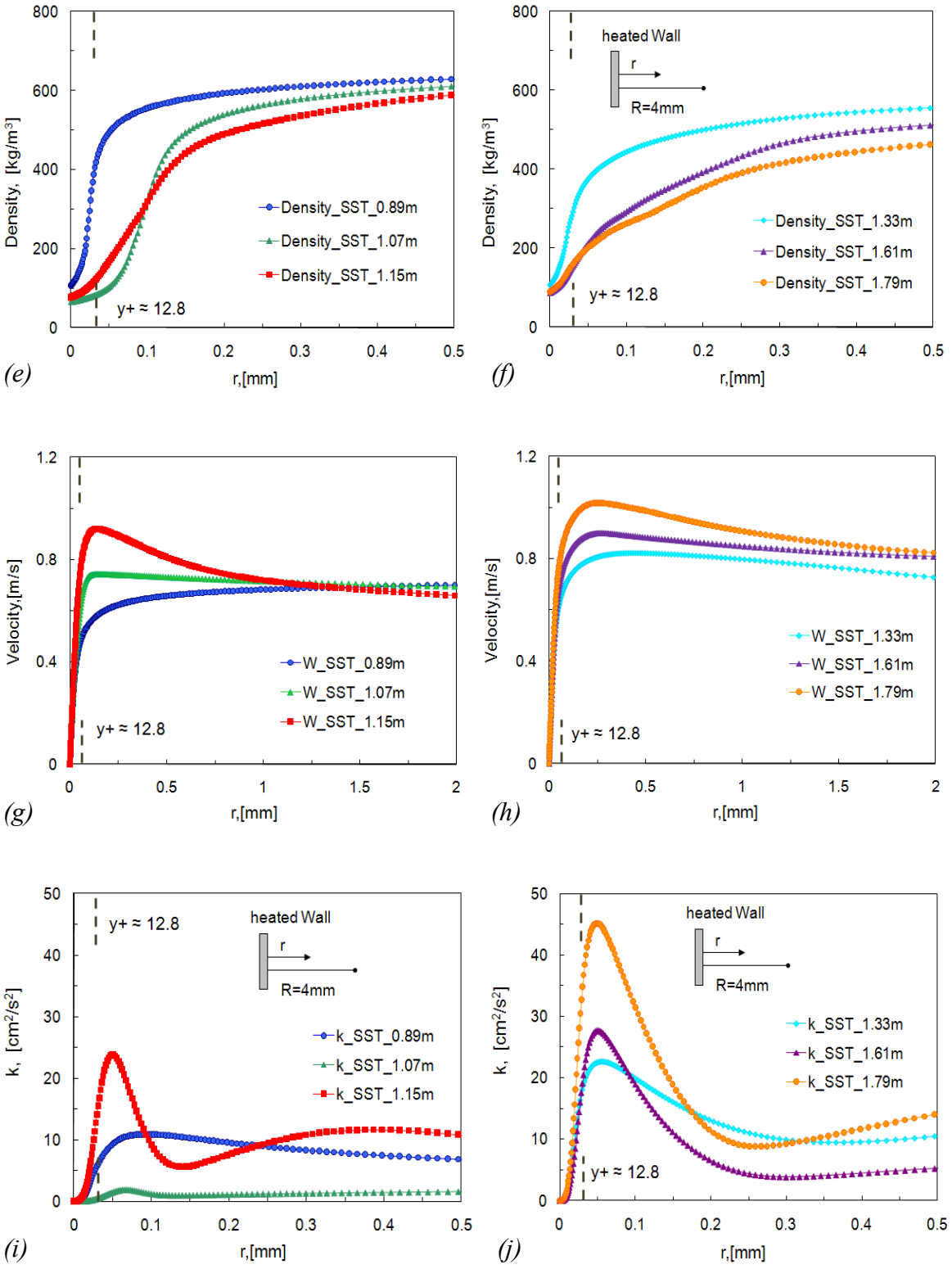

Figure 3 – 14: Radial profiles of thermal-hydraulic properties, turbulent kinetic energy and axial velocity (case D1). Left column: First HTD. Right column: Second HTD

First HTD and heat transfer restoration. As the fluid enters the heated section, the fluid temperature near the wall begins to increase. This increase in temperature is associated with a decrease in density as shown in Figure 3 – 14 (e). Because the near wall density is lower than the density of the fluid in the core, the near wall velocity begins to increase due to the buoyancy forces. This flow acceleration decreases the velocity gradient close the wall and forms a flatter velocity profile as shown in Figure 3 – 14 (g). Considering that the production term in the equation for turbulent kinetic energy (Equation (2-22)) is directly proportional to the velocity gradient, the lack of velocity gradient drastically reduces the diffusion of momentum and heat to the bulk of the flow. The direct consequence is graphically illustrated by the profiles of turbulent kinetic energy in Figure 3 – 14 (i). It can be seen that the highest value of k near the wall decreases from about 10 to less than 2 as the velocity gradient decrease. Therefore the heat transfer is deteriorated and the wall temperature keeps increasing. As the increase of velocity close to the wall continues, the bulk velocity is soon being exceeded, and a reverse gradient of velocity in the near wall region is then formed which shows as a typical "M shape" in the velocity and then is plotted by red dots in Figure 3 – 14 (g). Once the velocity gradient is rebuilt again, the turbulence diffusion is therefore restored and so is the heat transfer.

Second HTD and heat transfer restoration. Enhanced heat transfer due to the first restoration on heat transfer results in a strong decrease in the wall temperature and thus decreases the density difference between the wall and the bulk (light blue rhombus), which leads to the decrease in buoyancy forces and then the velocity close to the wall. Comparing the peak values of velocity at axial positions of 1.15m and 1.33m, there is a difference of 0.2 m/s between each other. Afterwards, the bulk flow starts to accelerate as the bulk temperature is increasing toward the Tpc, which leads to the second decrease of velocity gradient near the wall and then causes the second and milder peak in the wall temperature. As the temperature increases again, the density difference also starts to increase and form an "M shape" of velocity profile again. Consequently, the same mechanism as we mentioned above results in the second heat transfer restoration.

3.1.3 Conclusions for Annular Channel and Pipe Flow

The performance of the SST k-ω turbulence model in predicting heat transfer to water at a supercritical pressure has been assessed by comparing model predictions with four experimental datasets. Performed numerical study shows that the heat transfer to supercritical fluids in a vertical heated pipe can be successfully predicted by the SST model with a proper model configuration, even in the deteriorated region.

Experimental observations reveal two types of the HTD phenomenon: one at a high mass flux density and another at a low mass flux density. In both types of HTD the q/G ratios are greater than 0.7. The computational results here strongly support that the first type of HTD is caused by the integral effect of property variation near the wall region and independent of

the buoyancy effect. Good agreement can be found between the measurement and prediction. At low mass flux densities, buoyancy effect dominates in the near wall region and hence has a strong influence on the heat transfer. The simulation based on the working condition in Shitsman's experiment indicates that the SST model can predict this buoyancy driven HTD accurately.

The disagreement between predictions and experiments occurs only at the cases in which the inlet effect is strong and very hard to be predicted precisely. However, this inlet-affected heat transfer is impossible to occur at the operating conditions in HPLWR because the heated inlet in the core design is far away from the pseudocritical point.

3.2 Bare Rod in a Square Channel

In this section, the numerical investigation for a bare rod in a square channel is presented. The geometry used for the model is a 1/8 section with a length of 1.1 m. The simulations are performed at mass flux densities of 315 kg/m^{2}s and 1000 kg/m^{2}s, heat fluxes of 220 kW/m^2 and 440 kW/m^2. The simulations are carried out with different temperatures at the inlet, which is the same method used in experiments. Based on the result of turbulence model sensitivity study in chapter 2.3.4, ωRSM is used in all simulations. Working conditions are listed as below:

	Pressure, (P)	Mass flux density, (G) kg/m^2s	Heat flux, (q), kW/m^2	Flow direction
E1	25 MPa	1000	220	upward
E2			440	upward
E3		315	220	upward
E4			440	upward

Table 3 – 5: Working condition for a square annular channel in the cases of Licht et al. [65]

Figure 3 – 15 shows the comparisons between predictions and experimental data in charts of the wall temperature versus bulk fluid enthalpy at a high mass flux density of 1000 kg/m^{2}s. In the Figure 3 – 15 (a) the heat transfer tendency shows an enhancement in the vicinity of the T_{pc}. The comparison of experiment tendency in Figure 3 – 15 (a) and (b) indicates that the increase of the heat flux impairs the heat transfer and results in a higher value of the wall temperature. Good agreements can be found between the calculated temperatures and those measured in experiments along with most of the enthalpy region in Figure 3 – 15 (a) and (b). The temperature on the wall is slightly over predicted in the last set of calculation at

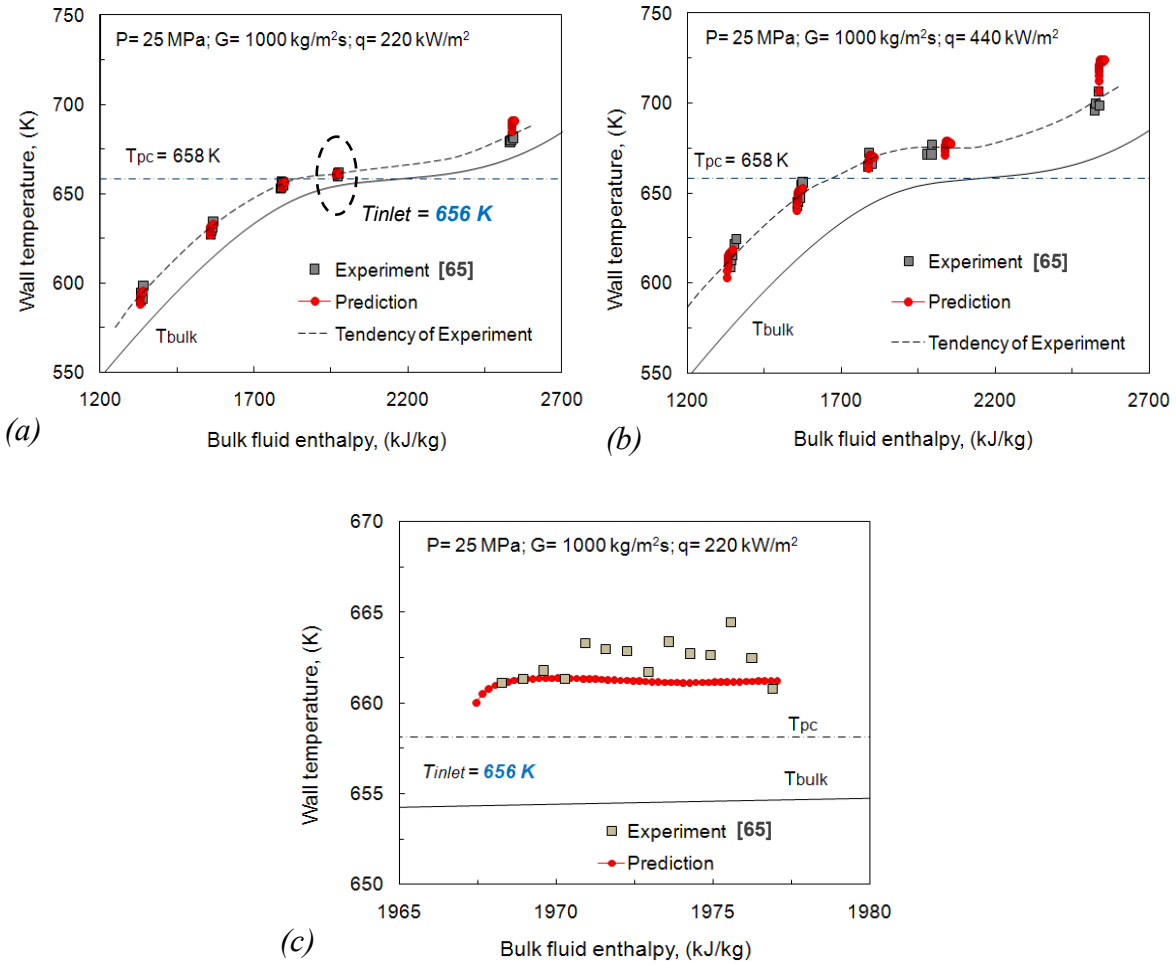

Figure 3 – 15: Comparison of predictions (ωRSM) and experiments at a **high** mass flux density

the bulk enthalpy of about 2530 kJ/kg. This over-prediction becomes more apparent at the higher heat flux (440 kW/m^2).

In each set of the calculations, the enthalpy increase is very small due to the relative low heat flux and high mass flux density. Therefore all the points accumulate together and are very hard to be distinguished individually. Figure 3 – 15 (c) shows one set of calculation with an inlet temperature of 656 K, which has been marked out in Figure 3 – 15 (a). It can be found that the model is not able to predict the small-scale oscillations in the wall temperature. The bulk enthalpy increase here is less than 10 kJ/kg. However, the average value of wall temperatures is still acceptable and the greatest discrepancy with measurement is no more than 5 K.

For a low mass flux density of 315 kg/m^{2}s, the comparison of predictions and experiments is plotted in Figure 3–16 at charts of the wall temperature versus bulk fluid enthalpy. In both of the Figure 3–16 (a) and (b) the experimental data show the HTD of small or big scales in the whole enthalpy region measured in experiments, which is characterized by many local peaks in the wall temperature in each of the sections.

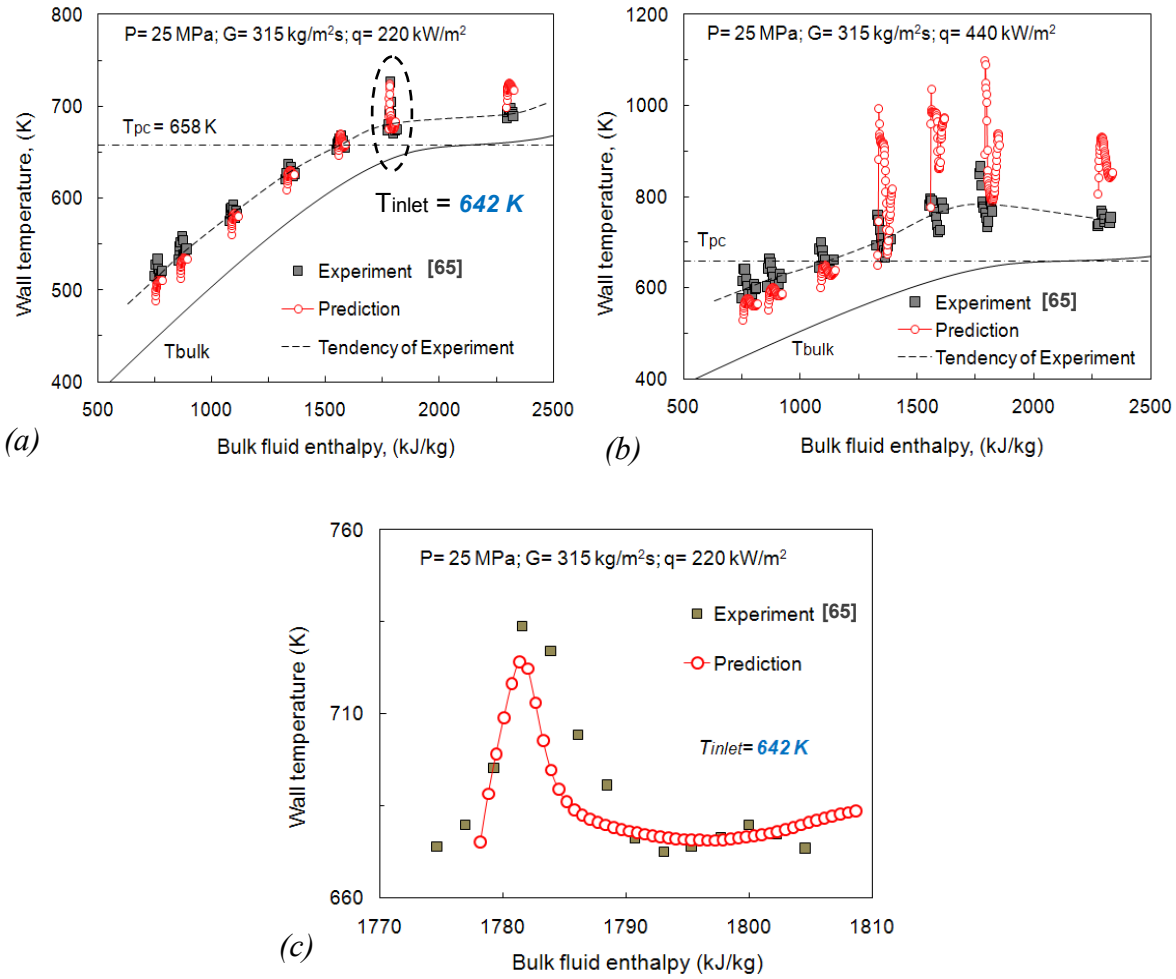

Figure 3–16: Comparison of predictions (ωRSM) and experiments at a **low** mass flux density

At a low heat flux of 220 kW/m^2 (Figure 3–16 a), predictions match experiments well in the whole region of bulk enthalpy only with slight discrepancies in the magnitude. The under-prediction in the wall temperature occurs in the lower bulk enthalpy region (i_b < 1200 kJ/kg), and an over-prediction happens in the higher bulk enthalpy region (i_b > 2250 kJ/kg). Disagreements between predictions and experiments indicate the insufficiency of the current model to a certain extent. In the Figure 3–16 (a), the most severe deterioration, which occurs at a section with the inlet temperature of 642 K, has been marked out. In Figure 3–16 (c), the results of the comparison show an outstanding agreement between predictions and experiments. The profile of the wall temperature is quite similar as that in Shitsman's case which also shows two peaks in the wall temperature. The good agreement here proves again that the model is capable of predicting the buoyancy affected deterioration at a low q/G ratio.

Figure 3–16 (b) shows that both of predictions and experiments exhibit severe deteriorations at a high q/G ratio of 1.4. The prediction reveals the heat transfer recovery after the first temperature peak and also captures the second peak downstream. However, deviations from experiments become larger as the inlet temperature increases, especially in the vicinity of

the pseudocritical temperature. The highest value of the wall temperature in this region is predicted extremely high. The similar phenomena have been observed by the author in other simulations. This kind of over-prediction normally happens when the prescribed temperature at the inlet is very close to T_{pc} and the heat flux is relatively high. It may be due to the strong variation of the properties in the laminar sublayer near the inlet, which cannot be precisely predicted by the current model.

3.3 Rod with Wrapped Wire in a Square Channel

The numerical investigation for a wire-wrapped rod in a square channel is presented in this section. The mesh structure has been illustrated in chapter 2.2.3. The model has a length of 2000 mm with the cladding and wire material taken into account. One revolution of the wrapped wire is 200mm. The cladding material is the stainless steel (1Cr18Ni9Ti) and the wire is ceramic material. The simulations are performed at a mass flux density of 800 kg/m^{2}s, heat fluxes of 400 kW/m^2 and 650 kW/m^2. In order to cover the whole enthalpy region measured in experiments, stepwise calculations are carried out. Based on the result of turbulence model sensitivity study in chapter 2.3.6, SST k-ω turbulence model is used in all simulations. Working conditions in this section are listed as below:

	Pressure, (P)	Mass flux density, (G) *kg/m²s*	Heat flux, (q), *kW/m²*	Flow direction
F1	25 MPa	800	400	upward
F2			650	

Table 3–6: Working condition for a square annular channel in the cases of Li et al. [66]

For a low heat flux of 400 kW/m^2, the calculated mean surface temperatures along with the bulk fluid enthalpy are plotted in Figure 3–17 (a). Predictions and measurements show a good agreement in the wall temperature before the bulk temperature passes beyond the pseudocritical point ($T_w > T_{pc} > T_b$). As the T_b is higher than T_{pc}, the discrepany becomes larger with a 25 K difference. Figure 3–17 (b) shows the comparison in the chart of heat transfer coefficient versus bulk fluid enthalpy. It can be found that the heat transfer coefficient exhibits an enhancement in the vicinity of the pesudocritical point. After its peak, the disagreement of predictions and experiments becomes more obvious. In the high enthalpy region the agreement starts to improve again. The similar trends between predictions and experiments indicate that the current model can predict this complex heat transfer quantitatively and the predicted results are acceptable before the pseudocritical point. However, the discrepancy indicates that the model still needs to be improved.

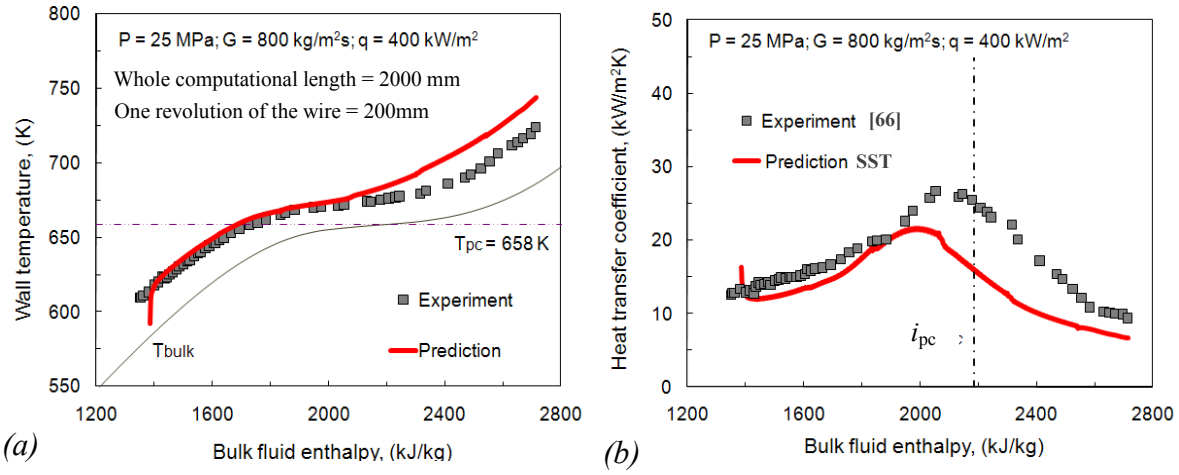

Figure 3–17: Comparison of predictions and experiments at a **low** heat flux of 400 kW/m^2
Left: the wall temperature, Right: heat transfer coefficient

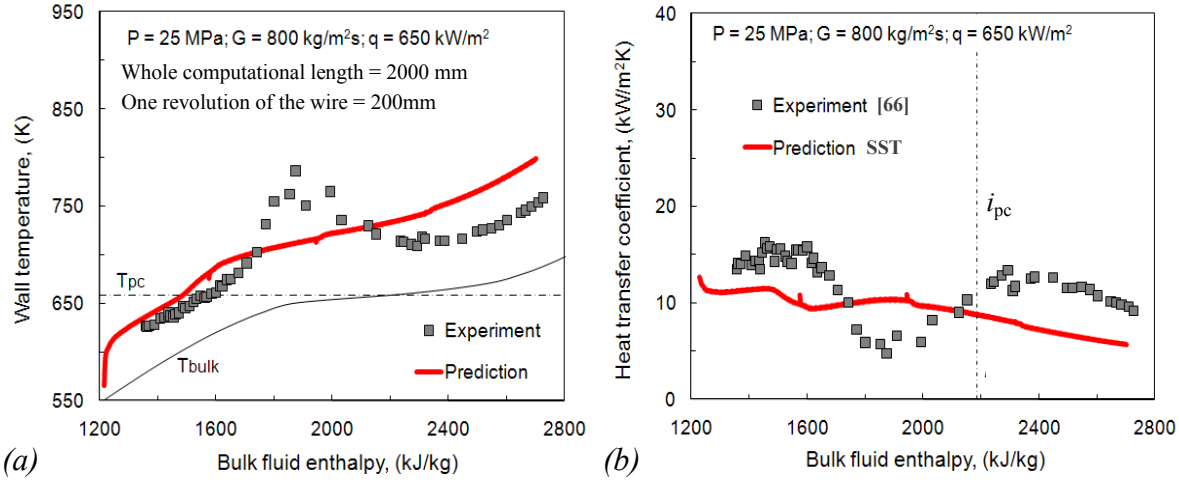

Figure 3–18: Comparison of predictions and experiments at a **high** heat flux of 650 kW/m^2
Left: the wall temperature, Right: heat transfer coefficient

Figure 3–18 shows a deteriorated heat transfer as the heat flux increases to 650 kW/m^2. As shown in the left chart, the numerical model cannot predict the local peak in the wall temperature. However, the prediction gives a rapid increase in the wall temperature when it passes through the pseudocritical point. After the most disagreement area (1800 kJ/kg < i_b < 2100 kJ/kg), the wall temperature predicted by model shows a similar trend as that in experiment. Figure 3–18 (b) illustrates the same tendency of predictions and experiments more apparently. This phenomenon, the wall temperature being over-predicted in the high enthalpy, has been found several times in the simulations with different geometries and working conditions. The consistency reveals the deficiency of the current model in dealing with the heat transfer of supercritical water.

4 Application

As mentioned in the very beginning of this dissertation, one of the important aims in this study is to examine the accuracy of existing turbulence models for a complex flow channel in which the wrapped wire is involved in HPLWR. In the chapter 3, comprehensive studies on the heat transfer behaviour in supercritical water have been performed for different geometries. The mechanisms of both the normal heat transfer and the deteriorated heat transfer have been investigated and then analyzed in detail. Based on those results, the SST k-ω model has been proven that for tubes and square annular channels it has a good ability of predicting the thermal-hydraulic behaviours of the supercritical water not only in mode of the normal heat transfer but also in mode of the deteriorated heat transfer. For a square channel with a wire-wrapped rod inside the SST k-ω model also showed a good performance in mode of the normal heat transfer and qualitatively predicted the deterioration in the case with a higher heat flux. In summary, besides a good, consistent performance for the normal heat transfer, the SST k-ω turbulence model with a proper mesh setup is capable of capturing the onset of HTD not only in the forced convective heat transfer at a high mass flux density, but also in the mixed convective heat transfer dominated by the buoyancy effect. However, the accuracy of the onset prediction is affected considerably by the inlet effect and the wrapped wire.

Since the model has been validated by several experiments, the task in this chapter is to investigate the heat transfer behaviour relevant to the HPLWR design in order to reduce the large uncertainty by using ordinary heat transfer correlations at a supercritical pressure. Additionally, the hotspot analysis for the geometry of a single wire-wrapped rod performed in this chapter reveals the potential highest temperature on the rod surface, which can be used as a reference value for the system safety analysis.

4.1 Geometry Factor and Wire Factor

In the supercritical water cooling channel the thermal-hydraulic behaviour differs significantly from that in a circular tube. Besides the effect coming from the channel shape variation, the wire spacer introduces particular effects on the heat transfer behaviour, which result in the local hotspot and the potential enhanced heat transfer. Therefore the heat

transfer coefficient (h) of supercritical water cannot be predicted by the conventional methods. In order to take into account the effect of square channel and the effect of wire, we propose to introduce two factors into a basic heat transfer correlation (HTC_{basic}) like Jackson's correlation (1-10). The form of the equation could be expressed as below:

$$HTC_{corrected} = F_{geo} \times F_{wire} \times HTC_{basic} \tag{4-1}$$

The value of F_{geo} is determined by a comparison of calculation results between a rod in a square channel and a rod in a circular tube (an annular channel). The value of F_{wire} is calculated by the same approach. It is the ratio of heat transfer coefficients between a wire-wrapped rod (WWR) and a square annular channel.

$$F_{geo} = \frac{h_{(a\ square\ annular\ channel)}}{h_{(an\ annular\ channel)}} \tag{4-2}$$

$$F_{geo} = \frac{h_{(WWR\ inside\ a\ square\ channel)}}{h_{(a\ square\ annular\ channel)}} \tag{4-3}$$

The value of the heat transfer coefficient in an annular channel can be calculated by 2D simulations based on the model validated in chapter 2.3. For the geometries of a square annular channel and a WWR inside a square channel, the same approach is used to derive the corresponding heat transfer coefficients. All the working conditions are coming from the HPLWR design, which are indicated in each of the charts. Finally, both of the geometry factor and the wire factor are derived and the corrected heat transfer correlation ($HTC_{corrected}$) can be implemented into the subchannel code for the safety analysis.

Results and Discussion

In the HPLWR evaporator a nominal sub-channel has a mass flux of 1665 kg/m^{2}s and a heat flux of up to 859 kW/m^2. A hot sub-channel has a mass flux density of 1332 kg/m^{2}s and a heat flux of up to 1375 kW/m^2. Those two working conditions are summarized in Table 4–1, shown as below:

	Mass flux density, (kg/m^2s)	**Heat flux, (kW/m^2)**
Nominal Channel	1665	859
Hot Channel	1332	1375

Table 4–1: Working conditions in HPLWR evaporator

In order to derive the F_{geo} and the F_{wire}, simulations for three geometries with an identical hydraulic diameter and the same working conditions are performed. These three geometries are an annular channel, a square annular channel and a wire-wrapped rod inside a square

channel. Cladding material has been taken into account in the simulations. All the temperatures mentioned here are averaged around the circumference of the cut sections on outer surface of the rod.

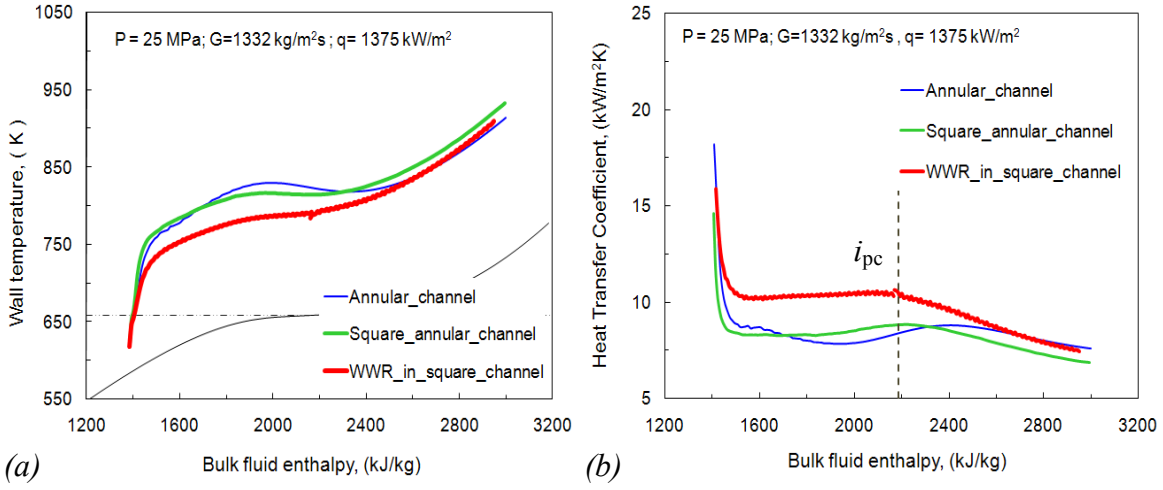

Figure 4–1: Comparison among an annular channel, a square annular channel and WWR inside a square channel at a **Hot-channel** working condition (q/G = 1.03)

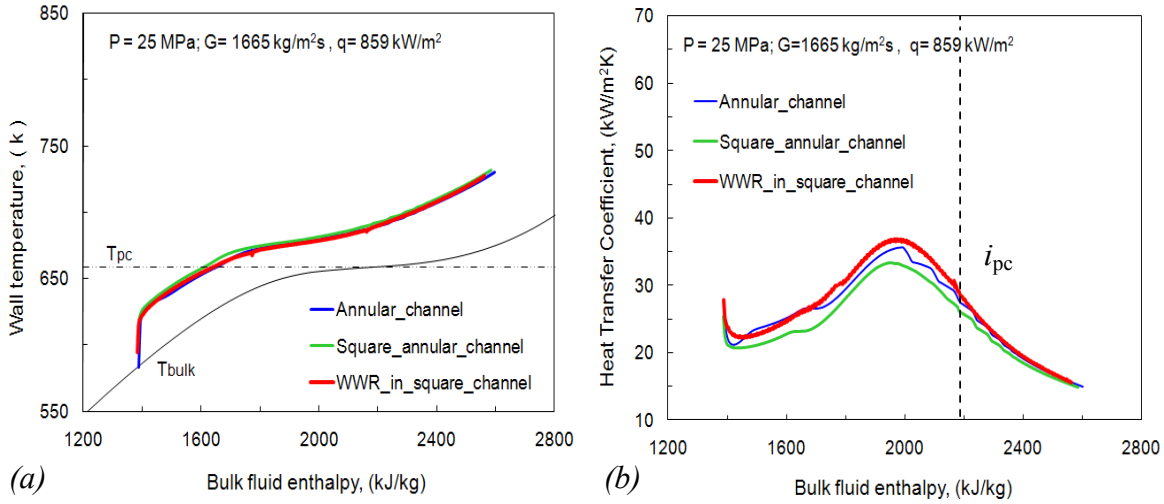

Figure 4–2: Comparison among an annular channel, a square annular channel and WWR inside a square channel at a **Nominal-channel** working condition (q/G = 0.52)

Figure 4–1 shows the comparison at a high q/G ratio of 1.03. The wall temperatures along with the bulk fluid enthalpy are plotted in Figure 4–1 (a) for all three geometries. The temperature profile of annular channel shows a small spike near the bulk enthalpy of 2000 kJ/kg, which is similar as in the square annular channel. In contrast, the wall temperature is reduced by about 50 K in the bulk enthalpy from 1400 kJ/kg to 2200 kJ/kg. As the flow develops downstream, the temperature profiles of three geometries are almost the same. Figure 4–1 (b) shows the comparison in a chart of heat transfer coefficient versus bulk fluid

enthalpy. For WWR inside a square channel, the value of the heat transfer coefficient is 25% larger than those in the square annular channel and the annular channel when the bulk fluid enthalpy is lower than the pseudocritical point ($i_b < i_{pc}$). As the flow passes beyond the i_{pc}, the improvement of the heat transfer induced by the wire becomes less and less. Finally the heat transfer behaviours are nearly independent of the geometry in the high enthalpy region.

In Figure 4–2 (a), the profiles in the wall temperatures are almost the same among three geometries. It is due to the high mass flux density and relatively low heat flux. Normally, the inconspicuous difference becomes easier to be distinguished in the chart of the heat transfer coefficient versus the bulk fluid enthalpy. As shown in Figure 4–2 (b), the heat transfer coefficient in the square annular channel is slightly lower than in the other two geometries. In the high enthalpy region ($i_b > i_{pc}$) even this slight difference has disappeared.

Based on the analysis of HTC for annular channel, square annular channel and WWR in a square channel, the averaged factors are listed in Table 4–2. These values indicate that the improved heat transfer induced by wire will occur at high q/G ratios, in other words, the DHT conditions. At the normal heat transfer conditions, effects induced by the wire and the channel shape are almost negligible. Our conclusions are consistent with those made by the experimentalists who mentioned that the wire spacer performs an essential function by improving the heat transfer in the pseudocritical region and potentially avoids or postpones the occurrence of DHT when the mass flux density is low and the heat flux is relatively high.

	Nominal channel	**Hot channel**
$\mathbf{F_{geo}}$	0.9	0.9 ~ 1.1
$\mathbf{F_{wire}}$	1.1	1.1 ~ 1.3

Table 4–2: Form-factors at the nominal channel and the hot channel conditions

4.2 Analysis of the Local Hotspot

This work aims at further understanding of the flow and heat transfer characteristics which is strongly influenced by the effect of its wire spacer. In particular, the effect of the heat conduction in the cladding plays an important role in the temperature distribution on the rod surface. Hence, this effect has been also investigated here. The flow domain and the geometry of a wire-wrapped rod inside a square channel are already introduced in chapter 2.2.3 and sketched in Figure 2–5 and Figure 2–6. In this section, two geometries are used for different purposes. The first one, WWR I, is the same as in the experiment Li et al. [66]. Predictions based on the WWR I will be later compared with the measurement to test the

heat conduction effect. The second geometry, WWR II, is used to analyze the possible highest temperature in the cladding material under the HPLWR working conditions. Therefore its geometric parameters are corresponding to the HPLWR design. Geometric parameters are listed in Table 4–3.

	D_{rod} (mm)	D_{wire}(mm)	W(mm)	δ (mm)	Reference
WWR I	10	2.2	15	2.5	*Li,* [66]
WWR II	8	1.34	10.88	0.5	*HPLWR*

Table 4–3: Parameters of a wire-wrapped rod inside a square channel

Analysis of the Thermal-hydraulic Behaviours for WWR I (Experiment)

In order to intuitively visualize the flow affected by wire in a square channel, the 3D streamlines have been shown in Figure 4–3 (a). It can be seen that the wire sweeps most part of the water downstream and rest of the water flows straightly across the wire near the corner region of the square channel. The Figure 4–3 (b) shows a nonuniform distribution in the surface temperature. A hotspot region appears apparently on the downwind side of the wire. Since this result is coming from a simulation without the cladding material, the maximum temperature difference here on the rod surface is over 25 K, which can be reduced by the cladding heat conduction in the CHT calculation. The reason responsible for this high temperature region is that the flow swept by wire almost stagnates on the downwind side of the wire and consequently causes the decrease of the energy diffusion in this local region, which therefore increases the surface temperature here.

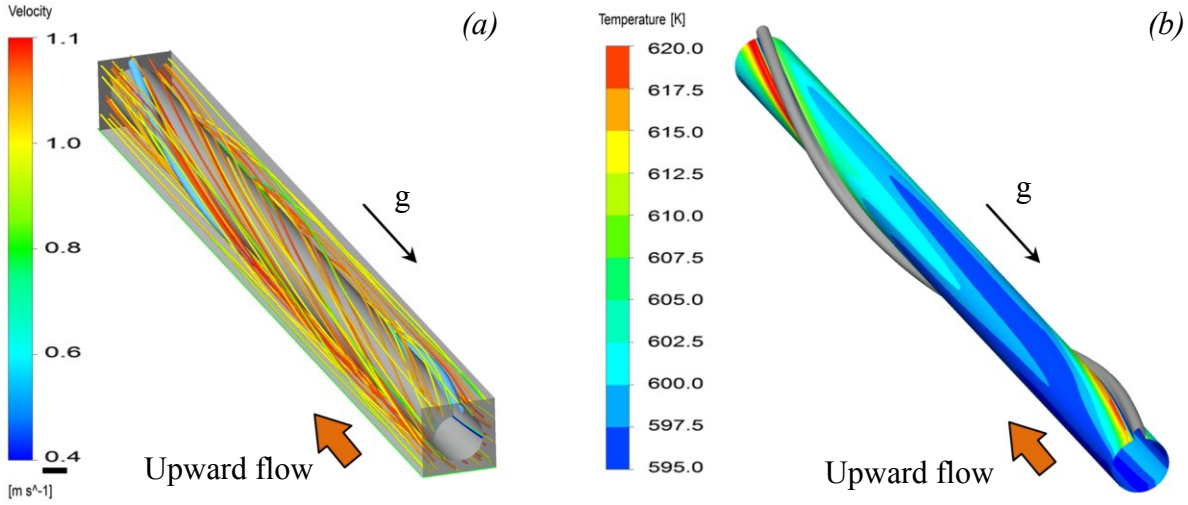

Figure 4–3: Perspective view of 3D streamlines originating from seeding points at the inlet (left) and the temperature distribution on the rod surface (right)

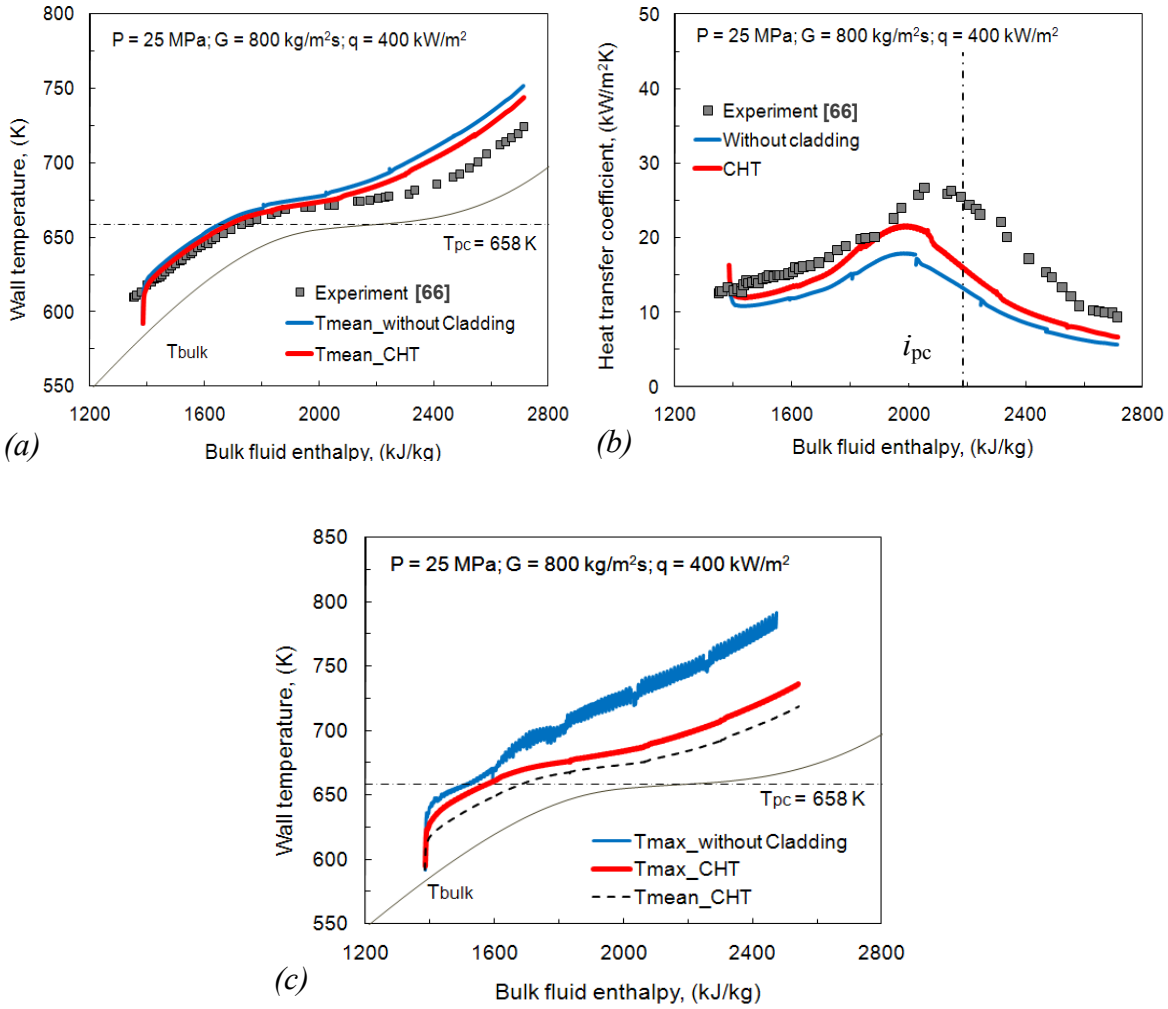

Figure 4–4: Comparison of the simulations with and without cladding at a **low** heat flux: (a): T_{mean} vs. i_b, (b): heat transfer coefficient vs. i_b, (c): T_{max} vs. i_b

In Figure 4–4 (a) the calculated mean surface temperature (T_{mean}) has been compared with the experiment for a low heat flux of 400 kW/m^2. The blue curve corresponds to simulations performed without cladding material. The red curve corresponds to conjugate heat transfer (CHT) simulations with the cladding material included. Before the bulk temperature T_{bulk} reaches T_{pc} the calculated T_{mean} achieves a good agreement with the experiments in the model of CHT. The effect induced by the cladding material slightly decreases the mean surface temperature due to the heat conduction. The results also show similarity with those in a square annular channel, in which the overprediction of the wall temperature occurred in the high enthalpy region. The heat transfer coefficient exhibits an enhancement in heat transfer in the vicinity of the pseudocritical point in Figure 4–4 (b). The effect due to the heat conduction of the cladding material increases the heat transfer coefficient up to 25% near the pseudocritical enthalpy (i_{pc}).

In Figure 4–4 (c) the maximum temperatures along with the bulk fluid enthalpy are plotted. Comparing with the temperature difference in terms of T_{mean}, profiles of the maximum

temperature (T_{max}) show a very large discrepancy between simulations with and without the cladding material. The profile of T_{max} (blue curve) in the case without cladding exhibits a rapid increase as the wall temperature passes beyond the pseudocritical temperature, which is denoted as a "Local Heat Transfer Deterioration (LHTD)" since the profile of T_{mean} illustrates a normal heat transfer trend at same conditions and doesn't have the strong oscillation which occurs in T_{max}. It can be found that the T_{max} difference between simulations with and without cladding is about 50 K, which is much bigger than the difference between T_{max} and T_{mean} in the case with cladding.

Figure 4–5 shows the comparison of simulations with and without cladding material for a high heat flux of 650 kW/m^2. In Figure 4–5 (a), it can be seen that the both of the models with and without cladding are able to predict the increase of the temperature qualitatively with a certain discrepancy in the magnitude. The result of the CHT simulation shows a better agreement with the measurement by predicting a lower T_{mean}. The improvement resulting from the cladding conduction becomes more obvious in the chart of heat transfer coefficient versus bulk fluid enthalpy in Figure 4–5 (b).

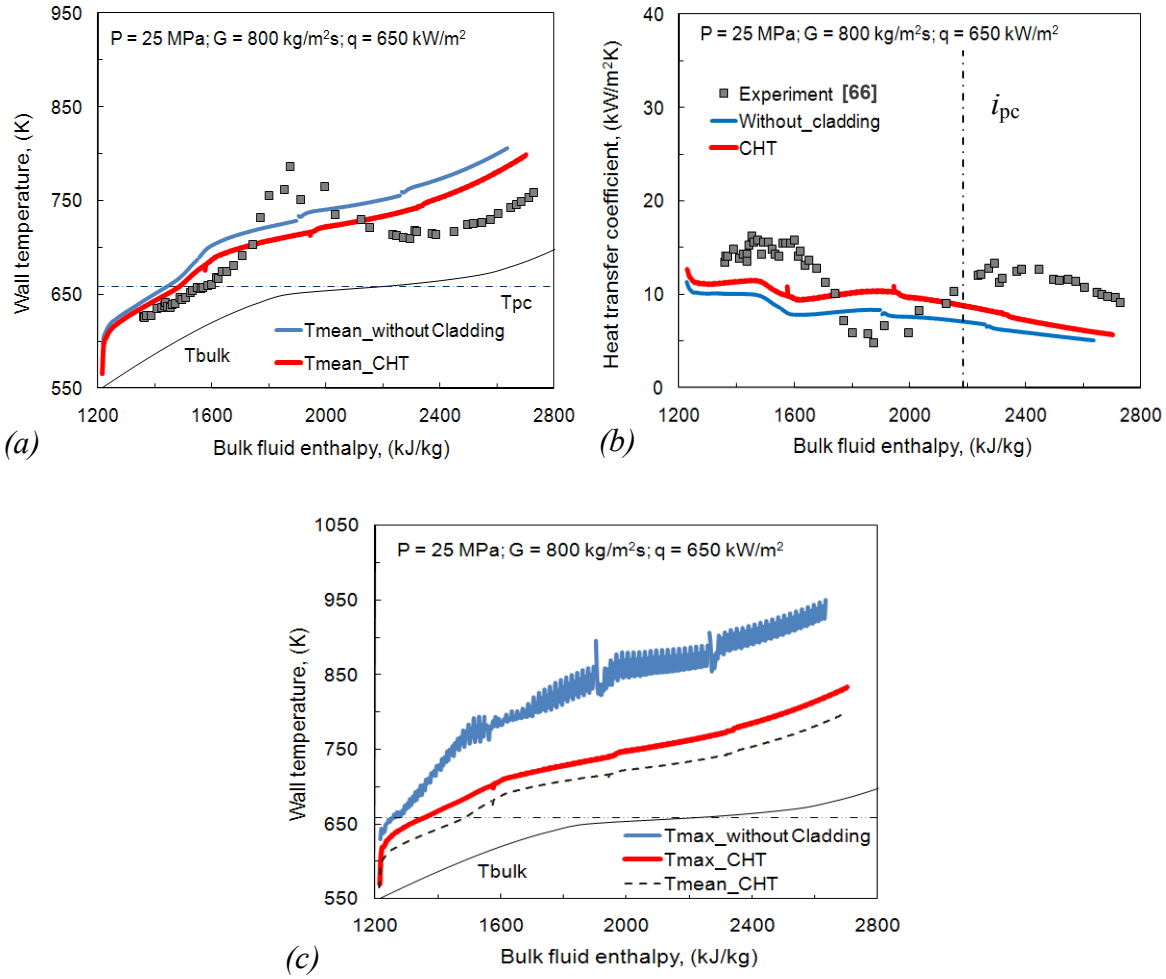

Figure 4–5: Comparison of the simulations with and without cladding at a **high** heat flux: (a): T_{mean} vs. i_b, (b): heat transfer coefficient vs. i_b, (c): T_{max} vs. i_b

In Figure 4–5 (c), the maximum temperatures along with the bulk fluid enthalpy are plotted. Comparing with the temperature difference in terms of T_{mean}, profiles of the maximum temperature (T_{max}) show a very large discrepancy between simulations with and without the cladding material. The temperature oscillation in T_{max} (blue curve) can be greater than 50 K in the high enthalpy region. The discontinuities in the T_{max} profile are due to the imperfect inlet-outlet boundary connection in stepwise calculations. Once the cladding material is taken into account, it can be seen that the T_{max} (red curve) has been dramatically reduced due to the heat conduction. This conduction effect eliminates not only the temperature oscillation but also the LHTD occurring in the low enthalpy region. The temperature difference between simulations with and without cladding is greater than 100 K after the developing region. The temperature difference between the T_{max} and the T_{mean} is also strongly reduced to 15 K in comparison with over 100K in the case without cladding.

Figure 4–6 illustrates the predicted temperature distribution on the rod surface. In the absence of the heat conduction, there are two high-temperature regions on both sides of the wire. The one on the downwind side is more obvious with a higher temperature. On the rod surface, the difference between the lowest and the highest temperature is greater than 85 K in the case without cladding. In the case with cladding, the temperature near the wire has been strongly reduced by the heat conduction. Although the temperature distribution on the surface is still nonuniform, the difference between the lowest and the highest temperature has been remarkably reduced to about 20 K.

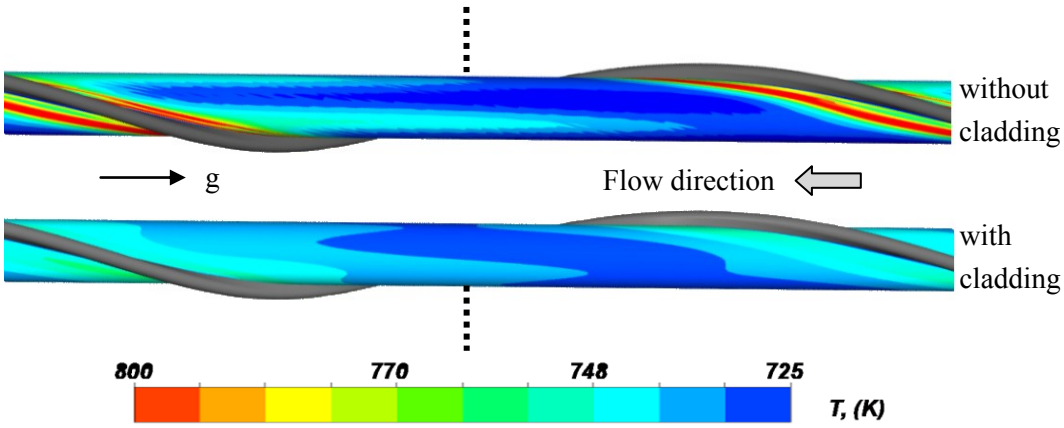

Figure 4–6: Temperature distribution in simulations with and without cladding

In order to further understand the temperature distribution on the rod surface, the surface temperature along with the circumferential position is plotted in Figure 4–7 at an axial cut section, which has been indicated by a black dash-line in Figure 4–6. The horizontal coordinate starts from one side of the wire and goes counter-clockwise along the circumferential direction. In the case without cladding, the surface temperature shows a wavy profile with two apparent peaks on both sides of the wire. The difference between the lowest and highest temperature is 129 K. In the case with cladding (CHT), this difference

becomes 22 K. It can be found that the difference in the mean temperature between simulations with and without cladding is only 15 K, which is much less than the difference in terms of maximum temperature (about 100 K). This phenomenon indicates that the most outstanding effect induced by the heat conduction is the elimination of the temperature peak in hotspot, rather than evident increase of the heat transfer coefficient which is generally calculated by the T_{mean}.

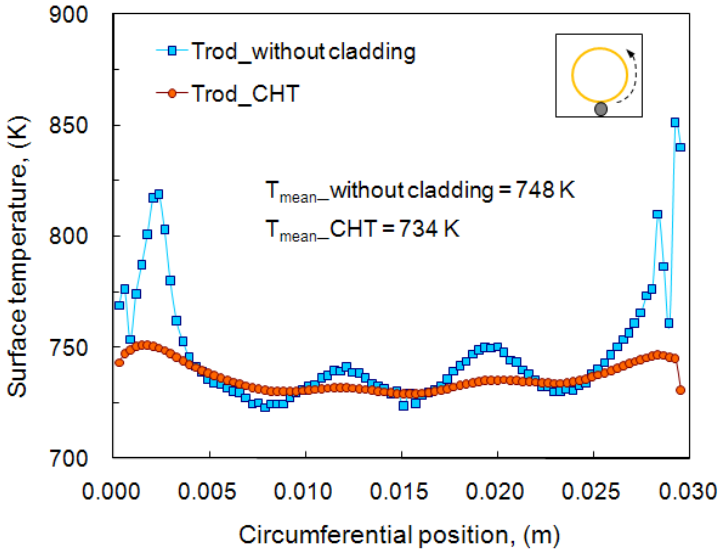

Figure 4–7: Surface temperature versus circumferential position at an axial cut section.

Analysis of the Thermal-hydraulic Behaviours for WWR II (HPLWR)

In the previous chapter, analyses are based on WWR I and the working conditions relevant to the experimental test. In this section, WWR II with a thinner cladding and the working conditions relevant to the HPLWR design are used. As already shown in Table 4–1, a hot sub-channel and a nominal channel working conditions are used in calculations.

Figure 4–8 illustrates the computational results in the charts of temperature versus bulk fluid enthalpy at the nominal and hot channel working conditions, respectively. The cladding material has been taken into account in calculations. The mean surface temperature and the maximum temperature on the outer surface of the rod are plotted in each of charts to illustrate their differences. The total length of the computational domain has been marked corresponding to the relevant increase of the bulk enthalpy. The range of the bulk enthalpy indicates that computational results are comparable with the designed situation in the HPLWR.

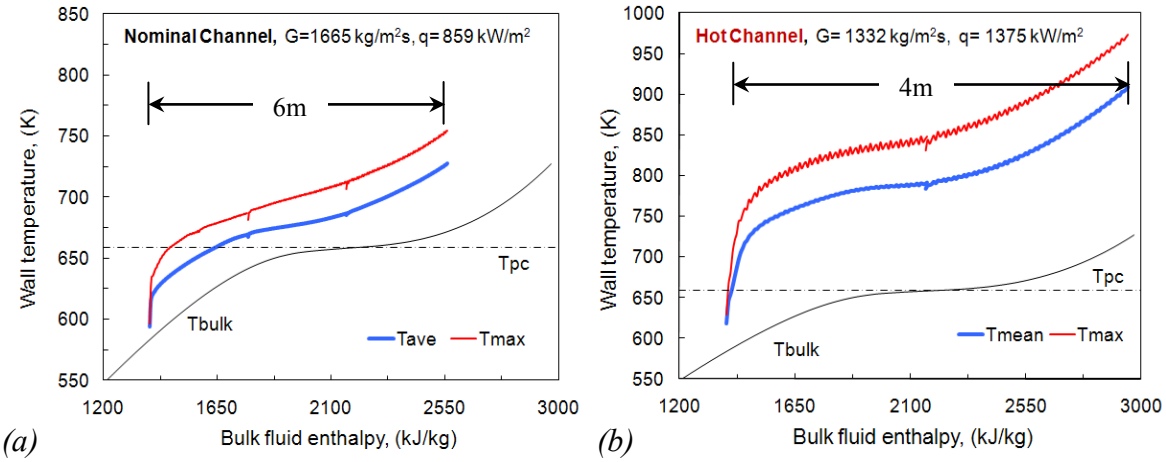

Figure 4–8: CHT simulation results at the nominal and hot channel conditions

Figure 4–8 (a) shows the results at the nominal channel condition. The bulk temperature at the inlet is 583 K and the final bulk temperature at the outlet is 670 K, which is purposely calculated to correspond to the relevant coolant temperatures of 310 ºC at the "evaporator" inlet and 390 ºC at the "evaporator" outlet in the design of HPLWR. As shown in the figure, both of the T_{max} and the T_{mean} are gradually developing downstream without any abrupt increase and keep a constant difference of 25 K between each other. The T_{max} reaches its maximum of 750 K at the bulk enthalpy of 2930 kJ/kg.

The results at the hot channel condition are shown in Figure 4–8 (b). After the developing region, the T_{max} and the T_{mean} increase smoothly. It is different from the results at the nominal channel condition that the T_{max} profile shows a slight oscillation due to interactions between the wire and the inner corners of the square channel. But the scale of this oscillation is much less than that in Figure 4–5 (c) where the amplitude varies in region of over 50 K. The difference between the T_{max} and T_{mean} keeps constant with a value of 60 K in the quasi-fully developed region. Finally, the T_{max} reaches its maximum of 973 K (700 ºC) at the outlet.

Up to now, all the surface temperatures mentioned above are the temperatures on the outer surface of the cladding. Actually, there is also temperature difference existing inside of the cladding material, which can be denoted by the temperature on the outer surface (T_{outer}) and the temperature on the inner surface (T_{inner}). Figure 4–9 illustrates the difference between the T_{outer} and the T_{inner}. In the left diagram it can be found that there are two internal high-temperature regions under the wire and close to the inner surface. This is due to the low heat transfer coefficient on the outer surface corresponding to the hotspot position. Because we use the same material for both of rod and wire spacer, and considering the contact area between the wire and rod is larger than the realistic line-contact, the wire improves the heat transferring from the rod to the coolant and therefore reduces the maximum temperature underneath. In other words, the temperature beneath the wire could be higher than the prediction in realistic conditions.

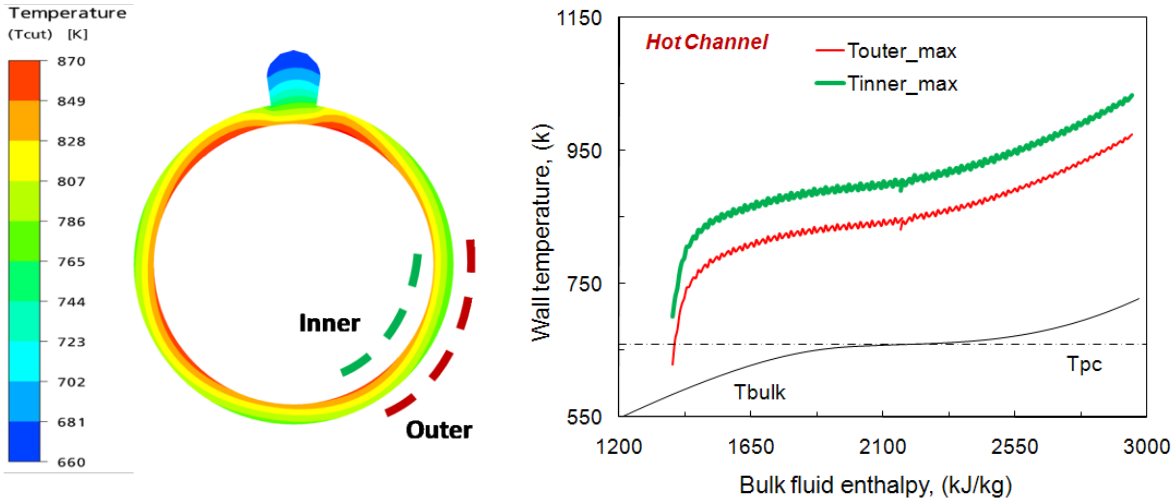

Figure 4–9: Predicted temperature distribution inside the rod (left). The maximum temperature profile on the inner and out surfaces of the rod (right)

The right chart in Figure 4–9 shows the maximum temperatures on the inner and outer surfaces develop along with the bulk fluid enthalpy. The T_{outer_max} denotes the maximum temperature on the outer surface (red curve), which is the same as the T_{max} in Figure 4–8 (b). The T_{inner_max} denotes the maximum temperature on the inner surface (green curve), where the heat flux is imposed in the numerical model. The difference between these two maximum temperatures is about 60 K. It is worth mentioning that the inner temperature reaches 1025 K (750 ºC) at the outlet of the calculation domain. This value is close to the maximum cladding temperature criterion in the transient condition mentioned by Oka and Kushizuka [21].

Conclusions

In this section, the investigation on the temperature hotspot has been carried out as a previous study for the safety analysis. It is found that the most outstanding effect induced by the heat conduction is the elimination of the temperature peak in the hotspots, rather than evident increase of the heat transfer coefficient. However, the conduction effect does not totally remove the hotspot. The temperature difference between the T_{max} and the T_{mean} on the outer surface of the rod can be greater than 60 K at the hot-channel working conditions. Furthermore, the temperature difference inside the cladding material cannot be neglected considering its temperature criterion.

5 Conclusions and Future Work

A series of numerical studies have been performed in order to understand the thermal and hydraulic behaviours in water at a supercritical pressure. Different turbulence models have been tested and validated by experimental data in terms of reproducing the heat transfer under different working conditions and at different geometries. In particular, the ability of capturing the onset of heat transfer deterioration is particularly important for safety analyses in the HPLWR design. Based on the knowledge resulting from the model validation, two form-factors, which aim to improve the accuracy of heat transfer correlations on the complex geometries and under the supercritical conditions, are derived for a further safety analysis by using the sub-channel codes.

Lessons learned on heat transfer behaviours in the supercritical water

Results of 2D simulations demonstrated that under a same mesh structure and the model configuration, the SST k-ω turbulence model has a better capability to predict the heat transfer behaviour of supercritical water upward flowing in vertical annular channels and tubes. It has been shown that the behaviour of the SST k-ω model in case of heat transfer deterioration is more superior to that of the RNG k-ε model. The RNG k-ε model is generally unsuited for this problem. The reason is that the SST model can reproduce the property variation and the turbulence status near the wall much better than the RNG model does. First, the SST k-ω model does not use the wall damping function and inherently avoids the stiff problem in the laminar sublayer. Second, the SST k-ω model accounts for the non-equilibrium between the production of k and its dissipation. On the contrary, the source for the deficiency of RNG k-ε model is thought to be the use of the wall damping function, which yields the ill-predicted properties in the near-wall region. Hence, the SST k-ω turbulence model is recommended by the author for simulations under similar working conditions and geometries which have been tested in this study.

The experimental data on annular channels and tubes show two types of HTD which may occur in an upward flow in supercritical water. The first type of HTD occurs at a high mass flux density, and the second one is induced by the effect of the lateral buoyancy effect at a relative low mass flux density. The simulations illustrate that the SST k-ω model is capable of predicting both of them. For the first type of HTD, the SST k-ω model shows a good performance on capturing the onset of HTD with a slight shift to upstream and also reach a good agreement with experiments before the HTD. For the second type of HTD, the SST

k-ω model gives an outstanding performance to reproduce the strong buoyancy effect along the radial direction, therefore results in a good prediction on this mixed convection heat transfer. However, a special inlet-affected heat transfer cannot be predicted accurately by the SST k-ω model in cases of Yamagata C3 and C4. The model needs more information to reproduce the thermal hydraulic boundary layer near the inlet. Nevertheless, this type of heat transfer is less important in this study since this type of inlet effect will not occur in the first upward heating path in the core of the HPLWR.

After the 2D investigation for the purpose of understanding the heat transfer behaviour and the basic mechanism of HTD, 3D simulations have been performed to investigate the geometric effect and the wire effect which will considerably influence the heat transfer behaviour in the fuel assembly. Simulations on a square annular channel illustrate that ω-based Reynolds Stress Model is capable of precisely predicting both of the forced and mixed convection heat transfer. However, still for the inlet-affect heat transfer, theω-based Reynolds Stress Model predicted higher values in the wall temperature but with a similar tendency in profile.

3D simulations on a square channel with a wire-wrapped rod inside have been performed to study the wrapped wire effect. It can be concluded that the SST k-ω model is suitable for the simulation in the presence of wrapped wire. Using the SST k-ω model requires only half of the computing time and gives a same prediction in comparison with the ω-based Reynolds Stress Model. Our model is capable of giving a reasonable prediction on the normal heat transfer. For the deteriorated heat transfer, the model can only qualitatively predict the abrupt increase of the wall temperature. But the results are still acceptable in most of the enthalpy region out of the HTD. Analysis of the temperature distribution on the rod surface reveals a high-temperature region near the wire. Before the cladding material is taken into the model, the difference between the T_{mean} on the whole surface and the T_{max} on the hotspot can be greater than 130 K. In contrast, this difference becomes 22 K in the case of conjugate heat transfer. It can be therefore concluded that the cladding material has to be taken into consideration in order to precisely predict the maximum temperature on the rod surface.

Contributions to HPLWR

Based on the validated model, the investigation on the temperature hotspot has been carried out as a previous study for the safety analysis in HPLWR. It is found that the most outstanding effect induced by the heat conduction is the elimination of the temperature peak in the hotspots, rather than evident increase of the heat transfer coefficient. However, the conduction effect does not totally remove the hotspot. The temperature difference between the T_{max} and the T_{mean} on the outer surface of the rod can be greater than 60 K at a hot-channel condition. Furthermore, the temperature difference inside the cladding material cannot be neglected considering its temperature criterion.

Additionally, two form-factors for adjustments of the current heat transfer correlation are derived based on the mean surface temperature. The values of the "geometry factor" and the "wire factor" indicate that the wire spacer can improve the heat transfer at DHT conditions. These factors can be implemented into sub-channel codes for safety analysis.

Further work

In chapter 2, we introduced a new statistical model which takes the effect of the turbulent temperature fluctuations on the specific heat capacity into account. It uses an effective heat capacity (or turbulent heat capacity) in the simulation rather than the molecular heat capacity. The results demonstrate the significance of recognizing the difference between $c_p(\bar{T})$ and $\overline{c}_p(\bar{T})$, as well as the potential capability of this pdf-turbulence model improving the prediction on the heat transfer in supercritical water.

However, the improvement occurring in the different enthalpy region indicates that a constant sigma cannot correctly represent the temperature fluctuation in the whole enthalpy region and is therefore inappropriate in an ideal pdf-turbulence model. In the further work, first, an ideal implementation of this model in a CFD code should use the numerically predicted fluctuation level rather than a constant value. Second, a variable turbulent Prandtl number (Pr_t) should be used in the model rather than a constant value. Third, a property-table generator is required so that a table of $\overline{c}_p(\bar{T})$ with different sigma can be implemented into the calculation rather than the current equations.

This pdf-turbulence model needs to be further investigated and validated in details. Data from DNS or experimental data with turbulent quantities measured carefully is also required in the further work.

Bibliography

[1] *Key World Energy Statistics 2007*, International Energy Agency, 2007.

[2] *Nuclear Power Worldwide: Status and Outlook*, International Atomic Energy Agency, 2007.

[3] D. Bittermann, J. Starflinger, and T. Schulenberg, "Turbine Technologies for High Performance Light Water Reactors," *Proceedings of ICAPP '04*, Pittsburgh, PA USA: 2004.

[4] M. Corradini, "Current aspects of LWR containment loads due to severe reactor accidents," *Nuclear Engineering and Design*, vol. 122, Sep. 1990, pp. 287-299.

[5] T. Schulenberg, J. Starflinger, and J. Heinecke, "Three pass core design proposal for a high performance light water reactor," Yokohama, Japan: 2006.

[6] K. Fischer, T. Schulenberg, and E. Laurien, "Design of a supercritical water-cooled reactor with a three-pass core arrangement," *Nuclear Engineering and Design*, vol. 239, Apr. 2009, pp. 800-812.

[7] S. Himmel and A.G. Class, E. Laurien and T. Schulenberg, "CFD analysis of subchannel flow in a HPLWR assembly with wire wraps," *International Student Workshop on HPLWR*, March 31 to April 3, 2008, Karlsruhe, Germany.

[8] W. Wagner and H. Kretzschmar, "IAPWS Industrial Formulation 1997 for the Thermodynamic Properties of Water and Steam," *International Steam Tables*, 2008, pp. 7-150.

[9] S. Mokry, I. Pioro, P. Kirillov, and Y. Gospodinov, "Supercritical-water heat transfer in a vertical bare tube," *Nuclear Engineering and Design*, vol. 240, Mar. 2010, pp. 568-576.

[10] J. Hofmeister, C. Waata, J. Starflinger, T. Schulenberg, and E. Laurien, "Fuel assembly design study for a reactor with supercritical water," *Nuclear Engineering and Design*, vol. 237, Aug. 2007, pp. 1513-1521.

[11] T. Schulenberg and J. Starflinger, "European Research Project on the High Performance Light Water Reactor," *International Students Workshop on HPLWR*, March 31 to April 3, Karlsruhe, Germany, 2008.

[12] Y. Kim, S. Bae, E. Lee, and D. Park, “Sensitivity Study of SCWR Core Design Concepts in Korea,” *Proceedings of The 16th Pacific Basin Nuclear Conference*, Aomori,Japan: 2008.

[13] L. Monti, J. Starflinger, and T. Schulenberg, “Coupled Neutronic / Thermal-Hydraulic Analysis of the HPLWR Three Pass Core,” *The 16th Pacific Basin Nuclear Conference*, Aomori,Japan: 2008.

[14] S. Himmel, A. Class, E. Laurien, and T. Schulenberg, “Sub-channel Analysis of a HPLWR Fuel Assembly with STAR-CD,” *The 16th Pacific Basin Nuclear Conference*, Aomori, Japan: 2008.

[15] S. Penttilä, A. Toivonen, L. Heikinheimo, and R. Novotny, “Corrosion Studies of Candidate Materials for European HPLWR,” *Proceedings of ICAPP '08*, Anaheim, CA, USA: 2008.

[16] M.F. Loewenberg, E. Laurien, A. Class, and T. Schulenberg, “Supercritical water heat transfer in vertical tubes: A look-up table,” *Progress in Nuclear Energy*, vol. 50, 2008, pp. 532-538.

[17] D. Palko and H. Anglart, “Numerical Study of the Influence of Buoyancy and Thermo-Physical Properties Variations on Heat Transfer to Supercritical Water,” *NUTHOS-7*, Seoul, KOREA: 2008.

[18] Y. Zhu and E. Laurien, “Predictions of Heat Transfer of Upward Flow in Annular Channel at Supercritical Pressure - Water and CO2,” *4th International Symposium on Supercritical Water-Cooled Reactors*, Heidelberg, Germany: 2000.

[19] D. Visser, J. Lycklama a Nijeholt, and F. Roelofs, “CFD predictions of heat transfer in super critical flow regime,” *Proceedings of ICAPP '08*, Anaheim, CA, USA: 2008.

[20] Y. Oka and S. Koshizuka, “Design Concept of Once-Through Cycle Supercritical-Pressure Light Water Cooled Reactors,” *Proceedings of International Symposium on Supercritical Water-cooled Reactor Design and Technology*, Tokoy, Japan: 2000.

[21] Y. Oka and S. Koshizuka, “Supercritical-Pressure, Once-Through Cycle Light Water Cooled Reactor Concept,” *J. Nucl. Sci. Technol*, vol. 38, 2001, pp. 1081-1089.

[22] S. Koshizuka, N. Takano, and Y. Oka, “Numerical analysis of deterioration phenomena in heat transfer to supercritical water,” *International Journal of Heat and Mass Transfer*, vol. 38, Nov. 1995, pp. 3077-3084.

[23] T.T. Yi, Y. Ishiwatari, J. Liu, S. Koshizuka, and Y. Oka, "Thermal and stability considerations of super LWR during sliding pressure startup," *Journal of Nuclear Science and Technology*, vol. 42, 2005, pp. 537-548.

[24] K. Kazuhiro, Y. Akifumi, I. Yuki, O. Yoshiaki, and L. Jie, "Fuel and Core Design of Super Light Water Reactor with Low Leakage Fuel Loading Pattern," *J. Nucl. Sci. Technol*, vol. 43, 2006, pp. 129-139.

[25] A. Yamaji, T. Tanabe, and Y. Oka, "Evaluation of the Nominal Peak Cladding Surface Temperature of the Super LWR with Subchannel Analyses," *Proceedings of GLOBAL 2005*, Tsukuba, Japan: 2005.

[26] A. Yamaji, Y. Oka, Y. Ishiwatari, J. Liu, and M. Suzuki, "Principle of rationalizing the criteria for abnormal transients of the Super LWR with fuel rod analyses," *Annals of Nuclear Energy*, vol. 33, Aug. 2006, pp. 984-993.

[27] Y. Ishiwatari, Y. Oka, S. Koshizuka, A. Yamaji, and J. Liu, "Safety of Super LWR, (II) Safety Analysis at Supercritical Pressure," *Journal of Nuclear Science and Technology*, vol. 42, 2005, pp. 935-948.

[28] Y. Ishiwatari, M. Yamakawa, and Y. Oka, "Research and development of a Super Fast Reactor (1) Overview and High-Temperature Structural design," Aomori, Japan: 2008.

[29] X. Cheng, "R&D Activities on SCWR in China," *4th International Symposium on Supercritical Water-Cooled Reactors*, Heidelberg, Germany: 2009.

[30] L. Cao, Y. Ju, Y. Oka, and S. Ikejiri, "Research and Development of a Super Fast Reactor (2) Core Design Improvement on Local Void Reactivity," Aomori, Japan: 2008.

[31] H. Mori, S. Yoshida, S. Morooka, and H. Komita, "Heat Transfer Study under Supercritical Pressure Conditions for Single Rod Test Section," *Proceedings of ICAPP '05*, Seoul, KOREA: 2005.

[32] H. Mori, M. Ohno, K. Ohishi, and Y. Hamamoto, "Research and Development of a Super Fast Reactor (7) Heat Transfer to a Supercritical Pressure Fluid Flowing in a Sub-bundle Channel," Aomori, Japan: 2008.

[33] H. Khartabil, R. Duffey, N. Spinks, and W. Diamond, "The pressure-tube concept of Generation IV supercritical water-cooled reactor (SCWR): Overview and status," *Proceedings of ICAPP '05*, Seoul, KOREA: 2005.

[34] D. Guzonas, J. Wills, T. Do, and J. Michel, "Corrosion of Candidate Materials for Use in a Supercritical CANDU Reactor," Whistler, BC, Canada: 2007.

[35] I.L. Pioro and R.B. Duffey, “Experimental heat transfer in supercritical water flowing inside channels (survey),” *Nuclear Engineering and Design*, vol. 235, Nov. 2005, pp. 2407-2430.

[36] V. Chatoorgoon, M. Shah, and R.B. Duffey, “Linear Predictions of Supercritical Flow Stability in Parallel Channels,” *Proceedings of 3th International Symposium on Supercritical Water-cooled Reactor Design and Technology*, Shanghai, China: 2007.

[37] H. Joo, J. Yoo, and J. Noh, “Conceptual Design for Rectangular Fuel Assembly for Thermal SCWR System,” *Proceedings of GLOBAL 2003*, New Orleans, LA, USA: 2003.

[38] K. Bae, H. Joo, and Y. Bae, “Conceptual Design of a 1400 MWe Supercritical Water Cooled Reactor Core with a Cruciform Type U/Zr Solid Moderator,” *Proceedings of ICAPP '07*, Nice, France: 2007.

[39] Y. Bae and H. Kim, “Convective heat transfer to CO2 at a supercritical pressure flowing vertically upward in tubes and an annular channel,” *Experimental Thermal and Fluid Science*, vol. 33, Jan. 2009, pp. 329-339.

[40] H. Kim, H.Y. Kim, J.H. Song, and Y.Y. Bae, “Heat transfer to supercritical pressure carbon dioxide flowing upward through tubes and a narrow annulus passage,” *Progress in Nuclear Energy*, vol. 50, Mar. , pp. 518-525.

[41] X. Cheng, X.J. Liu, and Y.H. Yang, “A Mixed Core for Supercritical Water-cooled Reactors,” *Nuclear Engineering and Technology*, vol. 40, Feb. 2008, pp. 117-126.

[42] M. Shitsman, “Heat transfer to water, oxygen and carbon dioxide in near critical region (In Russian),” *Thermal Eng.*, vol. 1, 1959, pp. 68-72.

[43] M. Shitsman, “Temperature conditions in tubes at supercritical pressures,” *Thermal Engineering*, vol. 15, 1968, pp. 72-77.

[44] M. Shitsman, “Impairment of the heat transfer at supercritical pressures,” *High Temperatures*, vol. 1, 1963, pp. 267-275.

[45] H. Swenson, J. Carver, and C. Kakarala, “Heat transfer to supercritical water in smooth-bore tubes,” *J. Heat Transfer, Trans. ASME.*, vol. 87, 1965, pp. 477-484.

[46] K. Goldmann, “Heat transfer to supercritical water at 5000 psi flowing at high mass-flow rates through round tubes,” *International Heat Transfer Conference*, University of Colorado, Boulder, CO, USA: 1961, pp. 561-568.

[47] K. Nishikawa and K. Miyabe, “On the boiling-liking phenomena at supercritical pressures.,” *Memoirs of Faculty of Engineering 25*, Kyushu University, Japan: 1965, pp. 1-25.

[48] B. Shiralkar and P. Griffith, “The effect of swirl, inlet conditions, flow direction, and tube diameter on the heat transfer to fluids at supercritical,” *J. Heat Transfer, Trans. ASME.*, vol. 92, Aug. 1970, pp. 465-474.

[49] W. Hall and J. Jackson, “Heat transfer near the critical point,” *Proceeding of the 6th International Heat Transfer Conference*, Toronto, Ontario, Canada: 1978, pp. 377-392.

[50] K. Yamagata, K. Nishikawa, S. Hasegawa, T. Fujii, and S. Yoshida, “Forced convective heat transfer to supercritical water flowing in tubes,” *International Journal of Heat and Mass Transfer*, vol. 15, Dec. 1972, pp. 2575-2593.

[51] A. Bishop, R. Sandberg, and L. Tong, *A review of heat transfer and fluid flow of water in the supercritical region and during "once-through" operation*, Pittsburgh, PA, USA: Westinghouse Electric Corporation, Atomic Power Division, 1962.

[52] A. Bishop, R. Sandberg, and L. Tong, *Forced convection heat transfer to water at near-critical temperatures and super-critical pressures*, Pittsburgh, PA, USA: Westinghouse Electric Corporation, Atomic Power Division, 1964.

[53] E. Krasnoshchekov and V. Protopopov, “Heat transfer at supercritical region in flow of carbon dioxide and water in tubes,” *Thermal Engineering*, vol. 12, 1959, pp. 26-30.

[54] E. Krasnoshchekov and V. Protopopov, “About heat transfer in flow of carbon dioxide and water at supercritical region of state parameters,” *Thermal Engineering*, vol. 10, 1960, p. 94.

[55] E. Krasnoshchekov, V. Protopopov, F. Van, and I. Kuraeva, “Experimental investigation of heat transfer for carbon dioxide in the supercritical region,” *Proceedings of the 2nd All-Soviet Union Conference on Heat and Mass Transfer*, Minsk, BSSR, 1967.

[56] E. Krasnoshchekov, V. Protopopov, I. Parkhovnik, and V. Silin, “Some results of an experimental investigation of heat transfer to carbon dioxide at supercritical pressure and temperature heads of up to 850 ºC,” *High Temperatures*, vol. 9, 1971, pp. 992-995.

[57] A. Ornatskii, L. Glushchenko, and S. Kalachev, “Heat transfer with rising and falling flows of water in tubes of small diameter at supercritical pressures,” *Thermal Engineering*, vol. 18, 1971, pp. 137-141.

[58] A. Ornatskii, L. Glushchenko, and O. Gandzyuk, “An experimental study of heat transfer in externally-heated annuli at supercritical pressures,” *Heat Transfer-Soviet Research*, vol. 4, 1972, pp. 25-29.

[59] L. Glushchenko, S. Kalachev, and O. Gandzyuk, “Determining the conditions of existence of deteriorated heat transfer at supercritical pressures of the medium,” *Thermal Engineering*, vol. 19, 1972, pp. 107-111.

[60] L. Glushchenko and O. Gandzyuk, “Temperature conditions at the wall of an annular channel with internal heating at supercritical pressures,” *High Temperatures*, vol. 10, 1972, pp. 734-738.

[61] P. Kirillov, A. Kolosov, and E. Petrova, *Temperature distribution in turbulent flow of water at supercritical pressures (circular tube)*, Institute of Physics and Power Engineering, 1986.

[62] P. Kirillov, R. Pomet'ko, and A. Smirnov, “Experimental study on heat transfer to supercritical water flowing in vertical tubes,” *Proceedings of GLOBAL 2005*, Tsukuba, Japan: 2005.

[63] P. Kirillov and V. Grabezhnaya, “Heat Transfer at Supercritical Pressures and the Onset of Deterioration,” *Proceeding of ICONE 14*, Miami, Florida, USA: 2006.

[64] I.L. Pioro, P. Kirillov, S. Mokry, and Y. Gospodinov, “Supercritical Water Heat Transfer in a Vertical Bare Tube: Normal, Improved and Deteriorated Regimes,” *Proceedings of ICAPP '08*, Anaheim, CA, USA: 2008.

[65] J. Licht, M. Anderson, and M. Corradini, “Heat Transfer and Fluid Flow Characteristics in Supercritical Pressure Water,” *Journal of Heat Transfer*, vol. 131, 2009, p. 072502.

[66] H. Li, H. Wang, Y. Luo, H. Gu, X. Shi, T. Chen, E. Laurien, and Y. Zhu, “Experimental investigation on heat transfer from a heated rod with a helically wrapped wire inside a square vertical channel to water at supercritical pressures,” *Nuclear Engineering and Design*, vol. 239, Oct. 2009, pp. 2004-2012.

[67] W. Hall and J. Jackson, “Laminarization of a turbulent pipe flow by buoyancy forces,” *ASME Paper No. 69-HT-55*, 1969.

[68] J. Jackson, “Consideration of the heat transfer properties of supercritical pressure water in connection with the cooling of advanced nuclear reactors.,” *Proceedings of the 13th Pacific Basin Nuclear Conference*, Shenzhen City, China: 2002.

[69] J. Fewster and J. Jackson, “Experiments on Supercritical Pressure Convective Heat Transfer Having Relevance to SCWR,” *Proceedings of ICAPP '04*, Pittsburgh, PA, USA: 2004.

[70] H. Kim, Y. Bae, H. Kim, J.H. Song, and B. Cho, “Experimental Investigation on the Heat Transfer Characteristics in a Vertical Upward Flow of Supercritical CO2.,” *Proceedings of ICAPP '06*, Reno, NV. USA: 2006.

[71] Y. Bae and H. Kim, “Convective heat transfer to CO2 at a supercritical pressure flowing vertically upward in tubes and an annular channel,” *Experimental Thermal and Fluid Science*, vol. 33, Jan. 2009, pp. 329-339.

[72] R. Deissler, “Heat transfer and fluid friction for fully developed turbulent flow of air and supercritical water with variable fluid properties,” *Transactions of the ASME*, vol. 76, Jan. 1954, pp. 73-85.

[73] N. Schnurr, V. Sastry, and A. Shapiro, “A numerical analysis of heat transfer to fluids near the thermodynamic critical point including the thermal entrance region,” *Journal of Heat Transfer*, vol. 98, Nov. 1976, pp. 609-615.

[74] R. Bellinghausen and U. Renz, “Pseudocritical heat transfer inside vertical tubes,” *Chemical Engineering and Processing*, vol. 28, 1990, pp. 183-186.

[75] W. Jones and B. Launder, “The calculation of low-Reynolds-number phenomena with a two-equation model of turbulence,” *International Journal of Heat and Mass Transfer*, vol. 16, 1973, pp. 1119-1130.

[76] S. Koshizuka, N. Takano, and Y. Oka, “Numerical analysis of deterioration phenomena in heat transfer to supercritical water,” *International Journal of Heat and Mass Transfer*, vol. 38, Nov. 1995, pp. 3077-3084.

[77] S. He, W. Kim, P. Jiang, and J. Jackson, “Simulation of mixed convection heat transfer to carbon dioxide at supercritical pressure,” *Proceedings of the Institution of Mechanical Engineers, Part C: Journal of Mechanical Engineering Science*, vol. 218, 2004.

[78] S. He, W. Kim, and J. Jackson, “A computational study of convective heat transfer to carbon dioxide at a pressure just above the critical value,” *Applied Thermal Engineering*, vol. 28, Sep. 2008, pp. 1662-1675.

[79] S. He, W. Kim, and J. Bae, “Assessment of performance of turbulence models in predicting supercritical pressure heat transfer in a vertical tube,” *International Journal of Heat and Mass Transfer*, vol. 51, Sep. 2008, pp. 4659-4675.

[80] J.H. Bae, J.Y. Yoo, and H. Choi, "Direct numerical simulation of turbulent supercritical flows with heat transfer," *Physics of Fluids*, vol. 17, Oct. 2005, pp. 105104-24.

[81] K. Seo, "Studies of Supercritical Heat Transfer and Flow Phenomena," *Proceedings of NURETH-11*, Avignon, France: 2005.

[82] B.E. Launder and D.B. Spalding, "The numerical computation of turbulent flows," *Comput. Methods Appl. Mech. Eng.*, 1974, pp. 269-289.

[83] S. Kim, Y. Kim, Y. Bae, and B. Cho, "Numerical simulation of the vertical upward flow of water in a heated tube at supercritical system pressure," *Proceedings of ICAPP '04*, Pittsburgh, PA, USA: 2004.

[84] F.R. Menter, "Two-equation eddy-viscosity turbulence models for engineering applications," *AIAA Journal*, vol. 32, 1994, pp. 1598-1605.

[85] V. Yakhot, S.A. Orszag, S. Thangam, T.B. Gatski, and C.G. Speziale, "Development of turbulence models for shear flows by a double expansion technique," *Physics of Fluids A: Fluid Dynamics*, vol. 4, 1992, p. 1510.

[86] F. Roelofs and E. Komen, "CFD Analyses of Heat Transfer to Supercritical Water Flowing Vertically Upward in a Tube," *Jahrestagung Kerntechnik 2005*, Nuremberg: 2005.

[87] X. Cheng, E. Laurien, and Y.H. Yang, "CFD Analysis of Heat Transfer in Supercritical Water in Different Flow Channels," *Proceeding of GLOBAL*, Tsukuba, Japan: 2005.

[88] C.G. Speziale, S. Sarkar, and T.B. Gatski, "Modelling the pressure–strain correlation of turbulence: an invariant dynamical systems approach," *Journal of Fluid Mechanics*, vol. 227, 2006, p. 245.

[89] J. Yang, Y. Oka, Y. Ishiwatari, J. Liu, and J. Yoo, "Numerical investigation of heat transfer in upward flows of supercritical water in circular tubes and tight fuel rod bundles," *Nuclear Engineering and Design*, vol. 237, Feb. 2007, pp. 420-430.

[90] S. Hassid and M. Poreh, "A turbulent energy dissipation model for flows with drag reduction," *Journal of Fluids Engineering*, vol. 100, Mar. 1978, pp. 107-112.

[91] D. Palko and H. Anglart, "Theoretical and Numerical Study of Heat Transfer Deterioration in HPLWR," *International Conference: Nuclear Energy for New Europe* , Slovenia: 2007.

[92] D. Palko and H. Anglart, "Numerical Study of Heat Transfer deterioration," *International Students Workshop on HPLWR*, March 31 to April 3, Karlsruhe, Germany, 2008.

[93] D. Visser, J. Lycklama a Nijeholt, and F. Roelofs, "CFD predictions of heat transfer in the super critical flow regime," *Proceedings of ICAPP '08*, Anaheim, CA, USA: 2008.

[94] L. Chandra, J. Lycklama a Nijeholt, D. Visser, and F. Roelofs, "CFD Analyses on the Influence of Wire Wrap Spacers on Heat Transfer at Supercritical Conditions," *Proceedings of 4th International Symposium on Supercritical Water-Cooled Reactors*, Heidelberg, Germany: 2009.

[95] E. Laurien, M. Rashid, and D.M. McEligot, "Heat Capacity Model for Turbulent Heat Transfer at Supercritical Pressure," *ICMF 2007*, Leipzig, Germany: 2007.

[96] E. Laurien and M. Rashid, "Prediction of Overheated Zones along the Wall of Strongly Heated Quasi-Fully Developed Pipe Flow at Supercritical Pressure," *Proceedings of ICAPP '08*, Anaheim, CA, USA: 2008.

[97] J.H. Bae, J.Y. Yoo, and D.M. McEligot, "Direct numerical simulation of heated CO2 flows at supercritical pressure in a vertical annulus at Re = 8900," *Physics of Fluids*, vol. 20, 2008, p. 055108.

[98] E. Laurien and T. Wintterle, "Secondary flows in the Cooling Channels of the High-Performance Light-Water Reactor," *Proceedings of ICAPP '07*, Nice, France: 2007.

[99] A. Kiss, E. Laurien, and A. Aszodi, "Numerical Simulation of a HPLWR Fuel Assembly Flow with Wrapped Wire Spacers," *Proceedings of ICAPP '08*, Anaheim, CA, USA: 2008.

[100] A. Kiss, E. Laurien, A. Aszodi, and Y. Zhu, "Improved Numerical Simulation of a HPLWR Fuel Assembly with Wrapped Wire Spacers," *Proceedings of 4th International Symposium on Supercritical Water-Cooled Reactors*, Heidelberg, Germany: 2009.

[101] S. Himmel, A. Class, E. Laurien, and T. Schulenberg, "Determination of Mixing Coefficients in a Wire-Wrapped HPLWR Fuel Assembly using CFD," *Proceedings of ICAPP '08*, Anaheim, CA, USA: 2008.

[102] S. Himmel, A. Class, E. Laurien, and T. Schulenberg, "Sub-channel Analysis of a HPLWR Fuel Assembly with STAR-CD," *Proceedings of 16PBNC*, Aomori, Japan: 2008.

[103] H. Anglart, “Heat Transfer Deterioration in Application to HPLWR-Mechanisms Identification and Ranking Table,” *Proceedings of 4th International Symposium on Supercritical Water-Cooled Reactors*, Heidelberg, Germany: 2009.

[104] B.E. Launder and B.I. Sharma, “Application of the energy-dissipation model of turbulence to the calculation of flow near a spinning disc,” *Letters in Heat and Mass Transfer*, vol. 1, Dec. 1974, pp. 131-137.

[105] W. Rodi, *Turbulence models and their application in hydraulics: a state-of-the art review*, Taylor & Francis, 1993.

[106] D.C. Wilcox, “Multiscale model for turbulent flows,” *AIAA Journal*, vol. 26, 1988, pp. 1311-1320.

[107] D.C. Wilcox, “Comparison of Two-Equation Turbulence Models for Boundary Layers with Pressure Gradient,” *AIAA Journal*, vol. 26, 1988, pp. 1299-1310.

[108] P.G. Huang, P. Bradshaw, and T.J. Coakley, “Assessment of closure coefficients for compressible-flow turbulence models,” *NASA TM-103882*, March, 1992.

[109] F.R. Menter, “Influence of the freestream values on k-omega turbulence model predictions,” *AIAA Journal*, vol. 30, 1992, pp. 1657-1659.

[110] I.L. Pioro and R.B. Duffey, *Heat Transfer and Hydraulic Resistance at Supercritical Pressures in Power Engineering Applications*, American Society of Mechanical Engineers, 2007.

[111] L. Chandra, F. Roelofs, M. Houkema, and B. Jonker, “A stepwise development and validation of a RANS based CFD modelling approach for the hydraulic and thermal-hydraulic analyses of liquid metal flow in a fuel assembly,” *Nuclear Engineering and Design*, vol. 239, Oct. 2009, pp. 1988-2003.

[112] M. Casey and T. Wintergerste, *ERCOFTAC Special Interest Group on "Quality and Trust in Industrial CFD" - Best Practic Guidelines*, Fluid Dynamics Laboratory, 2000.

[113] J. Jackson and W. Hall, “Forced convection heat transfer to fluids at supercritical pressure,” *Turbulent Forced Convection in Channels and Bundles*, New York, NY, USA: Hemisphere Publishing Corp., , pp. 563-612.

[114] D.C. Wilcox, *Turbulence Modeling for CFD*, Dcw Industries, Incorporated, 1998.

Appendix

A.1 The SST *k-ω* Turbulence Model

The SST k-ω turbulence model is developed by Menter [84] in order to avoid the strong freestream sensitivity in the standard k-ω model and account for the non-equilibrium between the production of *k* and its dissipation. The model utilizes the original k-ω model in the sub and log-layer and gradually switches to the standard k-ε model in the outer region of the boundary layer. The transport equations for the turbulent kinetic energy and the specific dissipation of turbulence are defined as below [84]:

$$\frac{\partial \rho \boldsymbol{k}}{\partial t} + \frac{\partial}{\partial x_j}\left(\rho u_j \boldsymbol{k}\right) = \frac{\partial}{\partial x_j}\left[\left(\mu + \sigma_k \mu_t\right)\frac{\partial \boldsymbol{k}}{\partial x_j}\right] + \mu_t \frac{\partial \overline{u}_i}{\partial x_j}\left(\frac{\partial \overline{u}_i}{\partial x_j} + \frac{\partial \overline{u}_j}{\partial x_i}\right) - \beta^* \rho \boldsymbol{k}\boldsymbol{\omega} \qquad \text{(A.1-1)}$$

$$\frac{\partial \rho \boldsymbol{\omega}}{\partial t} + \frac{\partial}{\partial x_j}\left(\rho u_j \boldsymbol{\omega}\right) = \frac{\partial}{\partial x_j}\left[\left(\mu + \sigma_\omega \mu_t\right)\frac{\partial \boldsymbol{\omega}}{\partial x_j}\right] + \gamma \frac{\boldsymbol{\omega}}{\boldsymbol{k}} \mu_t \frac{\partial \overline{u}_i}{\partial x_j}\left(\frac{\partial \overline{u}_i}{\partial x_j} + \frac{\partial \overline{u}_j}{\partial x_i}\right) - \beta \rho \boldsymbol{\omega}^2$$

$$+2(1 - F_1)\rho \sigma_{\omega 2} \frac{1}{\boldsymbol{\omega}} \frac{\partial \boldsymbol{k}}{\partial x_j} \frac{\partial \boldsymbol{\omega}}{\partial x_j} \qquad \text{(A.1-2)}$$

The terms on the right-hand side of Equation (A.1-2) represent conservative diffusion, eddy viscosity production and dissipation, respectively. The last term describes the cross diffusion. The constants ϕ of this model are calculated from the constants sets ϕ_1 and ϕ_2, which represent a set of constants in the standard k-ω model and the standard k-ε model respectively, shown as follows :

$$\phi = F_1 \phi_1 + (1 - F_1)\phi_2 \qquad \text{(A.1-3)}$$

The constants of set 1 (ϕ_1) in ***k-ω*** model are:

α_{k1}	β_1^*	β_1	$\sigma_{\omega 1}$	κ_1	γ_1
0.85	0.09	0.075	0.5	0.41	$\beta_1/\beta^* - \sigma_{\omega 1}\kappa^2/\beta^{*0.5}$

The constants of set 2 (ϕ_2) in ***k-ε*** model are:

α_{k2}	β_2^*	β_2	$\sigma_{\omega 2}$	κ_2	γ_2
1.0	0.09	0.0828	0.856	0.41	$\beta_2/\beta^* - \sigma_{\omega 2}\kappa^2/\beta^{*0.5}$

The function F_1 in Equation (A.1-2) blends the model coefficients of the ***k-ω*** model in boundary layers with the transformed ***k-ε*** model in free-shear layers and freestream zones. It is defined as:

$$F_1 = \tanh(arg_1^4) \tag{A.1-5}$$

$$arg_1 = min\left[max\left(\frac{\sqrt{k}}{0.09\omega y}; \frac{500\mu}{\rho\omega y^2}\right); \frac{4\rho\sigma_{\omega 2}k}{CD_{k\omega}y^2}\right] \tag{A.1-4}$$

where y is the distance to the nearest surface and $CD_{k\omega}$ is the positive portion of the cross-diffusion term in Equation (A.1-2):

$$CD_{k\omega} = max\left(2\rho\sigma_{\omega 2}\frac{1}{\omega}\frac{\partial k}{\partial x_j}\frac{\partial \omega}{\partial x_j}; 10^{-20}\right) \tag{A.1-6}$$

The eddy viscosity is defined as:

$$\mu_t = \frac{\rho\alpha_1 k}{max(\alpha_1\omega;\ \Omega F_2)} \tag{A.1-7}$$

where the Ω ($\Omega = \partial u_i/\partial x_j$) is the strain rate. This definition of the eddy viscosity guarantees that in the boundary layer of supercritical channel flows, where the equilibrium between the production of k and its dissipation ω is no more invariant due to the strong property variation and buoyancy effect, Bradshaw's assumption, i.e., $\tau = \alpha_1\rho k$ (shear stress is proportional to turbulent kinetic energy) is satisfied. The modification accounts for the transport of the turbulence shear stress in order to improve the accuracy of prediction of flows with a strong non-equilibrium between the production of k and its dissipation. This non-equilibrium can be caused by the adverse pressure gradient and also by the dramatic variation of properties in the laminar sublayer in channel flows under a supercritical pressure.

The auxiliary function F_2 in Equation (A.1-7) is given by:

$$F_2 = tanh(arg_2^2) \tag{A.1-8}$$

$$arg_2 = max\left(\frac{2\sqrt{k}}{0.09\omega y}; \frac{500\mu}{\rho\omega y^2}\right) \tag{A.1-9}$$

A.2 The SSG RSM and ω-based RSM

SSG Reynolds stress model:

The SSG Reynolds stress model [88] is a well validated model that has been used to model swirling flows in the past. Considering the flow pattern in the WWR case, the SSG model is therefore chosen as one of the candidate models.

Reynolds-Stress Tensor:

$$\frac{\partial \bar{\rho}\boldsymbol{\tau_{ij}}}{\partial t} + \frac{\partial}{\partial x_k}\left(\rho\tilde{u}_k\boldsymbol{\tau_{ij}}\right) = -\bar{\rho}P_{ij} - \bar{\rho}\Pi_{ij} + \frac{\partial}{\partial x_k}\left[\left(\mu + \frac{2}{3}c_s\bar{\rho}\frac{k^2}{\varepsilon}\right)\frac{\partial \boldsymbol{\tau_{ij}}}{\partial x_k}\right] + \frac{2}{3}\delta_{ij}\bar{\rho}\varepsilon \tag{A.2-1}$$

Dissipation Rate:

$$\frac{\partial \bar{\rho}\boldsymbol{\varepsilon}}{\partial t} + \frac{\partial}{\partial x_k}(\bar{\rho}\tilde{u}_k\boldsymbol{\varepsilon}) = C_\epsilon\frac{\partial}{\partial x_k}\left[\left(\mu + \sigma_\varepsilon\bar{\rho}\frac{k^2}{\boldsymbol{\varepsilon}}\right)\frac{\partial \boldsymbol{\varepsilon}}{\partial x_k}\right] + C_{\epsilon 1}\bar{\rho}\frac{\boldsymbol{\varepsilon}}{k}\tau_{ij}\frac{\partial \overline{u}_k}{\partial x_k} - \bar{\rho}C_{\epsilon 2}\frac{\boldsymbol{\varepsilon}^2}{k} \tag{A.2-2}$$

where the P_{ij} is the exact Reynolds stress production term, and Π_{ij} is the pressure strain. These terms are modelled as follows [114]:

$$\Pi_{ij} = -(C_1\varepsilon + C_1^*P)b_{ij} + C_2\varepsilon\left(b_{ik}b_{kj} - \frac{1}{3}b_{mn}b_{nm}\delta_{ij}\right) + \left(C_3 - C_3^*\sqrt{b_{ij}b_{ij}}\right)kS_{ij}$$

$$+C_4k\left(b_{ik}S_{jk} + b_{jk}S_{ik} - \frac{2}{3}b_{mn}S_{mn}\delta_{ij}\right) + C_5k(b_{ik}\Omega_{jk} + b_{jk}\Omega_{ik}) \tag{A.2-3}$$

$$P_{ij} = \tau_{im}\frac{\partial \overline{u}_j}{\partial x_m} + \tau_{jm}\frac{\partial \overline{u}_i}{\partial x_m} \quad , \quad P = \frac{1}{2}P_{kk} \tag{A.2-4}$$

in the formulation (A.2-3), b_{ij} is the anisotropy tensor, S_{ij} is the strain rate and Ω_{ij} is the vorticity. Their expression and the constants in the formulation are shown below:

$$b_{ij} = \frac{\tau_{ij}}{k} - \frac{2}{3}\delta, \quad S_{ij} = \frac{1}{2}\left(\frac{\partial \overline{u}_i}{\partial x_j} + \frac{\partial \overline{u}_j}{\partial x_i}\right), \quad \Omega_{ij} = \frac{1}{2}\left(\frac{\partial \overline{u}_i}{\partial x_j} - \frac{\partial \overline{u}_j}{\partial x_i}\right) \tag{A.2-5}$$

	C_1	C_1^*	C_2	C_3	C_3^*	C_4	C_5
Standard value	3.4	1.8	4.2	0.8	1.3	1.25	0.4
CFX's value	1.7	0.9	-1.05	0.8	0.65	0.625	0.2

Table A.2-1: Closure Coefficients in pressure strain equation

It needs to be mentioned that the constant values used in CFX differ from those in the original paper [88] or in other literatures which the author has read so far. The reason is still unknown.

ω-based Reynolds Stress Model:

The ω-based Reynolds Stress Model, which is developed by Wilcox [106], is a Reynolds Stress model based on the ω equation. The advantage of ω equation is that it allows for a more accurate near wall treatment with a low-Reynolds number formulation based on the refined mesh near the wall. The modeled equations for the Reynolds stresses can be written as follows:

Reynolds-Stress Tensor:

$$\frac{\partial \bar{\rho}\boldsymbol{\tau_{ij}}}{\partial t} + \frac{\partial}{\partial x_k}\left(\bar{\rho}\tilde{u}_k\boldsymbol{\tau_{ij}}\right) = -\bar{\rho}P_{ij} - \bar{\rho}\Pi_{ij} + \frac{\partial}{\partial x_k}\left[\left(\mu + \sigma^*\bar{\rho}\frac{k}{\omega}\right)\frac{\partial \boldsymbol{\tau_{ij}}}{\partial x_k}\right] + \frac{2}{3}\beta^*\bar{\rho}k\omega\delta_{ij} \tag{A.2-6}$$

Specific Dissipation Rate:

$$\frac{\partial \bar{\rho}\boldsymbol{\omega}}{\partial t} + \frac{\partial}{\partial x_k}(\bar{\rho}\tilde{u}_k\boldsymbol{\omega}) = \frac{\partial}{\partial x_k}\left[\left(\mu + \sigma\bar{\rho}\frac{k}{\boldsymbol{\omega}}\right)\frac{\partial \boldsymbol{\omega}}{\partial x_k}\right] + \alpha\frac{\rho\boldsymbol{\omega}}{k}\tau_{ij}\frac{\partial \overline{u}_k}{\partial x_k} - \beta\bar{\rho}\boldsymbol{\omega}^2 \tag{A.2-7}$$

Pressure Strain Correlation:

$$\Pi_{ij} = \beta^* C_1 \omega \left(\tau_{ij} + \frac{2}{3} k\delta_{ij}\right) - \hat{\alpha}\left(P_{ij} - \frac{2}{3} P\delta_{ij}\right)$$

$$-\hat{\beta}\left(D_{ij} - \tfrac{2}{3} P\delta_{ij}\right) - \hat{\gamma} k \left(S_{ij} - \tfrac{1}{3} S_{kk}\delta_{ij}\right) \quad \text{(A.2-8)}$$

Auxiliary Relations and Closure Coefficients:

$$P_{ij} = \tau_{im}\frac{\partial \overline{u}_j}{\partial x_m} + \tau_{jm}\frac{\partial \overline{u}_i}{\partial x_m}\ , \quad P = \frac{1}{2}P_{kk}, \quad D_{ij} = \tau_{im}\frac{\partial \overline{u}_m}{\partial x_j} + \tau_{jm}\frac{\partial \overline{u}_m}{\partial x_i} \quad \text{(A.2-9)}$$

	C_1	C_2	$\hat{\alpha}$	$\hat{\beta}$	$\hat{\gamma}$
Standard value	1.8	0.52	(8+C_2)/11	(8C_2-2)/11	(60C_2-4)/55

Table A.2-2: Closure Coefficients in pressure strain equation

A.3 Best Practice Guidelines

Turbulence Modeling

RANS methods are the most widely used approach for CFD simulations of industrial flows. It can achieve a good balance between the required accuracy of results and the cost compared with LES and DNS. The two-equation model, especially the SST k-ω turbulence model, has therefore been chosen in the 2D simulations for HPLWR design. The SST k-ω turbulence model gives a good compromise between accuracy and robustness in 2D simulations. Most importantly, it showed the best performance to predict the HTD.

When the work fluid is supercritical water, the SST k-ω turbulence model has a good ability not only to predict the normal heat transfer and enhanced heat transfer, but also to predict the onset of the HTD with a certain deviation. In the cases of simulations in supercritical CO_2, quantitative prediction of the heat transfer deterioration using this model is not satisfactory. This is possibly due to a localized inlet effect.

2D simulations normally aim to validate the model and to investigate the mechanism of HTD, which is not the main purpose in 3D simulations. After the model sensitivity study, it

is clear that the SST model should be used in the simulation for a WWR in a square channel. The computing time consumed by the SST model is nearly half of that consumed by the ωRSM due to the six less equations. Furthermore, the simulations are much easier to converge by using the SST model.

It is also worth to be mentioned that the turbulence model should pair with a proper grid in order to give the best solution. In the case of the simulation of the thermal-hydraulic behaviour to supercritical fluids, the grid compressed strongly towards the heated boundary is recommended in the grid generation in order to fully-resolve the boundary layer. The value of y+ should be less than 1, sometimes need to be close to 0.1.

Guidelines on turbulence models:

- There is no universally valid general turbulence model that is accurate for all cases of simulations. Validation and calibration of the turbulence model with test data are necessary for all applications.

- The selection of physical models is often a personal decision. Depending on our own experience, the SST k-ω turbulence model validated by test data can give a good performance in 2D simulations and 3D simulations involving wire-wrapper that guides the flow. However, in simulations involving 3D rod bundle geometries without wire spacers, the RSM is recommended in consideration of the secondary flows.

- Avoid the use of standard wall functions. In wall-attached boundary layers, the gradients of properties and relative flow variables become large. A large number of grid points close to the heated wall are required to resolve these gradients. Alternatively, a special wall function which is suitable to variable properties under supercritical pressure could be another option.

Conjugate heat transfer should be considered in simulations when the wrapped-wire is introduced into the model. It could remove the local HTD which appears near the contact place between the wire and rod in the absence of cladding material.

Numerical Issues

The spatial discretisation errors, which result from the numerical order of accuracy of the discretisation scheme and from the grid spacing, are primarily concerned with the numerical approximation of convective terms in the governing transport equations. It is well known that a first order scheme is usually not at all suitable for engineering applications involving complex flows with large gradient of properties and thin boundary layers. Therefore the first order methods should be avoided in any CFD simulations of HPLWR.

After a higher order scheme (mostly second) is already given, spatial discretisation errors can be influenced by a given grid. It is also important to provide a high-quality numerical grid in order to reduce the spatial discretisation errors in simulations, which requires the concentrated grid points in the areas of large solution variation (near the surface to fuel rod). Guidelines for grid generation are given in chapter 3.

Guidelines on discretisation scheme:

- Avoid the use of first order scheme. The use of second order scheme (high-resolution in CFX) is recommended.
- Give an estimate of the discretisation error in the simulation by applying a grid-independent study in order to minimise the error caused by grid generation.

There are a variety of opinions on how to judge convergence. In general, the sizes of the RMS (Root Mean Square) residual, Max residual and overall flow balance need to be considered. The level of convergence required depends on the purpose of the simulation. The Max residual are normally 10 times larger than the RMS residual. However, the MAX residual can be 100 times larger than RMS residual when the heat transfer deterioration happens.

In CFX, users can additionally apply a target 'imbalance' for the conservation equations (that is a global balance criterion), which is also helpful to evaluate the running time approximately. The solver will not stop until the residual criteria are met and global balances targets are also met. It is also recommended to set up monitor points for relative quantities e.g. temperature and properties near the heated wall.

Guidelines on convergence target:

- The value of RMS residual level should be lower than 10^{-6} and 10^{-5} in 2D (tube or annulus) and 3D (wire wrapped rod) calculations, respectively. It would not improve the accuracy when the convergence targets are lower than 10^{-6}.
- The value of global imbalances should at least be less than 0.1% before you can consider a solution converged.

Because most of cases are steady-state simulations, the monitored quantities should turn to constant and keep it until the simulations finish.